UNIVERSITEIT VAN PRETORIA
UNIVERSITY OF PRETORIA
YUNIBESITHI YA PRETORIA

CONTROLLED CHLORIDE CRACKING OF AUSTENITIC STAINLESS STEEL

By

Mantsaye S. Raseroka

Study Supervisor:

Prof Chris Pistorius

Submitted in partial fulfillment of the requirement for the degree Master of Science in Applied Science (Metallurgical Engineering)

In the Faculty of Engineering, Built Environment and Information Technology

University of Pretoria

Pretoria

Date of submission: November 2008

Acknowledgements

I would like to thank the following persons and institutions:

Prof Chris Pistorius for the support, knowledge, valuable guidance, encouragement when times were tough and as well as advice.

The staff and students of the Metallurgical Engineering Department for your assistance; I appreciate the support, especially by Mrs. Sarah Havenga.

Dr Sabina Verryn, for help with XRD analysis.

Eskom, for their financial support, allowing me to pursue these studies, and for the facilities and resources.

Mark Newby and his team for support, help and training.

Rob Hederson for help with the control box.

Ronny Scheeper for finite element analysis model.

My friends and collogues for your understanding, support and time which you gave when I needed it. Jimmy Khosa for encouragement and help that you always give.

My family, especially my mother, for love, care and understanding.

I thank you all and I greatly appreciate whatever help or support you offered during this study period. Most importantly I thank God for making these studies possible.

UNIVERSITEIT VAN PRETORIA
UNIVERSITY OF PRETORIA
YUNIBESITHI YA PRETORIA

CONTROLLED CHLORIDE CRACKING OF AUSTENITIC STAINLESS STEEL

By: MS Raseroka
Supervisor:
Professor PC Pistorius
Department of Materials Science and Metallurgical Engineering
Master of Science in Applied Science

ABSTRACT

Type 304 stainless steel is used in various applications where corrosion resistance is required. This material is selected for weldability and corrosion resistance, but it can suffer stress corrosion cracking (scc), corrosion fatigue, pitting and crevice corrosion in chloride environments. The aim of this project was to produce Type 304 containers with intentional stress corrosion cracks, to serve as test samples for future weld repair trials.

A test rig was constructed which used thermal stress to crack Type 304 tube samples; a central Type 310 stainless steel bar contained a heating element, so that the bar serve as a heat source and a stressing element. The rig was filled or half filled with magnesium chloride solution. The elastic strain in the tube sample was directly related to the temperature difference between the central bar and the sample. The thermal stress was sufficient to cause stress corrosion cracking. The tests were terminated when the first crack extended through the wall thickness of the 304 tube sample. The distribution and depth of cracks were determined after the tests. The test procedure caused the formation of multiple cracks in the tube sample.

The temperature controller caused cyclical variation in the bar temperature and hence in the thermal stress. However, the temperature variation did not have an effect on cracking; corrosion fatigue did not contribute to cracking, and the cracks had the classic branched transgranular morphology of chloride cracking.

Keywords

Strain, temperature, chloride stress corrosion cracking (scc), corrosion fatigue, austenitic stainless steel, Type 304L stainless steel, crack density

Table of Contents

List of tables

List of figures

Chapter One

1. Background and SCC issues or challenges

1.1Introduction

Type 304/304L stainless steel is widely used, for example in the nuclear power and brewery industries and at swimming pools as roof fasteners and rods. These stainless steels can suffer from chloride induced stress corrosion cracking (SCC), corrosion fatigue, as well as pitting and crevice corrosion in the presence of chloride. Chloride stress corrosion cracking does occur on austenitic stainless steel components and poses a danger which can result in catastrophic failure. Other types of corrosion act as initiation points and stress raisers for chloride stress corrosion cracking [1].

The aim of this project was to provide cracked samples of defined geometry for a larger stress corrosion cracking repair project, aimed at the *in-situ* repair of the cracked components.

1.2 SCC

Stress corrosion cracking is the environmentally assisted cracking of ductile material in an apparently brittle manner under tensile stress. Type 304L stainless steel in an aqueous chloride solution, under tensile stress, (residual stress and/or operational stress), can undergo stress corrosion cracking. The crack morphology could be transgranular, intergranular, and branched [2, 3]. Crack direction is mainly perpendicular to the load or stress.

1.3 Operational experience/Historical Background and Current state

During plant maintenance inspections are performed to identify defects or damage, and to verify the integrity of components. Stress corrosion cracking is one of the forms of damage which is detected by inspection of or leakage from components. Depending on the extent of defects, replacement or repair can explored. Tungsten inert gas arc welding and recently also laser and friction welding have been researched as repair methods [1, 4]. In one example, overlay

weld repair was performed on a brew kettle; however due to shallow weld repair, the crack was not fully sealed (a notch was still present) and further crack propagation caused the weld repair to leak [1].

1.4 Problem statement and Research questions

Stress corrosion cracking can be costly where plant damage occurs and much more so when lives are lost. An example of the latter was the collapse of indoor swimming pool roofs. The roof had been supported by stainless steel (SS) rods in tension [5,6,7,8]. In the brew kettle example, initial cracking and subsequent leaking of the weld repair affected down time of the plant [1]. When the cost of replacement is high, possible repair is investigated, but samples or test rigs are required for testing of the repair procedure. As background to this project, a need for researching possible repair processes was identified; this project focused on the production of cracked samples that represent the in-service condition. The final practical aim (which is outside the scope of this project) is to perform repair *in-situ*, while liquid is leaking from the cracked vessels.

Research questions

- Can chloride stress corrosion cracking be produced in a controlled manner under controlled conditions, to provide samples to test the repair procedure?
- How does residual stress from manufacturing and fabrication influence cracking?
- What is the influence of both static and cyclic thermal stresses on stress corrosion cracking?

1.5 Rationale for study and Research objective

This research forms part of the repair project and is to supply the non-standard samples to be used in the simulated repair process, so contributing to the development of in-service weld repair of stress corrosion cracks. Repair is seen as a way to avoid replacement costs and also to help in managing the shortage of special alloys.

Chapter Two

2 Brief Literature review on Stress Corrosion Cracking

2.1. Introduction/SCC Overview

Austenitic stainless steels can undergo chloride stress corrosion cracking in chloride solutions under tensile stress. The combination of tensile stress and an aggressive environment can cause cracking even though the stresses are below the yield strength. Chloride induced stress corrosion cracks are branched, with the macroscopic path normal to the applied tensile stress. Anodic dissolution does plays a significant role in crack growth [2, 9]. Stress corrosion cracking generally occurs at temperatures between 50ºC to 350ºC [10]. Solution treated, unsensitised austenitic stainless steel has mainly transgranular crack paths, while cracks in sensitised austenitic stainless steel are intergranular. The fracture surface of stress corrosion in region I and II are transgranular, intergranular or both while region III fracture surface is of made microvoids coalescence. At low K_I close Kiscc the crack morphology is transgranular. SCC anodic dissolution and crack growth require activation energy [11].

Factors that influence Stress Corrosion Cracking

- Constant or fluctuating temperature (which can affect the stress in the material)
- Oxygen levels in the solution
- Single phase or dual phase (steam-vapour, water-liquid or both) environment (dry and wet)
- Concentration of minor and major solution species. For example, a $MgCl_2$ solution is more aggressive than NaCl and $CaCl_2$ solutions [2]
- Acidity (*p*H) of the solution
- Electrochemical conditions, such as galvanic coupling or applied cathodic protection
- Composition and microstructure of the material; this was not studied here since the aim was to produce samples which simulate the actual components (which are of Type 304 stainless steel).

The conditions required for stress corrosion cracking to occur are a susceptible alloy in a specific environment in the presence of tensile stress; see Figure 2.1.

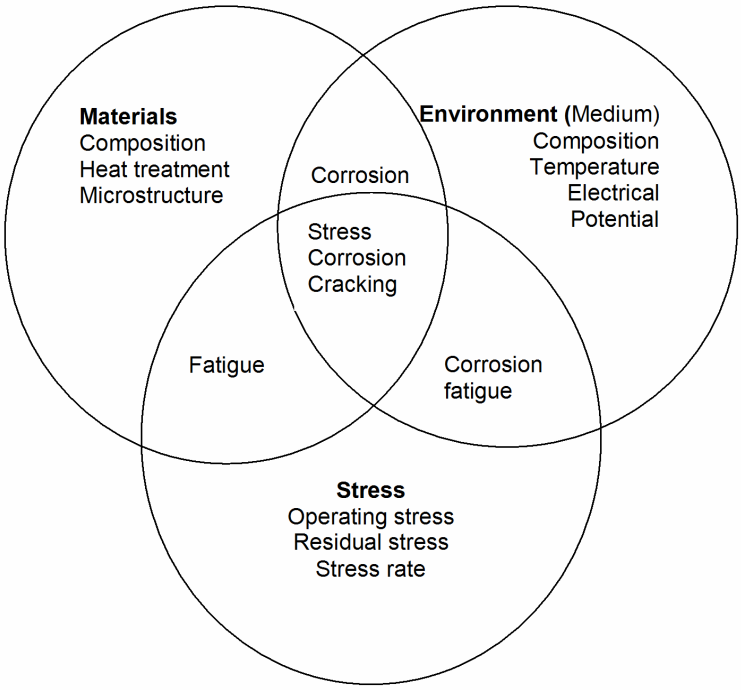

Figure 2.1 Three conditions are to be present for SCC to occur, namely environment, tensile stress and a material which is susceptible [9].

Environments that promote stress corrosion cracking of austenitic stainless steel are the following [9]:

- Chlorides, both inorganic and organic
- Caustic solutions
- Sulphurous and polythionic acids

2.1.1 Mechanism of chloride Stress corrosion cracking

Several mechanisms for stress corrosion cracking have been proposed; a useful review of these is given by Jones and Ricker [12]. In the case of chloride cracking of stainless steels, the mechanism must account for the cleavage-like nature of the failure; this has been taken to imply a role of mechanical failure in crack growth [13]. However, the nature of this mechanical role is not clear. In the mechanism of film-induced cleavage [14], corrosion produces a surface product layer which can inject cracks into the underlying metal. Such a surface film was found by transmission electron microscopy of chloride cracks in austenitic stainless steel [15]. In applying this idea, Nishimura [16] proposed that crack growth occurs when the stress at the crack tip reaches a critical value, which is independent of the corrosive environment; the proposed role of the

environment is to change the rate at which the local stress at the crack tip increases as a result of corrosion – but there appears not to be direct experimental evidence for the constancy of the fracture stress, and the effect of environment on the rate of stress increase. In contrast with the proposal that the stress corrosion crack grows by brittle failure, it has also been suggested that plasticity is enhanced at the crack tip [17].

The lack of a generally accepted mechanism for chloride cracking of austenitic stainless steels is a difficulty in the present work, because there is no single theoretical framework which can be used to explain the experimental observations.

2.1.2 The transgranular crack advancement in cleavage manner

As is already established that transgranular SCC occur by intermittent microcleavage event due to a thin film. The increments are about 0.5µm long Sieradzki, et. Al. and Pugh are in agreement [10, 18]. The mean cracking velocity is estimated to be 0.1µm.s^{-1} and it was consistence with spacing of crack front striations.

Transgranular SCC appears to propagating by discontinuous cleavage. Blunted crack is continues by cleavage crack the blunted due to lagging of step formation velocity behind the cleavage crack tip, which continues after crack arrest forming a ligament thus blunt crack tip. When stress transferred back to tip the environment reinitiate the cleavage crack after blunting [18].

The Cottrell – Lomer lock allows dislocations to pile up on each of the {111} planes and eventually crack will be formed on (110) plane [10]. The film is reformed because of environment, a brittle crack can initiate under thin film (oxide, de-alloyed layer and hydride) advance for short distance in cleavage manner in substrate where after step formation is completed then the environment reinitiate the cleavage crack [18].. Dislocations are allowed to pile up on lock until cracking again. When two slipping planes are equally stress, the stress required to nucleate a crack in the film may by roughly estimated that is

the crack driving force [10]. The film formation determines the time between crack growth events. The film mismatch and thickness influence discontinuous cleavage crack growth.

Early proposed cause of cleavage cracking was Hydrogen Embrittlement, Adsorption and Selective dissolution but from selective dissolution film–induced cleavage was deduce and it seemed more suitable [18].

2.2 The conditions required for SCC to occur; other factors that affect SCC

The main factors are summarised in Table 2.1

Table 2. 1 Material, environmental and mechanical factors that influence stress corrosion cracking [19].

Material Factors	Environmental Factors	Mechanical Factors
Composition Microstructure Contaminants or impurities Grain size Grain orientation	Temperature pH Electrochemical Potential Solute species Solute concentration Oxygen concentration	Stress Strain rate

2.2.1 Environmental effects

Short discussions on the major environmental effects are presented below.

Dissolved Oxygen

The time to failure in an oxygenated environment is shorter, as shown in Figure 2.2 which compares cracking in oxygenated and nitrogen purged chloride solutions. The greater severity of cracking in the oxygenated solution supports the role of anodic dissolution in crack growth.

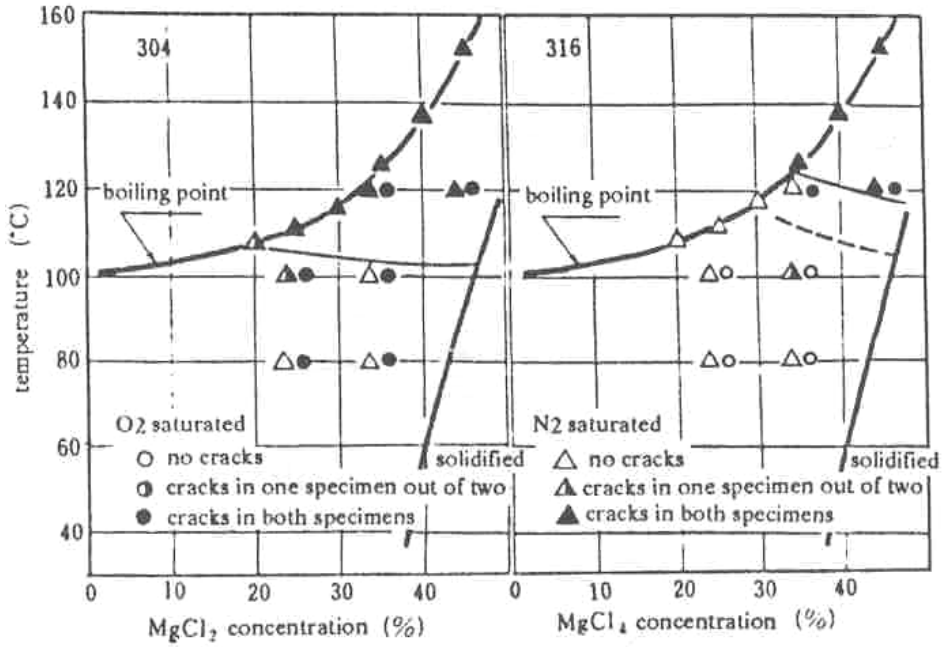

Figure 2.2 Susceptibility to SCC of Types 304 and 316 stainless steel in oxygen-saturated and nitrogen-saturated $MgCl_2$ solution (U-bend test) [2]

Acidity (pH)

If the *p*H is below 2, uniform corrosion can predominate, but recent work shows that chloride stress corrosion cracking does occur at low pH at room temperature [20]. In general, the time to failure is longer at higher *p*H. [2, 19]

Temperature effect

At higher temperature, the time to failure is shorter. The crack initiation time and crack propagation time are not that easy to distinguish experimentally. The total time to failure is mostly reported. Kowaka [2] showed the apparent activation energy to be between 54 and 96 kJ/mol (figure 2.3).

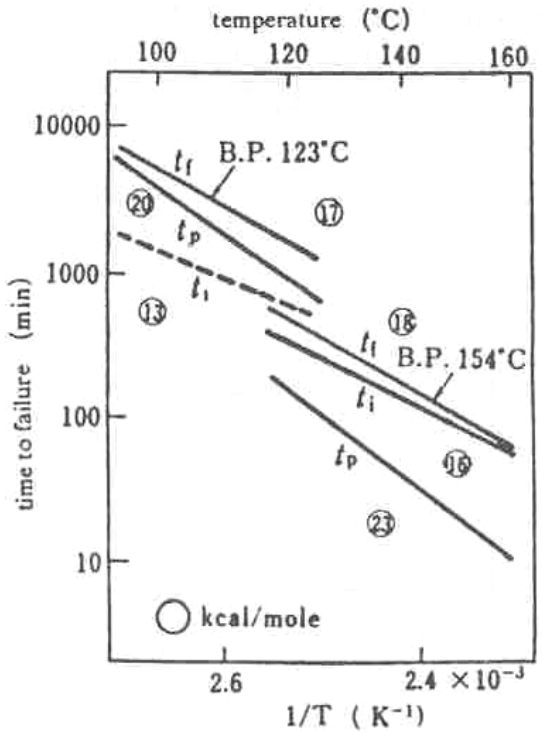

Figure 2.3 Effect of temperature on stress corrosion cracking of Type 304 stainless steel in $MgCl_2$ [2]

Chloride Solutions

$MgCl_2$ solution is more aggressive than sodium chloride (NaCl) solution with regards to stress corrosion cracking [2]. All other chloride salts are less severe compared with $MgCl_2$ and NaCl [2]. However, the chloride activity is more significant than cation influence. Chloride concentration affects the time to failure: high concentration reduces time to failure while low concentration prolongs time to failure.

Effect of Potential

Stainless steel behaves differently at different potentials, depending on the presence and stability of the passive layer, as illustrated by figure 2.4. In this figure, regions I, II and III are where the passive film is unstable, and where active-passive corrosion-resistant alloys can be expected to be susceptible to stress corrosion cracking. The passive film is assumed to be a prerequisite for stress corrosion cracking [9]. Stress corrosion cracking occurs in narrow potential ranges, with pitting corrosion predominating at more positive potentials.

Corrosion pits can serve as initiation points of stress corrosion cracks because of the stress concentrations at pits.

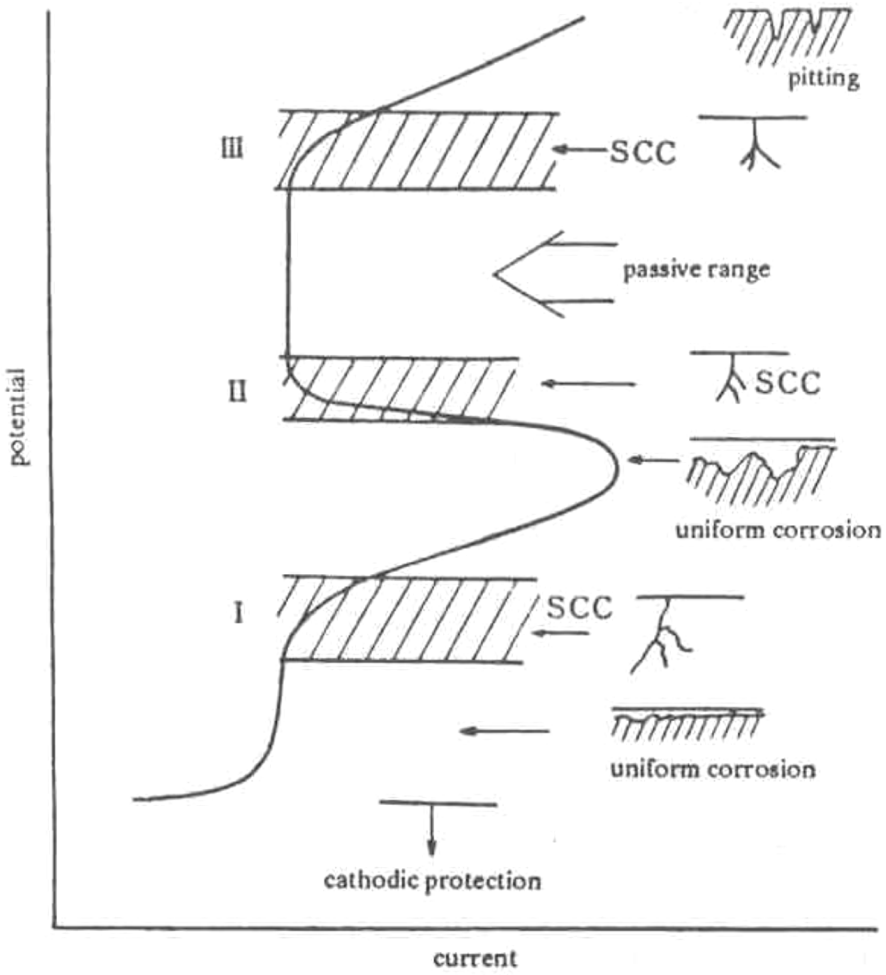

Figure 2.4 Schematic anodic polarisation curve showing zones of susceptibility to stress corrosion cracking [9]

2.2.2 Stress

The presence of tensile stress is essential for stress corrosion cracking. In most instances, metals are subjected to tensile stress in service, often in the presence of residual stresses caused by welding or/and forming. The residual stresses can be comparable with the proof stress and can cause cracking [2]. The magnitude of the stress affects time to failure (Figure 2.5).

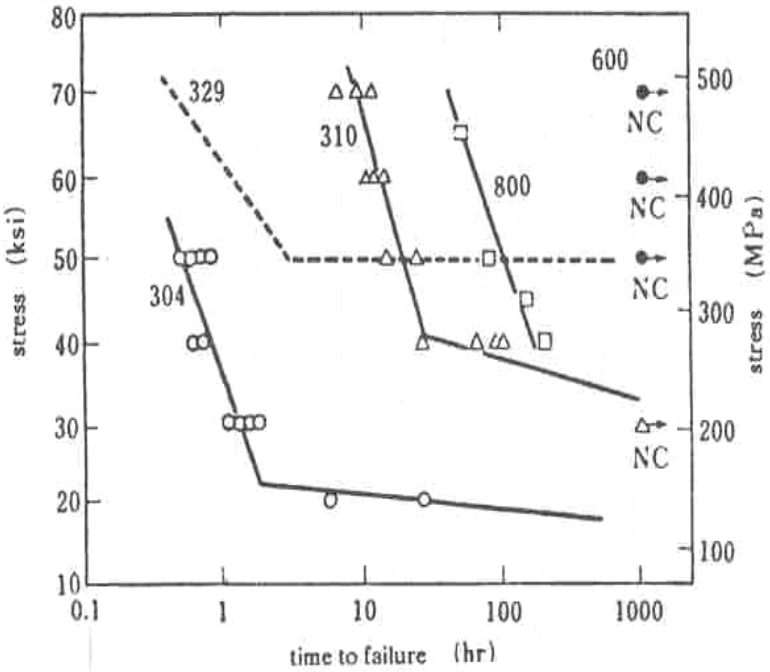

Figure 2.5 Effect of stress on SCC of several materials in boiling 45% $MgCl_2$ at 154°C (see figure 6.16 pp 361 of reference [2]).

2.2.3 Effect of Metallurgical factors [2]

Factors such as alloying elements, grain size, cold work, and surface condition of the material influence stress corrosion cracking. Alloying elements effects can be detrimental, variable or beneficial for stainless steel. For example Ni, C and Si have positive effects in reducing susceptibility to stress corrosion cracking while Cr, P and N increase susceptibility to stress corrosion cracking. The table below summarises the effects of alloying elements on the susceptibility of stainless steel to stress corrosion cracking. The temperature influences the effect of each alloying element on susceptibility to stress corrosion cracking. Some alloying elements are beneficial, some are detrimental, and others do not have any effect. Susceptibility of stainless steel is shown in by figures 2.6 and 2.7 as a function of nickel content. At low nickel levels (ferritic stainless steel) and high nickel levels (nickel alloys) resistance to stress corrosion is improved. Certain levels of silicon can increase the resistance of stainless steel to stress corrosion cracking (see figure 2.8). The combination of phosphorus and nitrogen should be well controlled not to compromise the stress corrosion properties of austenitic stainless steel (figure 2.9). Molybdenum addition increases the threshold stress

intensity of stainless steel, improving the stress corrosion cracking resistance of Fe-Ni-Cr alloys [21].

Table 2.2 The effect of alloying elements on cracking of stainless steel in various environments [2,21]

Element	Boiling 45% $MgCl_2$	Boiling 35% $MgCl_2$
C	O	O•
Si	O	O
Cr	X	□
Mo	X	O
Cu	X	O
P	X	X
N	X	X
Ni	O	

Remark O: beneficial X: detrimental □: no appreciable effect
•: effective in inhibiting transgranular cracking

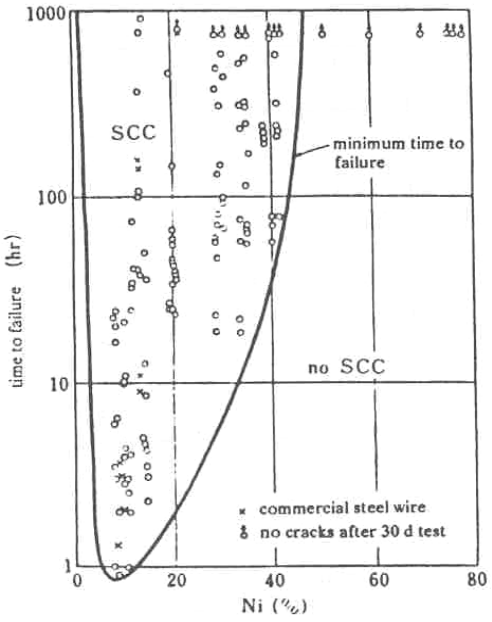

Figure 2.6 Effects of Ni content on SCC of stainless steel in boiling 42% MgCl2 [2]

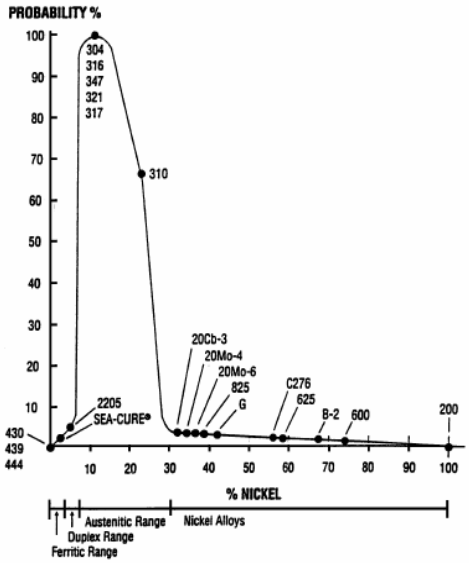

Figure 2.7 Probability of stress corrosion cracking as function of the alloy's nickel content [1]

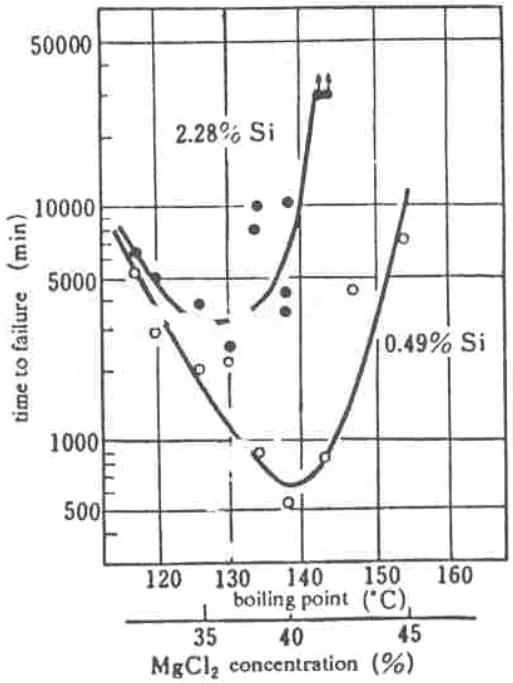

Figure 2.8 Effects of Si on SCC of 17Cr-13Ni stainless steel in various boiling $MgCl_2$ solutions at a constant load of 245MPa [2]

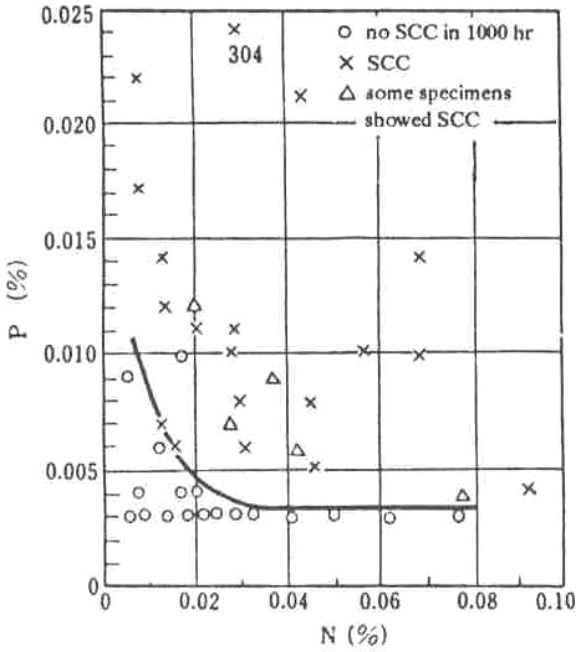

Figure 2.9 Effects of P and N on SCC of 17Cr-13Ni stainless steel in various boiling $MgCl_2$ solutions at a constant load of 245MPa [2]

Grain size has a minor effect on transgranular stress corrosion cracking. Larger grain size plays a role in intergranular stress corrosion cracking (of sensitised steels) in the formation of a galvanic cell, where the grain boundary is the anode while the rest of the grain is the cathode.

Surface finish affects susceptibility to stress corrosion cracking. Surface defects or notches can act as pre-existing defects to initiate cracks.

2.2.4 Corrosion fatigue and Stress Corrosion Cracking

The importance of possible cyclical stressing effects in this project is that the temperature control method which was applied inherently caused the stress to be non-static. Mechanical fatigue occurs in non-corrosive environments under cyclic stress; in corrosive environments the fatigue strength is generally reduced [21], and the corrosion-assisted fatigue life is lower than fatigue life in air (see figure 2.10). The factors which influence corrosion fatigue and stress corrosion cracking are tabulated in table 2.4 and some of the factors are discussed in this section.

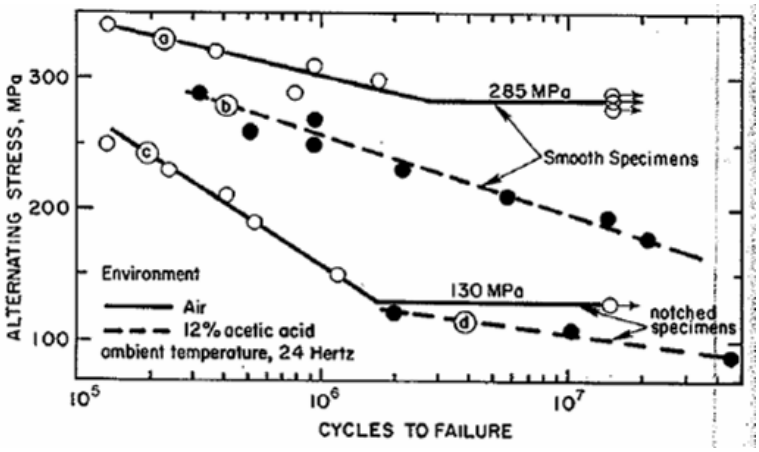

(i)

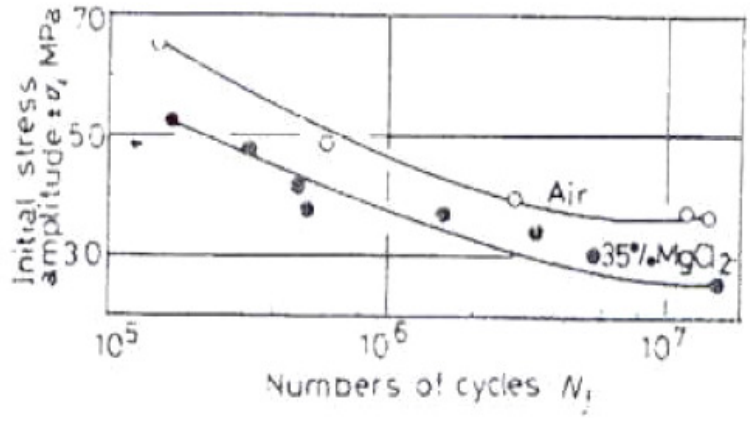

(ii)

Figure 2.10 Effect of corrosion to lower the fatigue limit of (i) 316 in air and acetic acid and (ii) 321 in air and $MgCl_2$ solution [21,22]

Table 2.3. Factors Affecting Corrosion Fatigue [23, 19]

Metallurgical	Environmental	Mechanical	Geometrical
• Alloy composition • Microstructure and crystal structure • Heat treatment • Grain boundary structure • Grain shape and size • Surface texture • Distribution of alloy elements and impurities • Deformation mode (slip character, twinning, cleavage) • Mechanical properties (strength, toughness, etc.)	• Type of environments (gaseous or liquid) • Partial pressure of damaging species in aqueous or other liquid environments • Concentration of damaging species in aqueous or other liquid environments • Temperature • pH • Electrochemical potential • Viscosity of the environment	• Fatigue load frequency • Fatigue load ratio • Fatigue load waveform • Maximum stress-intensity factor and stress-intensity factor range • Load interactions in variable amplitude loading (over/ under/spectrum load) • Residual stress	• Crack size • Crack geometry • Specimen thickness (plane strain versus plane stress)

2.2.4.1 Comparing Stress corrosion cracking with Corrosion fatigue [24]

Stress corrosion occurs in specific environments for a specific material while corrosion fatigue happens in any corrosive environment. Tensile loading is required for both situations, but the stress ratio (the ratio between the minimum and maximum stresses) distinguishes the two mechanisms. Temperature increases crack growth rates of both stress corrosion and corrosion fatigue cracking. In stress corrosion cracking both failure modes are present (intergranular and transgranular) and in corrosion fatigue generally only transgranular. The corrosion fatigue crack generally contains corrosion product but stress corrosion cracks generally do not show any corrosion product. The corrosion fatigue fracture surface can show beach marks and striations, and the

fracture surface of stress corrosion is cleavage-like. Cathodic protection suppresses both cracking mechanisms (see table 2.5).

The morphology of cracking of chloride SCC (of non-sensitised material) and corrosion fatigue are both transgranular, but stress corrosion cracks are more branched [24]; see Figures 2.11, 2.12, 2.13, 2.14 and 2.15 for examples.

Corrosion fatigue is similar to stress corrosion cracking in that the presence of a corrosive solution induces apparently brittle fracture in alloys that are normally ductile. The crack propagates perpendicularly to the principal tensile load for both. However, corrosion fatigue requires neither a specific corrodent nor a very low corrosion rate, and acts on pure metals and alloys. Corrosion fatigue propagates at a low rate so corrosion product is likely to be present in the crack [9].

Strong mixing occurs between the crack tip solution and solution from other parts of the corrosion fatigue cracks [25] due cyclic loading (and the resulting pumping action), in contrast with the static situation for stress corrosion cracking.

Table 2.4. Characteristics of Environmentally-Assisted Cracking [26, 9, 2]

	Stress Corrosion Cracking	**Corrosion Fatigue**
Stress	Static tensile	Cyclic and tensile
Aqueous corrosive agent	Specific to the alloy	Any
Temperature	Increases	Increases
Pure metal	Resistant	Susceptible
Crack morphology	Transgranular, Intergranular, Branched	Transgranular, Unbranched, Blunt tip
Corrosion products in cracks	Absent	Present
Crack surface appearance	Cleavage-like	Beach marks and/or striations
Cathodic protection	Suppresses	Suppresses

2.2.4.2 Effect of Stress

Placing a specific material such as type 304L stainless steel under cyclic or alternating stress in a corrosive environment, particularly chloride or sulphide solutions, can result in corrosion fatigue (while stress corrosion cracking occurs under static stress in same corrosive environment) [21,24,27].

Cyclic loading under cracking conditions need not accelerate crack growth: movement of the flanks of the crack can serve to expel (pump) the solution within the crack, and decrease concentration differences between the crack interior and bulk solution. [24, 25]

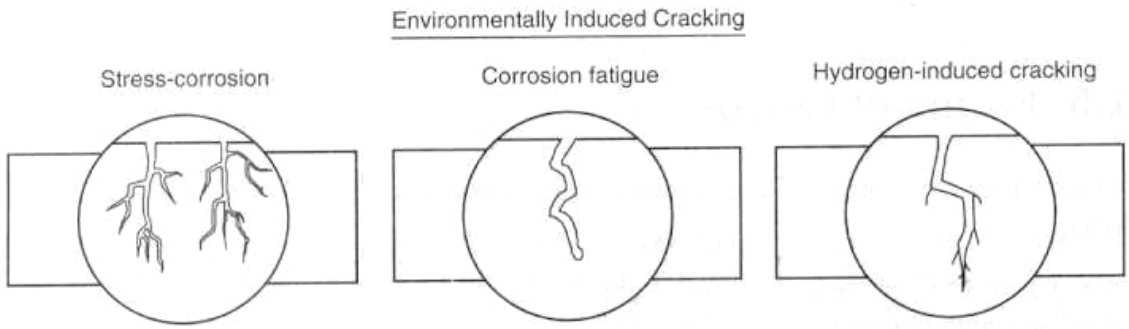

Figure 2.11 Cracking morphology of SCC and CF [9]

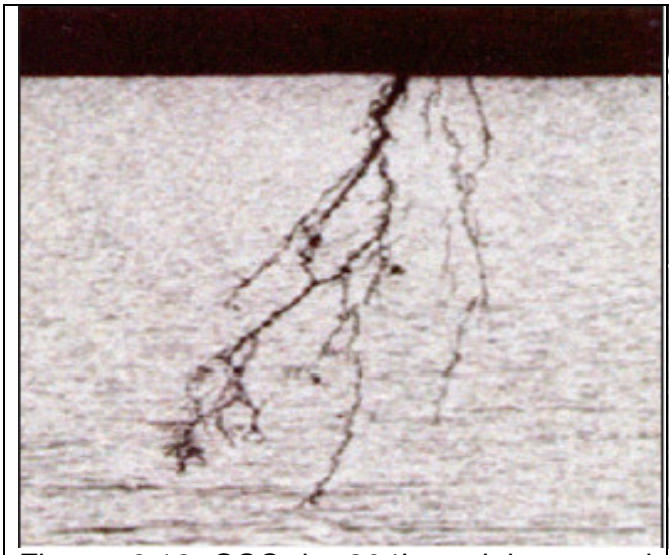

Figure 2.12 SCC in 304L stainless steel pipeline [27]

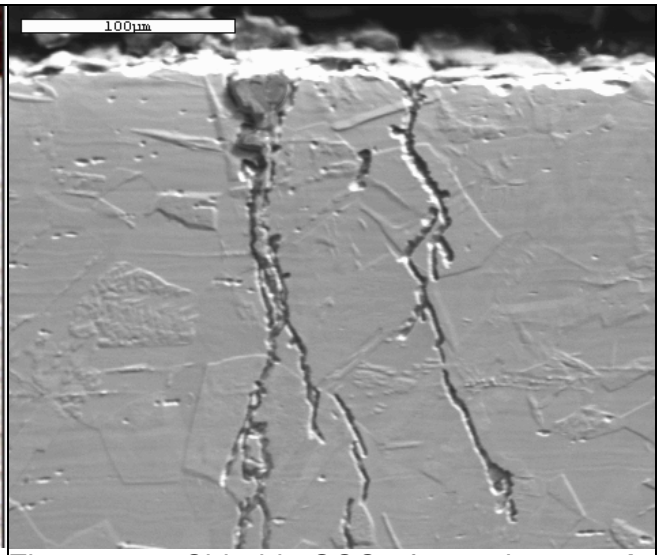

Figure 2.13 Chloride SCC of sample test 3A top (this work)

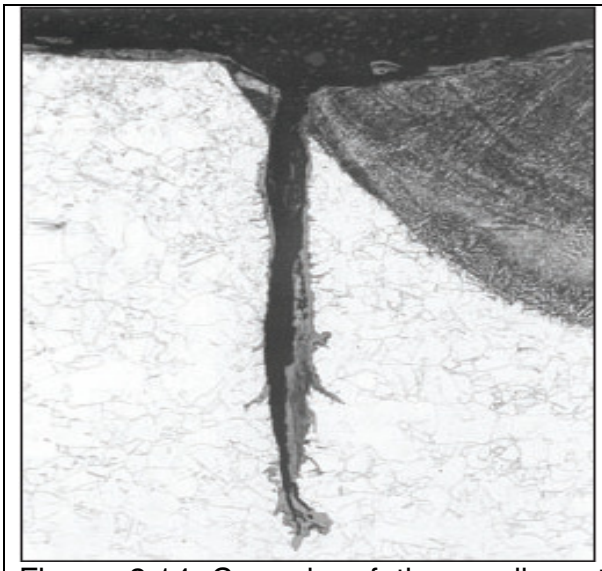

Figure 2.14 Corrosion fatigue adjacent to weld in 316 stainless steel pipeline [27]

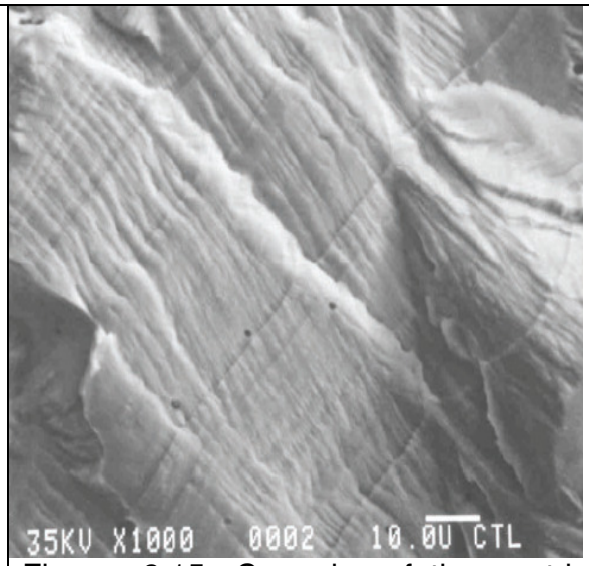

Figure 2.15 Corrosion fatigue striation (scanning electron micrograph) [27]

2.3 Preventing and controlling Stress corrosion cracking

SCC can be managed or controlled by repairing the material, changing the environment or reducing tensile stress, or can be prevented by changing the material (using resistant material).

2.3.1 Changing Environmental conditions

Possible environmental changes included the following:

- Raising the pH of the solution will reduce the probability of stress corrosion cracking.
- Designing to minimise crevices and localised deposits
- Reducing the chloride concentration.
- Cathodic protection (making the potential less positive than the presumed stress corrosion cracking threshold)

2.3.2 Reducing Stress

Several methods had been practised to reduce the stress. These include proper welding methods, reduction of the residual stresses by stress relieving the formed or welded material, and shot peening the component (resulting in compressive stresses on the surface).

2.3.3 Material choice

High-nickel alloys and duplex stainless steels (such as 2205) can be used, but are more expensive. For some applications, ferritic stainless could be used and offers lower cost. In low chloride environments type 316 stainless steel would more suitable because it has better pitting corrosion resistance than 304 stainless steel.

2.3.4 Repairing defects

Weld repair of defects is recommended if changing the environmental conditions is difficult, residual stress are lower due to geometry, manufacturing and construction and replacement of the material is not possible [1]. Methods such as laser and tungsten inert gas welding have been trialled on pipes and tanks [1, 4]. However, welding may itself introduce new defects. A summary of welding defects and corrosion phenomena resulting from these defects is shown in figure 2.16. Such defects can compromise the integrity and the quality of weld repairs.

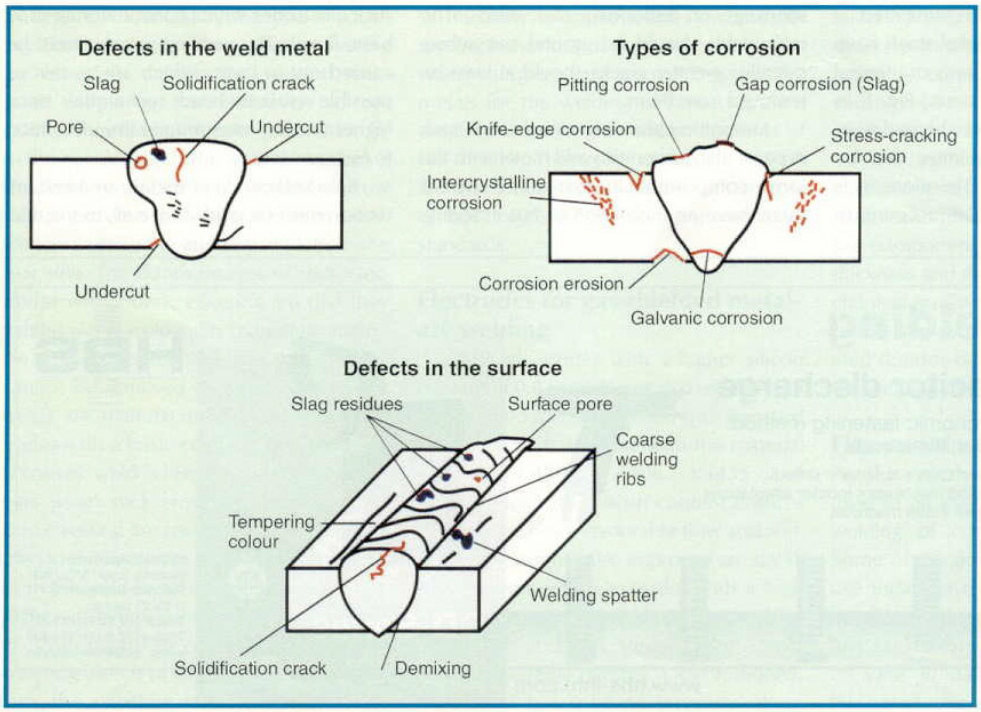

Figure 2.16 welding defects and corrosion phenomena resulting from these defects [28].

2.3.5 Laser welding

As mentioned, this research is part of larger project which aims to repair the stress corrosion cracks in-service. For this reason, the repair process is mentioned briefly.

Laser welding is well established in the fields of repair and surface protection [29]. Laser welding is a fusion welding process where any weldable material is joined using a laser beam as a high energy-density power source. Laser cladding involves the deposition of the material from powder or rod filler onto a substrate using laser heating. The process can be used as a repair procedure to rebuild wall thickness. Wear prevention by hard-surfacing the components and improved corrosion resistance can be obtained [30, 31].

With laser welding or cladding it is possible to control the depth of penetration to a greater extent, compared with Tungsten Inert Gas and Metal Inert Gas welding processes. Welding at high speed and at low heat input rates are possible, depending on the power of the equipment used. Advantages of laser welding are listed in Table 2.3. A typical nozzle typical arrangement is shown in figures 2.17. and 2.18 As schematic picture of the nozzle during the cladding process is shown by figure 2.18.

Table 2.5 Comparison of laser welding with conventional welding processes [32]

	Laser	**Electron Beam**	**Resistance Spot**	**Gas Tungsten Arc**	**Friction**	**Capacitive Discharge**
Weld Quality	Excellent	Excellent	Fair	Good	Good	Excellent
Weld Speed	High	High	Moderate	Moderate	Moderate	Very High
Heat Input Into Welded Part	Low	Low	Moderate	Very High	Moderate	Low
Weld Joint Fit-Up Requirements	High	High	Low	Low	Moderate	High
Weld Penetration	High	High	Low	Moderate	High	Low
Range of Dissimilar Materials	Wide	Wide	Narrow	Narrow	Wide	Wide
Range of Part Geometries/Sizes	Wide	Moderate	Wide	Wide	Narrow	Narrow

	Laser	Electron Beam	Resistance Spot	Gas Tungsten Arc	Friction	Capacitive Discharge
Controllability	Very Good	Good	Fair	Fair	Moderate	Moderate
Ease of Automation	Excellent	Moderate	Excellent	Fair	Good	Good
Initial Costs	High	High	Low	Low	Moderate	High
Operating / Maintenance Costs	Moderate	High	Moderate	Low	Low	Moderate
Tooling Costs	High	Very High	Moderate	Moderate	Low	Very High

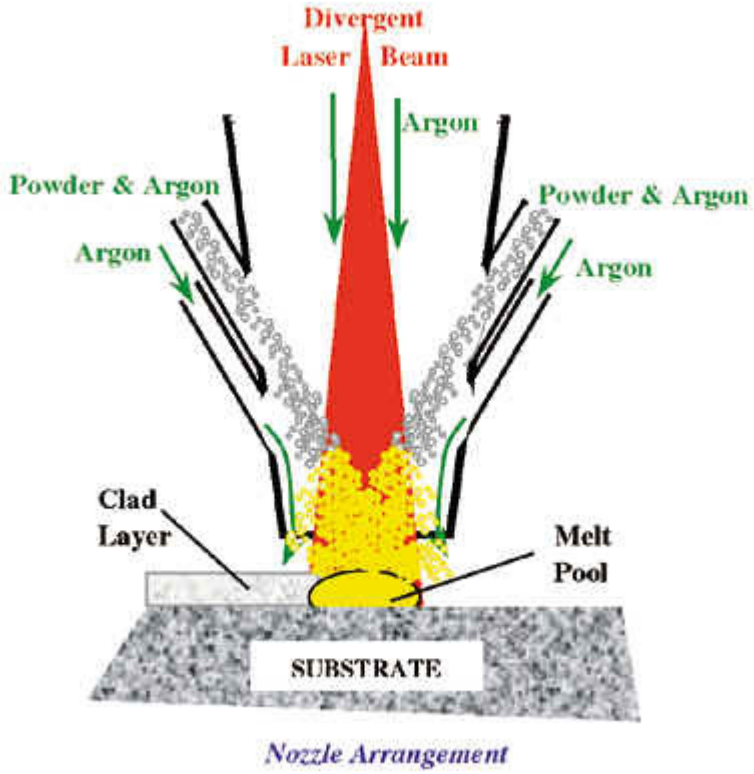

Figure 2.17 Nozzle arrangement for laser cladding [33]

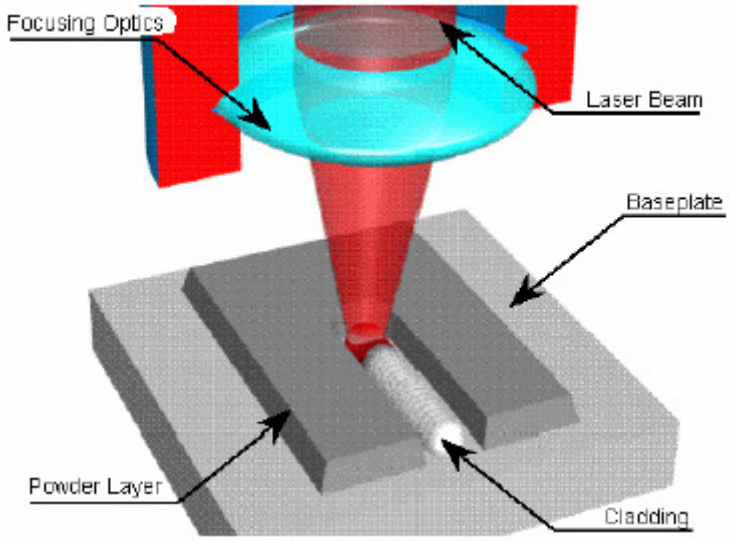

Figure 2.18 Single cladding process [34]

Chapter Three

3.1 Hypothesis

This work tested the hypothesis that (1) small amplitude loads when superimposed on sustained or constant load result in stress corrosion cracking at lower loads and (2) that thermally induced stress, together with residual stress from manufacturing and fabrication will reach the threshold stress required to crack the sample in a small laboratory rig.

3.2 Scope of research

The experimental work investigated stress corrosion cracking of non-standard samples, with cyclical loading superimposed on a baseline stress. The effects of cyclical strain, thermal stress and temperature on the time to failure were assessed, and the fracture surface and crack morphology were examined.

Chapter Four

4 Experimental design and methodology

4.1 Introduction

The designed rig (see figure 4.1) was constructed from tubes of type 304L stainless steel (samples to be cracked) and type 310 stainless steel plates and hollow bar (stressing elements). A heating element was inserted in the hole in the central type 310 bar. The resulting temperature difference between the bar and tube caused thermal stress (tensile in the 304L tube, and compressive in the type 310 bar). The inner surface of the 304L tube was exposed to magnesium chloride solution and the outside exposed to atmosphere. In the presence of tensile stress and magnesium chloride solution, at temperatures above 60℃, Type 304L stainless steel is expected to crack. Type 310 stainless steel has superior stress corrosion cracking resistance. Filler metal ER309L Si is suitable for dissimilar welding and was used here to fabricate the rig.

Chemical analysis and mechanical testing of Type 304L stainless steel were performed. Strain gauges mounted on the tube were used to measure the strain and thermocouples were used to measure temperature (both types of measurement were recorded with a data logger). Following testing, crack depths and crack density were measured, and cross-sectional samples were examined metallographically. Fracture surface analysis was performed on some selected fracture surfaces. The success of the study to produce cracked samples will be followed by a Laser cladding or welding repaired.

4.2 Sample design (rig design) and testing conditions

Rig Design

The test rig was designed to simulate a vessel, pipe or tank that has undergone stress corrosion cracking and needs repair. The temperature difference between the hollow bar and 304L stainless steel tube induced thermal stress in the 304L

tube, superimposed on residual stresses from manufacturing and fabrication. The cracks were expected to initiate from the inside of the 304L tube.

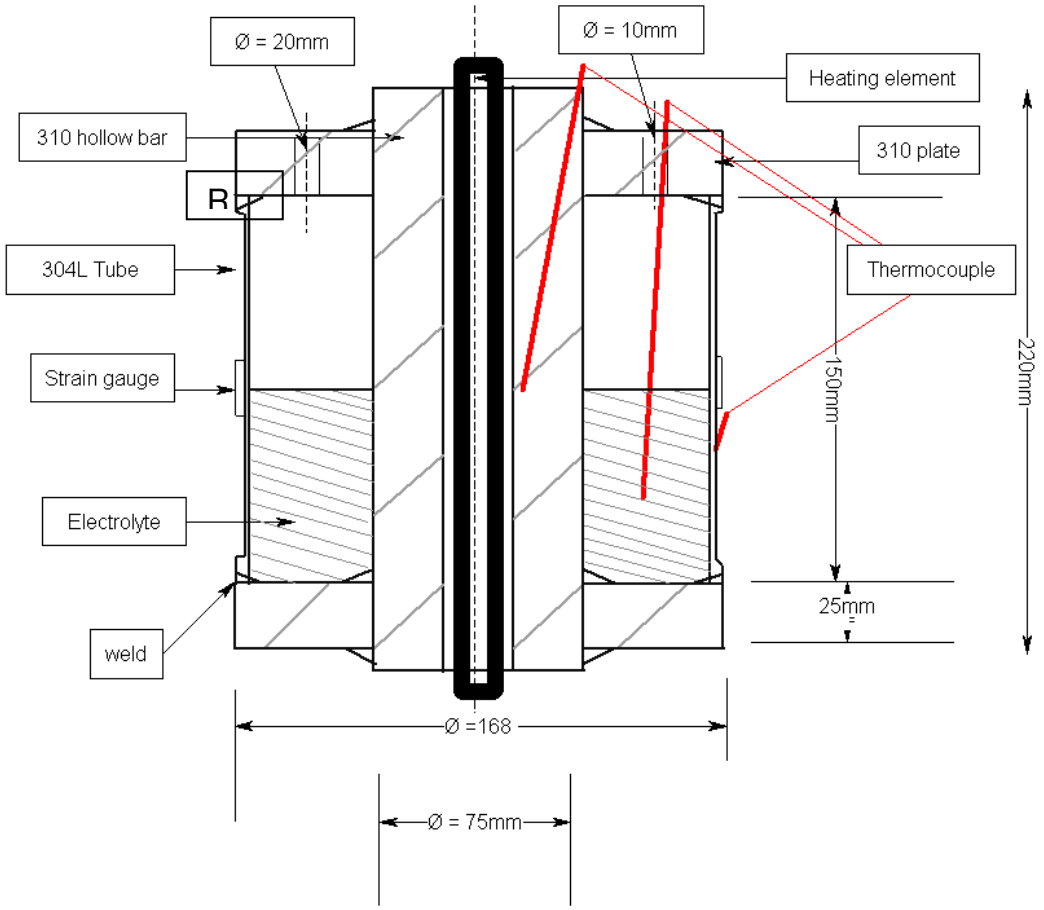

Figure 4.1 Schematic illustration of test rig. "R" shows the top weld.

A successful outcome with the designed rig was defined as failure of only the 304L tube, with the hollow bar carrying the (compressive) load without failing. The dimension and sizes selected have to be according to load carry capacity. To test whether the dimensions selected are suitable, design calculations (see appendix A) for load carrying capabilities/limits were performed, to show that the center bar and outer tube will be able to carry the load according to experimental requirements and that the sizes are suitable in terms of diameters and wall thickness.

Electrical circuit: Heating element

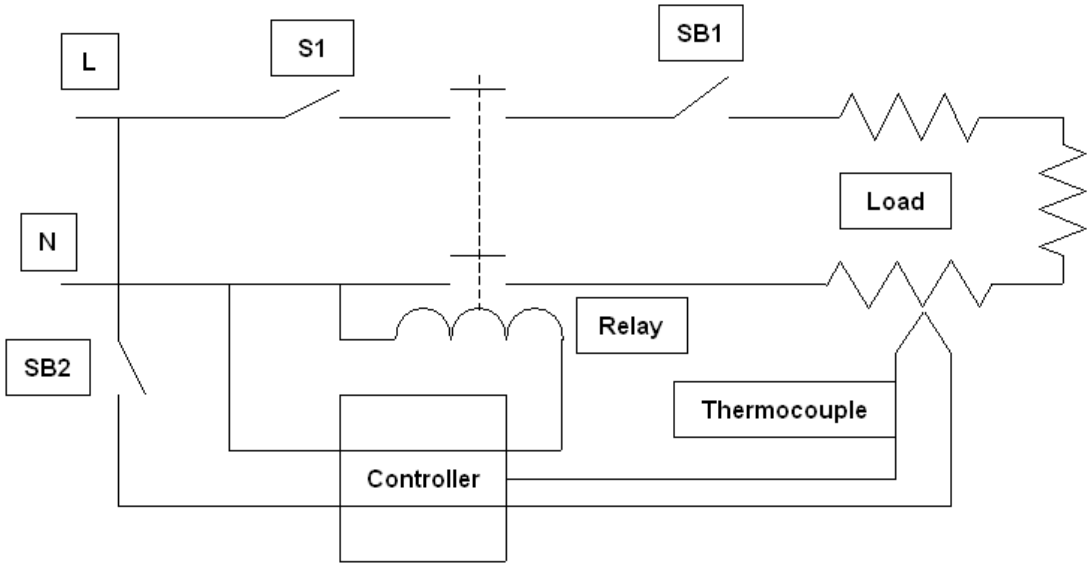

Figure 4.2 Schematic electric circuit of the heating element with single temperature controller

The electrical circuit with heating element and controller is shown in figure 4.2. One of two controllers could be selected, where one had a large (0 to 800ºC) temperature range and the other had a smaller (0 to 200ºC) temperature range. Circuit breaker no.1 (SB1) was for the heating elements and circuit breaker no.2 (SB2) was for the controller.

Test Conditions

Type J thermocouples were used to measure temperature. The environment was magnesium chloride solution. $MgCl_2$ solutions are more aggressive (with respect to chloride cracking of stainless steels) than other aqueous chloride solutions due to the slight acidity of the solutions (*p*H = 6). The stress sources were residual stress and thermally induced stress. Type 304L stainless steel material was selected, with temperature and solution concentration selected to crack 304L. Figures 4.3 and 4.4 show the temperature and solution concentration ranges relative to regions of susceptibility to stress corrosion cracking.

Chloride concentrations were $1.6X10^5$ ppm chloride (21% $MgCl_2$ solution) and $2.6X10^5$ ppm chloride (35% $MgCl_2$ solution), with average temperatures of 80℃

and 92 ℃ and pH of between 1.1 to 6. Distilled water and hydrochloric acid were used to adjust or maintain the pH during the tests. The solutions were prepared by dissolving $MgCl_2.6H_2O$ (analytical grade) in demineralized water. The solution was left open to atmosphere (in the test rig) to allow the presence of dissolved oxygen. Initially the replenishment was performed using $MgCl_2$ solution (tests 1 and 2) and demineralised water was used subsequently.

The solution *pH* was measured during the tests. To measure *pH*, a solution sample was removed from test rig, cooled down, and then measured at room temperature.

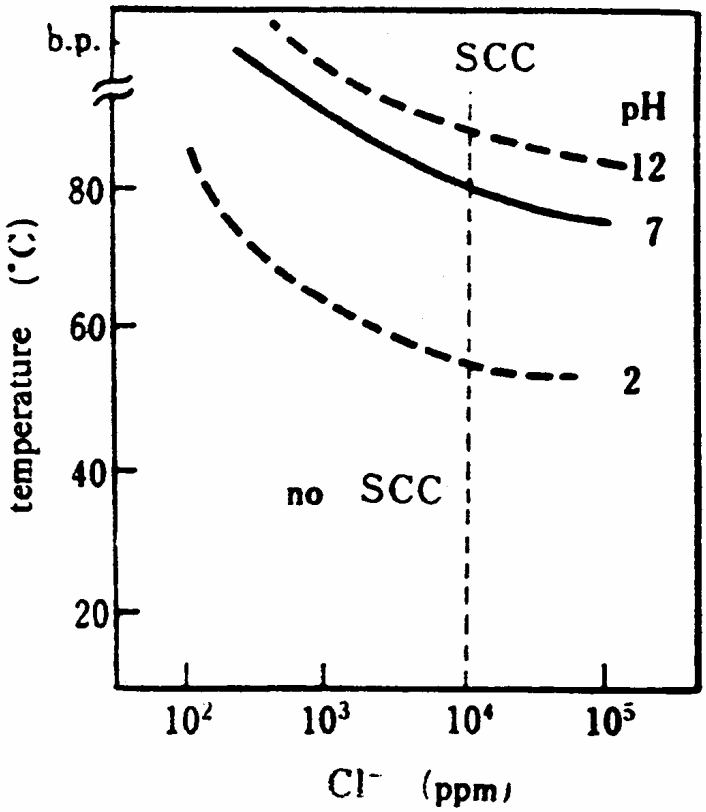

Figure 4.3 The relationship between temperatures and chloride concentrations which lead to stress corrosion cracking of 304 [2]

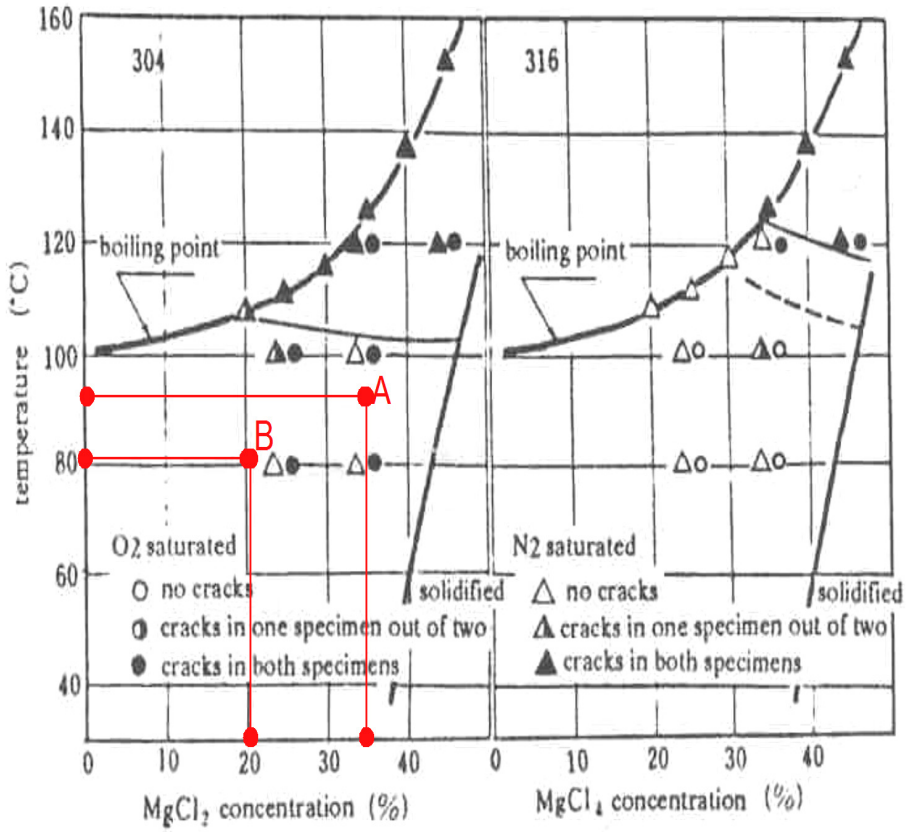

Figure 4.4 The relationship between temperature, chloride concentration and cracking, showing boiling point and solidification of $MgCl_2$ solution [2]

Some samples were grooved by a sharp-tipped machining tool. The sharp tip was used to shave material at localized point to produce a 0.5mm wide and 0.5mm deep triangular groove all around the internal circumference, at the mid point of the sample. The groove served to increase the local stress. The grooved samples are indicated in the test conditions summary as given in Table 4.1.

Table 4.1 Test conditions summary

	Test 1	**Test 2-5**
$MgCl_2$ concentration in solution	21wt%	35wt%
Mass of Cl^- in 100g solution	15.64g	26.06g
Temperature of hollow bar	80°C	90°C, 101°C, 114°C, 127°C
Temperature of the solution	79.96°C	80°C, 83°C, 86°C, 91°C
Tests with bar diameter of 75mm	None	T3A, T3B, T3C, T4A, T4B, T4C, T4D, T5A
Tests with bar diameter of 50mm	T1A, T2A, T2B	T5B, T5C
Grooved samples	None	T4C, T4D, T5B, T5C

The stress intensity at the notch is estimated to be about 4 MPa.m$^{0.5}$, assuming an average stress of 100MPa and a crack of 0.5mm.

4.3 Measurement of strain

Strain gauges were used to measure the elastic strain of the tube test sample. HBM type strain gauges with temperature compensation for steel (α= 10.8X10^{-6}/ºC) suitable for steel of accuracy of about 0.3µm/m were used, with resistance of 120Ω and gauge factor of 2. Full and half Wheatstone bridges were used (full bridge for samples T3A, T3B, T4A, T4B, T4C, T5A, T5B and T5C and half bridge for T3C), see figures 4.5 and 4.6.

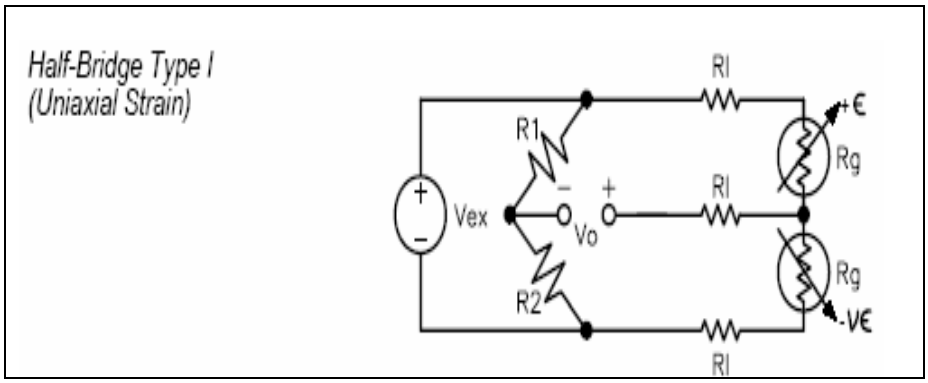

Figure 4.5 Schematic: half Wheatstone bridge [35].

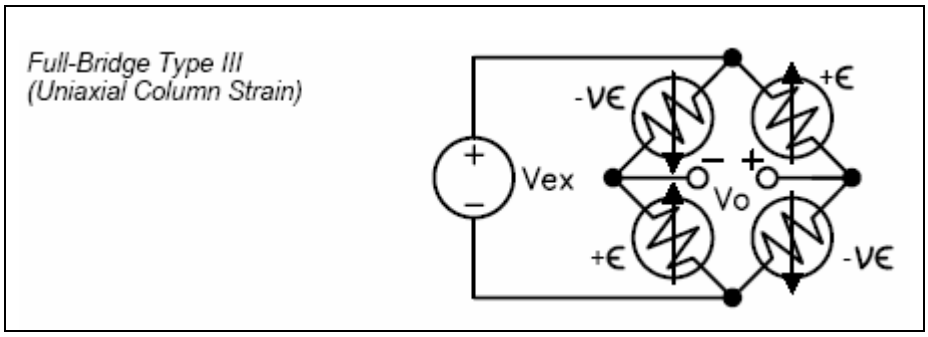

Figure 4.6 Schematic: full Wheatstone bridge [35]

Typical test results of temperature and strain are plotted below in Figures 4.7 and 4.8 respectively. The temperatures measured at the center bar, in the solution and on the outside surface of the sample (as shown in figure 4.1) are plotted in figure 4.7, showing that the temperature differed between these areas and varied over time during testing. The measured strain follows the pattern of temperature variations (see figure 4.8). The oscillations in temperature and strain resulted

from the on-off nature of the controller. Figure 4.9 shows the temperature difference (temperature of the bar minus temperature of tube sample) with time. The significance of this difference is that it is the origin of the thermal stress which was imposed on the tube sample by the bar.

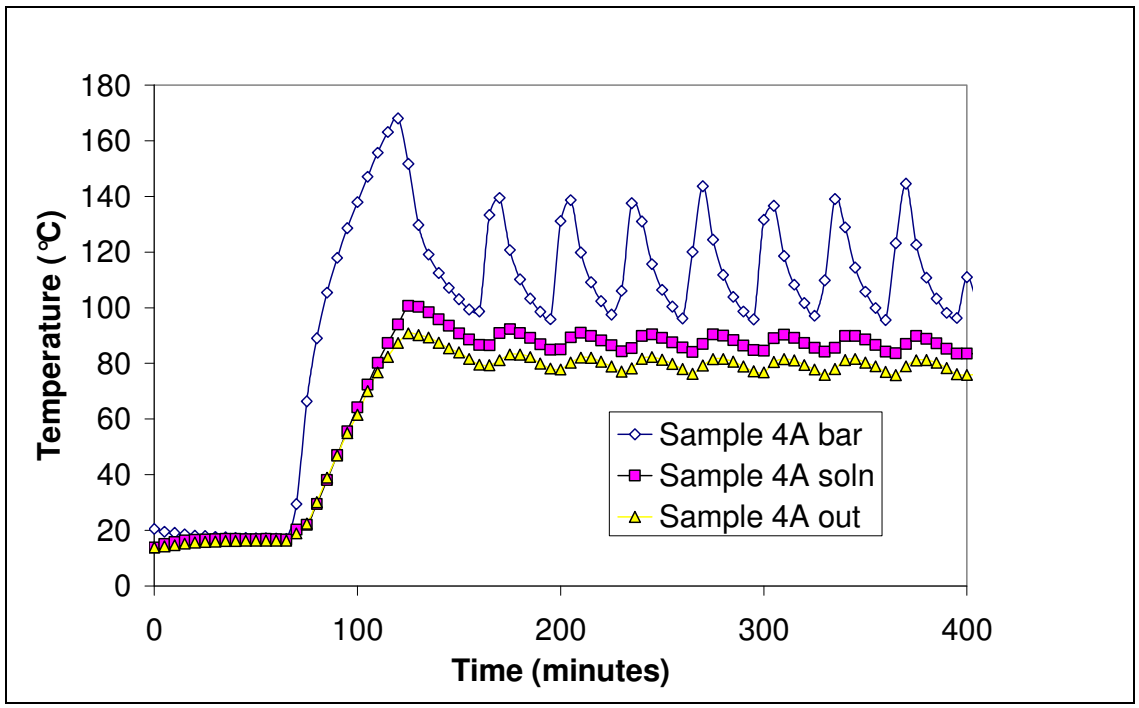

Figure 4.7 Typical temperature results from the experiment (sample 4A shown)

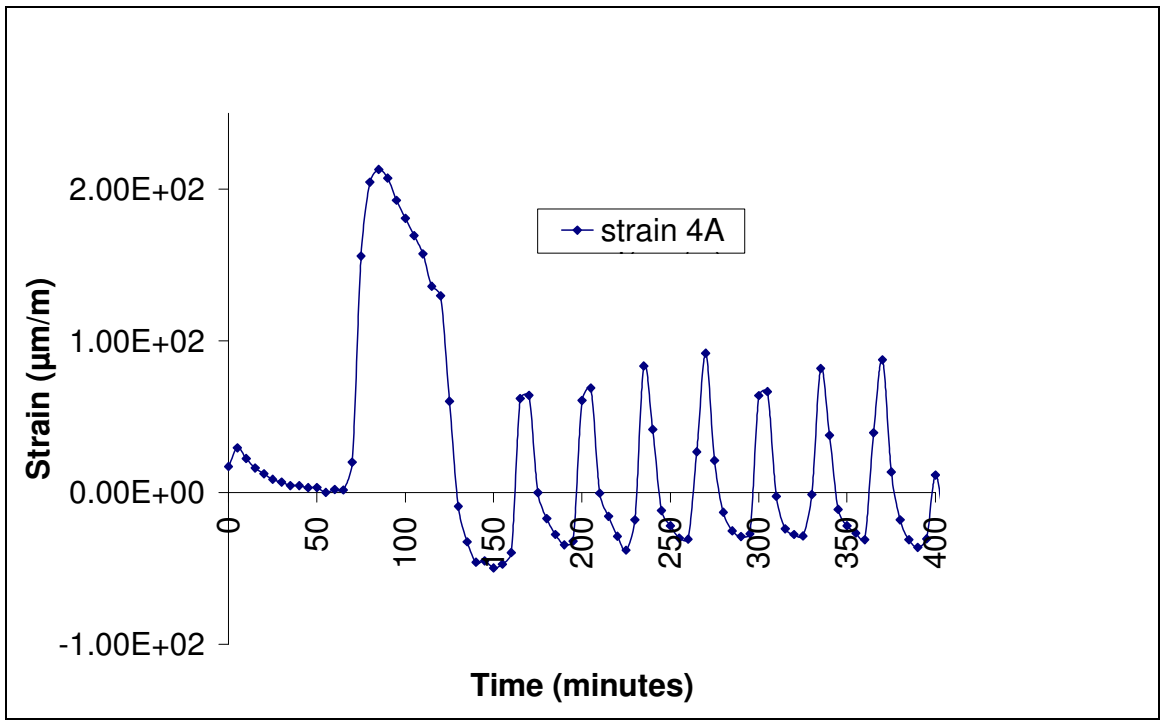

Figure 4.8 Typical strain results from the experiment (sample 4A shown)

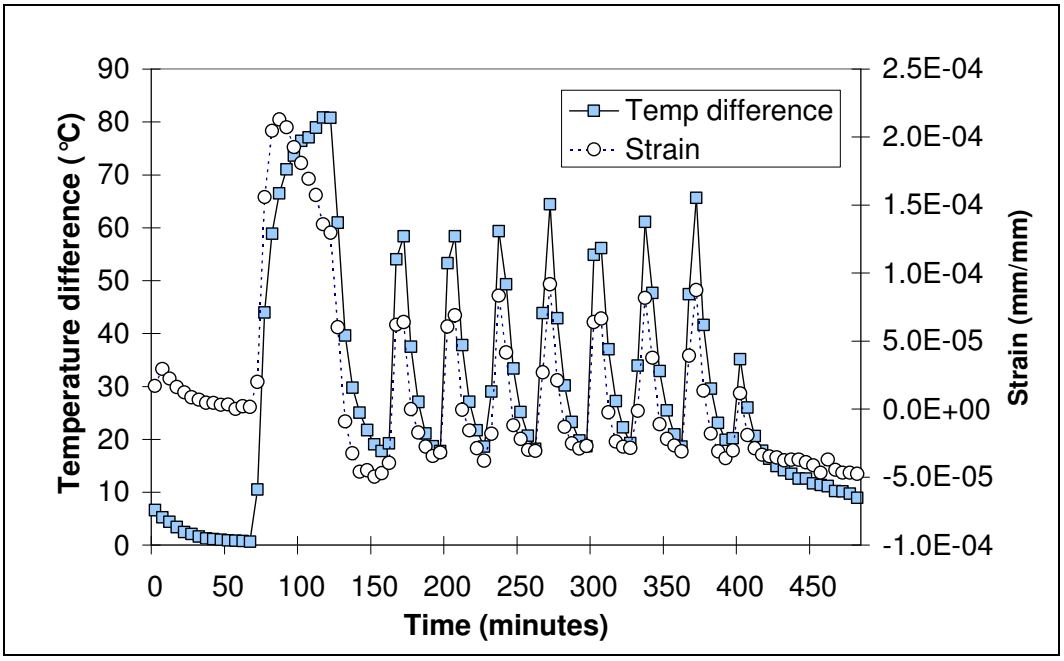

Figure 4.9 Typical temperature difference (bar-sample) and strain variation with time in sample 4A

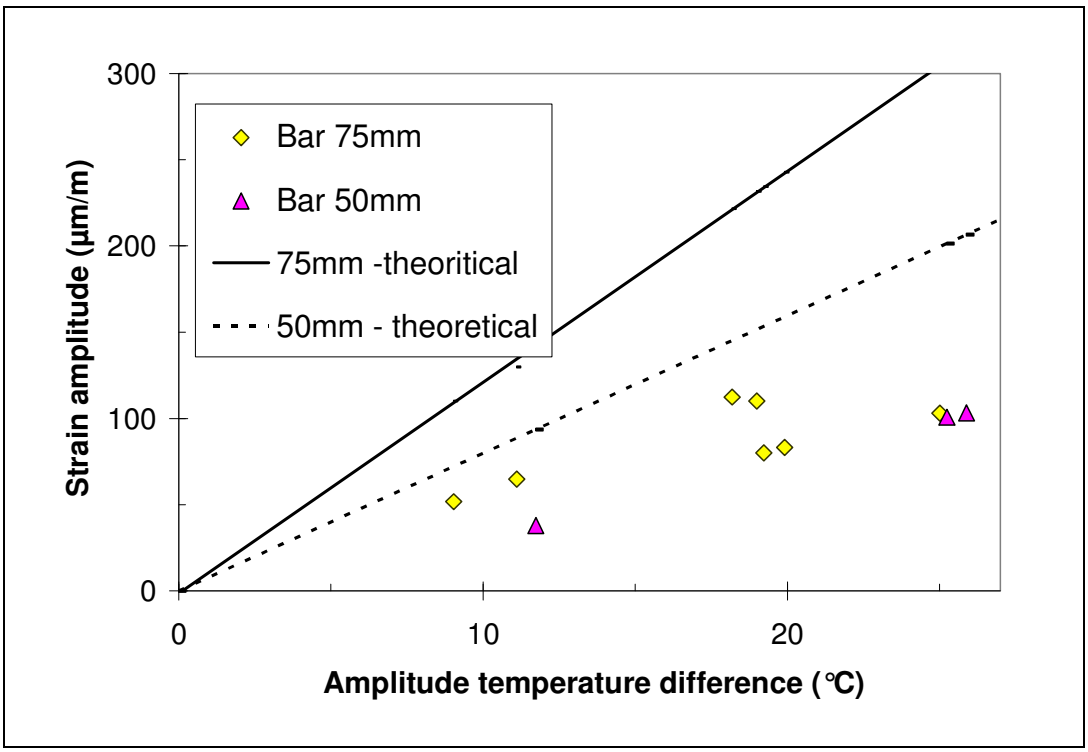

Figure 4.10 Theoretical and actual strain amplitude plotted against amplitude of the bar-sample temperature difference amplitude. Notes on legend: "Bar 50mm theoretical" and "Bar 75mm theoretical" – strain amplitude **predicted** from temperature difference, for samples with Ø50mm and Ø 75mm center bars respectively; "Bar 50mm ave strain" and "Bar 75mm ave strain" – **measured** strain amplitude for Ø 50mm and Ø 75mm center bars respectively.

The strain in the tube (sample) is caused by the temperature difference between the bar and the tube. A simple analytical method can be used to obtain a first estimate of the elastic stress in the tube (sample), as shown below. Comparison of the actual cyclical elastic strain with the predicted values (Figure 4.10) shows the actual values to be approximately half the predicted values. The main reason for this is likely to be flexing of the type 310 flange which connected the bar to the sample; flexing of this flange hence took up some of the thermal strain, resulting in less stressing of the sample. If the flange were rigid, the expected relationship between the bar-sample temperature difference and the stress in the sample is as follows:

$$\sigma/E = \alpha\,\Delta T/(1 + A_2/A_1) \qquad (1)$$

In equation 1, σ is the stress in the tube sample, E is the elastic modulus α is the thermal expansion coefficient, ΔT is the temperature difference between the bar and tube, A_2 is the cross-sectional area of the tube, and A_1 is the cross-sectional area of the bar

This relationship is derived from simple balance of forces, as follows:

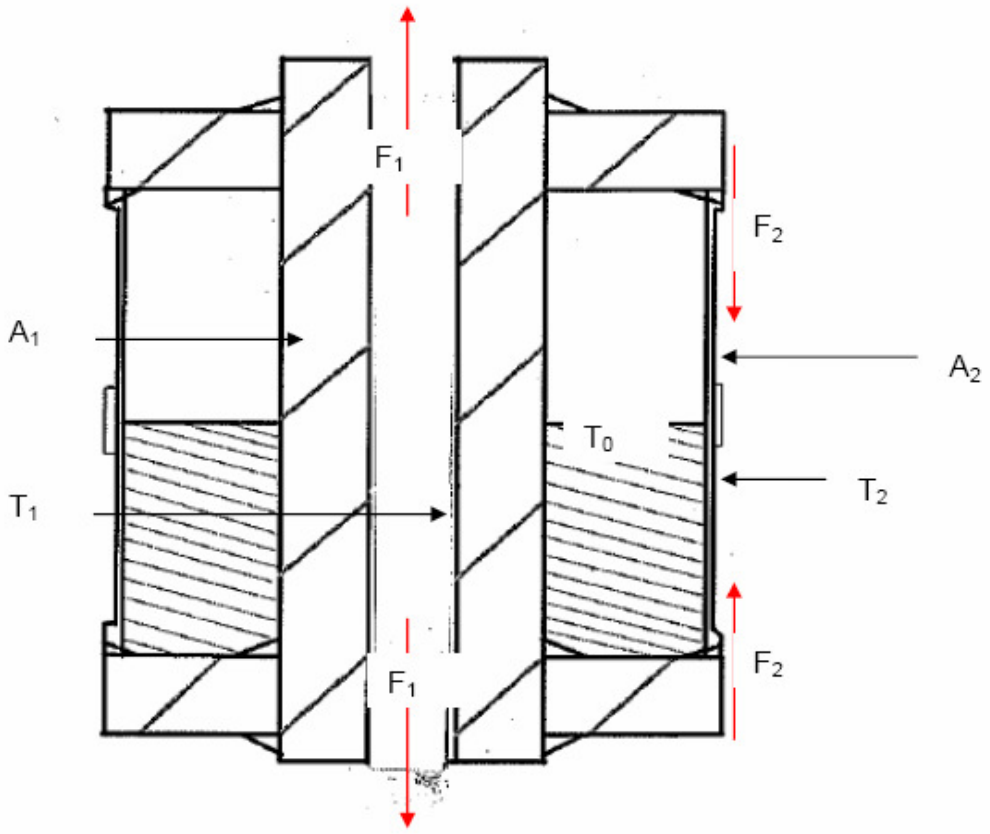

Figure 4.11 Forces acting in the test rig

Let σ_1 be the (compressive) stress in the bar, and σ_2 the (tensile) stress in the tube. Then $\sigma_1 A_1 = -\sigma_2 A_2$, or $\sigma_1 = -\sigma_2 A_2/A_1$

If the end flanges are rigid, then the total strain (elastic and thermal) of the tube and bar must be equal. If T_x is the initial temperature at which the stresses in the tube and bar are zero, the strains can be written as:

$\varepsilon_1 = \sigma_1/E + \alpha(T_1-T_x) = \varepsilon_2 = \sigma_2/E + \alpha(T_2-T_x)$
Substitution of the expression $\sigma_1 = -\sigma_2 A_2/A_1$ then yields
$\sigma_2/E = \alpha(T_1-T_2)/(1+A_2/A_1)$

4.3.1 Predicted Strain and Temperature: finite-element analysis

Finite-element analysis was performed on the test rig to obtain more accurate predictions of the steady-state temperatures and stresses. The analysis was performed by a specialist in structural integrity at Eskom, Mr Ronnie Scheepers.

The following material properties for 304L stainless steel were used for the temperature distribution and thermal stress calculations:

Table 4.2 Physical properties

Thermal conductivity of stainless steel	15 W/mK
Modulus of elasticity	193 GPa
Poisson's ratio	0.24
Thermal expansion coefficient	16.9×10^{-6} °C^{-1}

It was assumed that the central surface temperature (on the inner surface of cylindrical cavity in the bar, next to the heating element) is at 110ºC. Natural convection between the outer surface and surrounding air (at 20°C) was assumed (see figures 4.12 and 4.13). The assumed convection heat transfer coefficient was 5W/m^2°C (table 4.3). Within the sample rig, the thermal conductivity of steam (at 100°C) was used in the freeboard, and that of water (at 93°C) for the solution (table 4.3). Results are presented in figures 4.11 to 4.14.

Table 4.3 Heat transfer constants used

Conductivity of steam top (100℃)	0.0243W/m℃
Conductivity of liquid water (93℃)	0.678W/m℃
Heat flow (interior of bar surface)	0.01 W/mm^2
Convection heat transfer coefficient- top	5W/m^2 ℃
Convection heat transfer coefficient- centre	5W/m^2 ℃
Convection heat transfer coefficient- bottom	5W/m^2 ℃

The calculated thermal stress at the internal surface of the tube was approximately 26 MPa for the 75 mm centre bar, and 22MPa for the 50 mm centre bar (see figures 4.14 and 4.15). The predicted temperatures are comparable with the measured temperatures (as presented later).

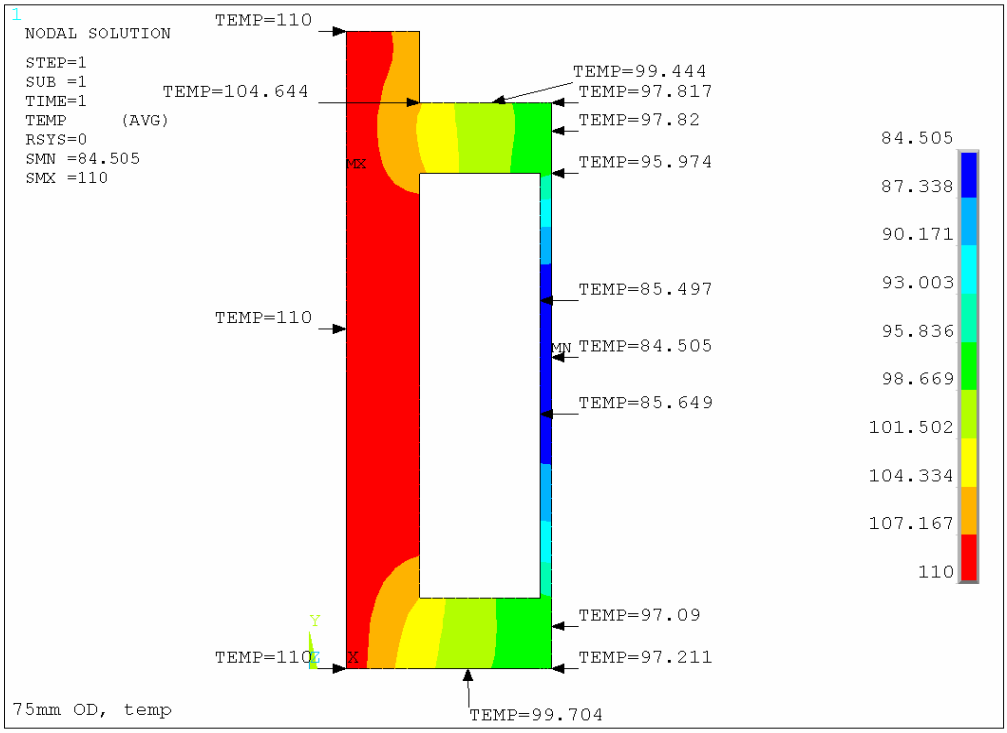

Figure 4.12. Steady state temperature distribution for rig with a Ø75mm centre bar.

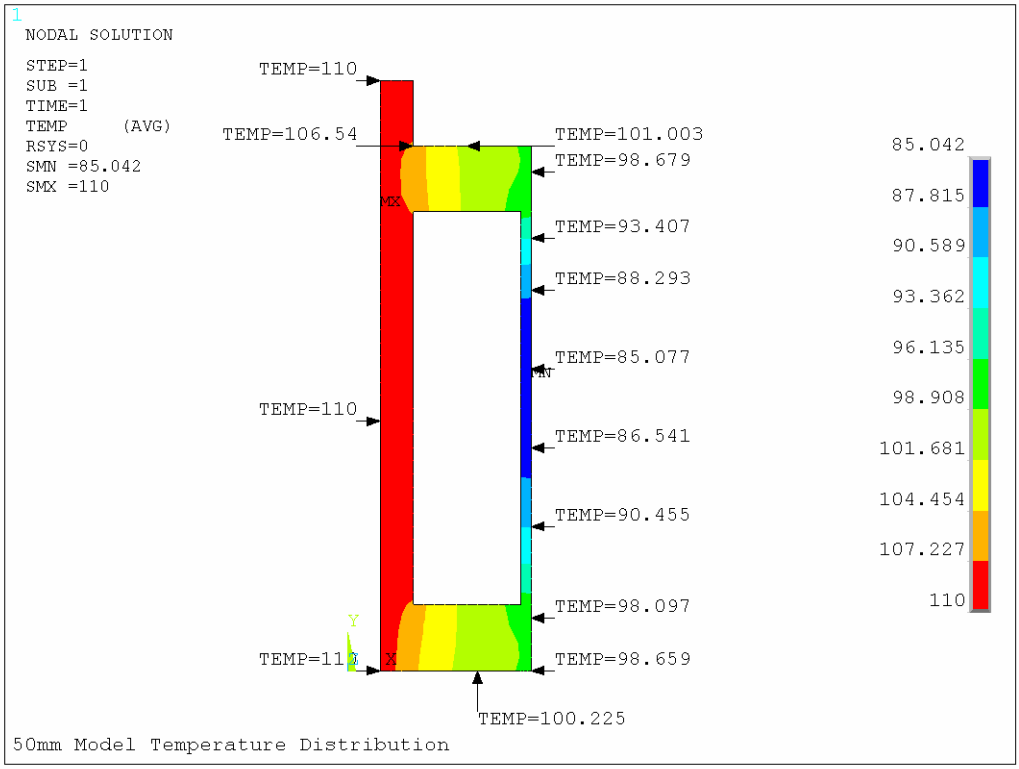

Figure 4.13. Steady state temperature distribution for rig with a Ø50mm centre bar.

Figure 4.14. Steady state stress distribution for a rig with a 75mm diameter centre bar.

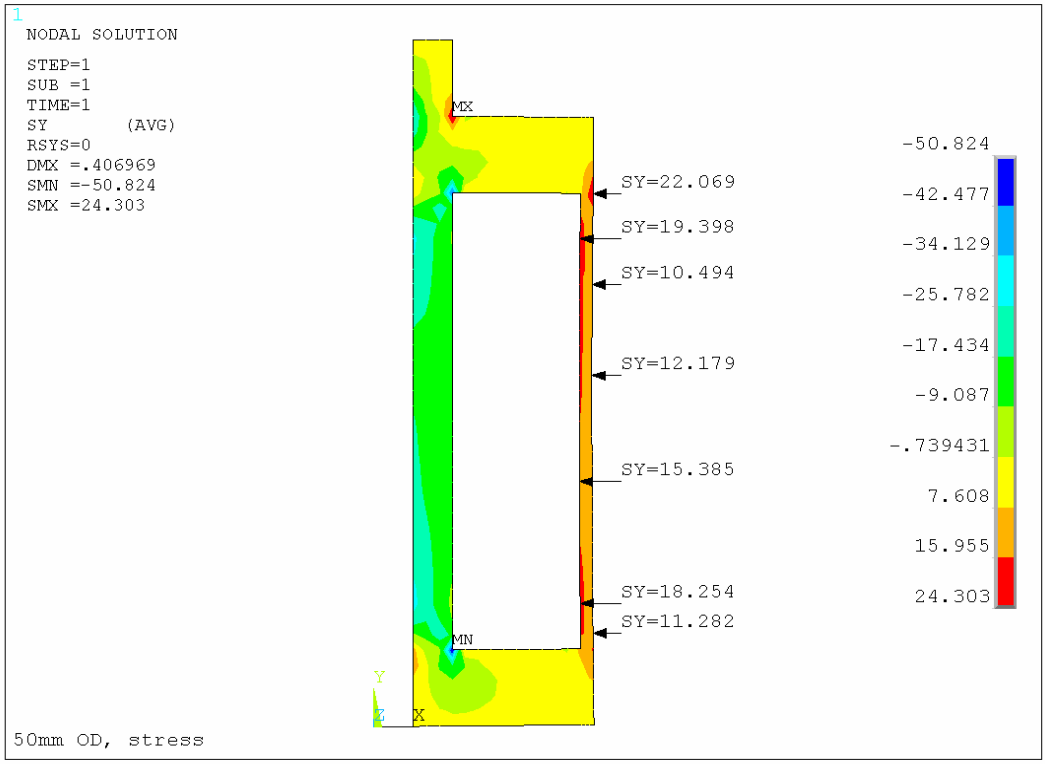

Figure 4.15. Steady state stress distribution for a rig with a 50mm diameter centre bar.

4.4 Mechanical Testing

The tensile properties and hardness of the tube were measured. Mechanical testing was performed according to ASTM standard 307 for flat samples. Vickers hardness tests were performed. The mechanical test results are within specification (DIN X2CrNi 18-9 or EN 10088 no 1.4307) for as-received stainless steel. The average hardness is 85HRB. The ultimate tensile strength was 668MPa and the 0.2% proof strength was 340MPa. The as-received grain size was 40 micron.

4.5 Visual examination and metallography

After testing, samples were examined by scanning electron microscope, stereo and optical microscope to identify the mode of failure, microstructure, and crack density.

The samples were examined visually to detect gross defects (e.g. leakage of solution during the test, indicating a through-wall crack). The evidence was

recorded and photographed. Stereo microscopy supported visual examination. Visual examinations and stereo microscope analysis of cracked or failed samples were performed on external and internal surfaces, and observations recorded. The bar and flange were also examined for cracks and noted. The cracks were classified as being through-wall or non-through-wall and surface cracks were counted. Cross-sectional evaluations of cracks were performed at selected positions, measuring crack depths (see figures 4.16 and 4.17).

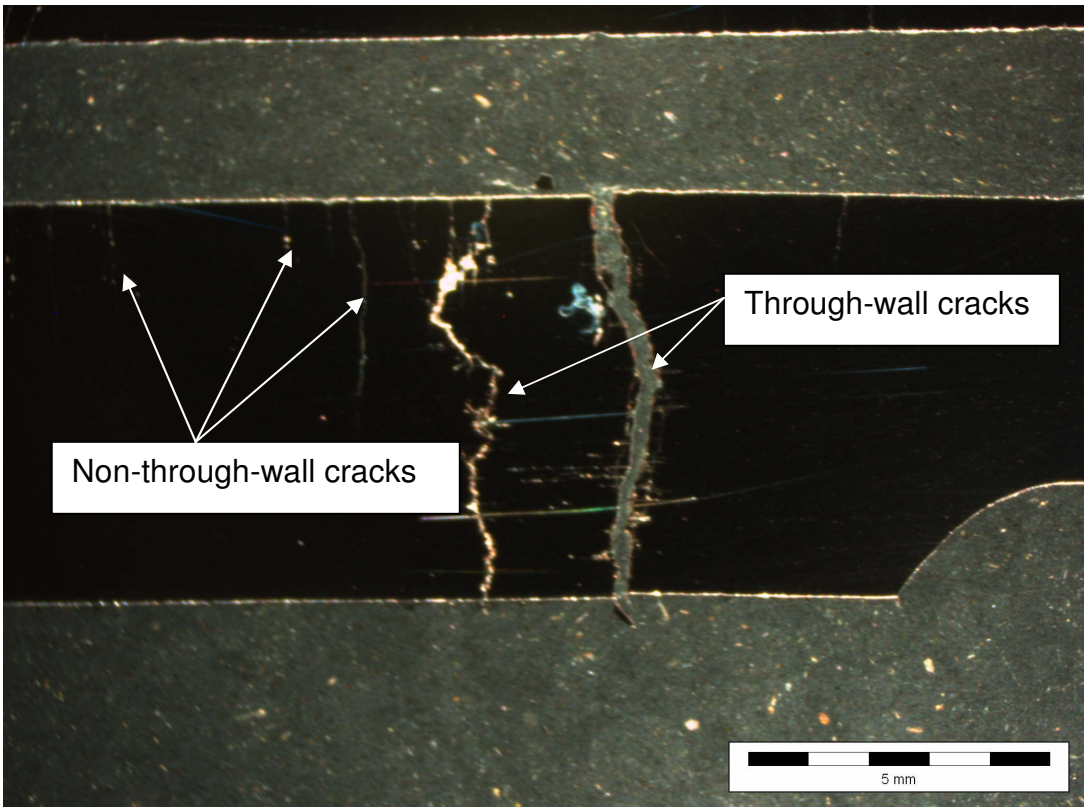

Figure 4.16 Typical stereo microscope image of type 304L stainless steel sample (cross-section) after testing

Metallographical evaluation was performed on polished cross-sections of the polished samples; cracks were counted and documented. The crack morphology was evaluated.

Scanning electron microscopy (SEM) was used for fracture analysis at higher magnification.

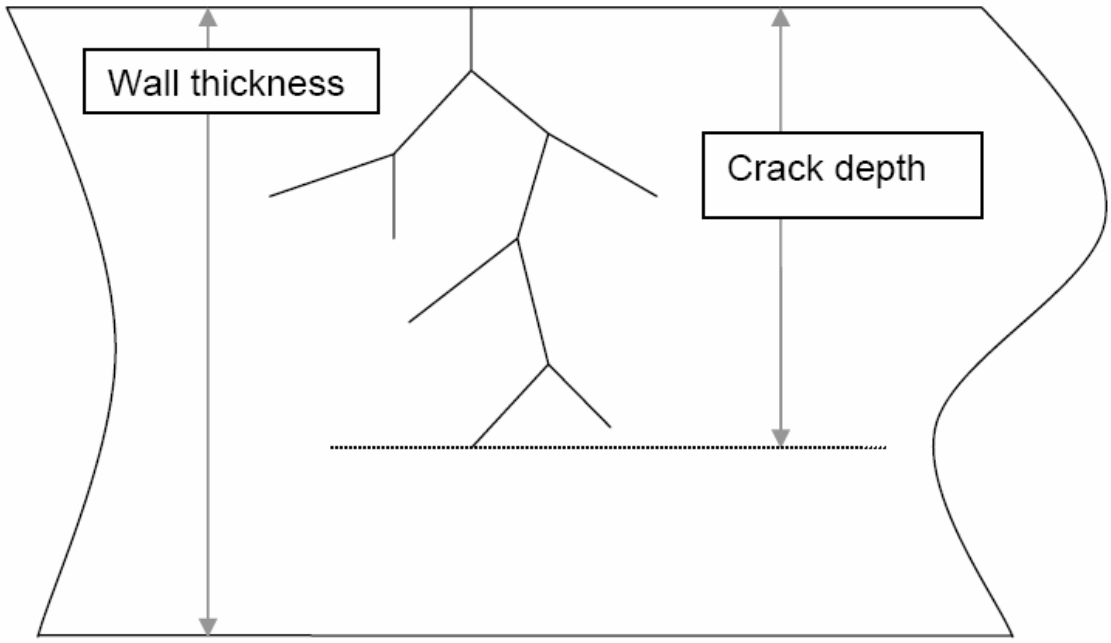

Figure 4.17 Measuring crack depth

Chapter One

1. Background and SCC issues or challenges

1.1Introduction

Type 304/304L stainless steel is widely used, for example in the nuclear power and brewery industries and at swimming pools as roof fasteners and rods. These stainless steels can suffer from chloride induced stress corrosion cracking (SCC), corrosion fatigue, as well as pitting and crevice corrosion in the presence of chloride. Chloride stress corrosion cracking does occur on austenitic stainless steel components and poses a danger which can result in catastrophic failure. Other types of corrosion act as initiation points and stress raisers for chloride stress corrosion cracking [1].

The aim of this project was to provide cracked samples of defined geometry for a larger stress corrosion cracking repair project, aimed at the *in-situ* repair of the cracked components.

1.2 SCC

Stress corrosion cracking is the environmentally assisted cracking of ductile material in an apparently brittle manner under tensile stress. Type 304L stainless steel in an aqueous chloride solution, under tensile stress, (residual stress and/or operational stress), can undergo stress corrosion cracking. The crack morphology could be transgranular, intergranular, and branched [2, 3]. Crack direction is mainly perpendicular to the load or stress.

1.3 Operational experience/Historical Background and Current state

During plant maintenance inspections are performed to identify defects or damage, and to verify the integrity of components. Stress corrosion cracking is one of the forms of damage which is detected by inspection of or leakage from components. Depending on the extent of defects, replacement or repair can explored. Tungsten inert gas arc welding and recently also laser and friction welding have been researched as repair methods [1, 4]. In one example, overlay

weld repair was performed on a brew kettle; however due to shallow weld repair, the crack was not fully sealed (a notch was still present) and further crack propagation caused the weld repair to leak [1].

1.4 Problem statement and Research questions

Stress corrosion cracking can be costly where plant damage occurs and much more so when lives are lost. An example of the latter was the collapse of indoor swimming pool roofs. The roof had been supported by stainless steel (SS) rods in tension [5,6,7,8]. In the brew kettle example, initial cracking and subsequent leaking of the weld repair affected down time of the plant [1]. When the cost of replacement is high, possible repair is investigated, but samples or test rigs are required for testing of the repair procedure. As background to this project, a need for researching possible repair processes was identified; this project focused on the production of cracked samples that represent the in-service condition. The final practical aim (which is outside the scope of this project) is to perform repair *in-situ*, while liquid is leaking from the cracked vessels.

Research questions

- Can chloride stress corrosion cracking be produced in a controlled manner under controlled conditions, to provide samples to test the repair procedure?
- How does residual stress from manufacturing and fabrication influence cracking?
- What is the influence of both static and cyclic thermal stresses on stress corrosion cracking?

1.5 Rationale for study and Research objective

This research forms part of the repair project and is to supply the non-standard samples to be used in the simulated repair process, so contributing to the development of in-service weld repair of stress corrosion cracks. Repair is seen as a way to avoid replacement costs and also to help in managing the shortage of special alloys.

Chapter Two

2 Brief Literature review on Stress Corrosion Cracking

2.1. Introduction/SCC Overview

Austenitic stainless steels can undergo chloride stress corrosion cracking in chloride solutions under tensile stress. The combination of tensile stress and an aggressive environment can cause cracking even though the stresses are below the yield strength. Chloride induced stress corrosion cracks are branched, with the macroscopic path normal to the applied tensile stress. Anodic dissolution does plays a significant role in crack growth [2, 9]. Stress corrosion cracking generally occurs at temperatures between 50ºC to 350ºC [10]. Solution treated, unsensitised austenitic stainless steel has mainly transgranular crack paths, while cracks in sensitised austenitic stainless steel are intergranular. The fracture surface of stress corrosion in region I and II are transgranular, intergranular or both while region III fracture surface is of made microvoids coalescence. At low K_I close Kiscc the crack morphology is transgranular. SCC anodic dissolution and crack growth require activation energy [11].

Factors that influence Stress Corrosion Cracking

- Constant or fluctuating temperature (which can affect the stress in the material)
- Oxygen levels in the solution
- Single phase or dual phase (steam-vapour, water-liquid or both) environment (dry and wet)
- Concentration of minor and major solution species. For example, a $MgCl_2$ solution is more aggressive than NaCl and $CaCl_2$ solutions [2]
- Acidity (*p*H) of the solution
- Electrochemical conditions, such as galvanic coupling or applied cathodic protection
- Composition and microstructure of the material; this was not studied here since the aim was to produce samples which simulate the actual components (which are of Type 304 stainless steel).

The conditions required for stress corrosion cracking to occur are a susceptible alloy in a specific environment in the presence of tensile stress; see Figure 2.1.

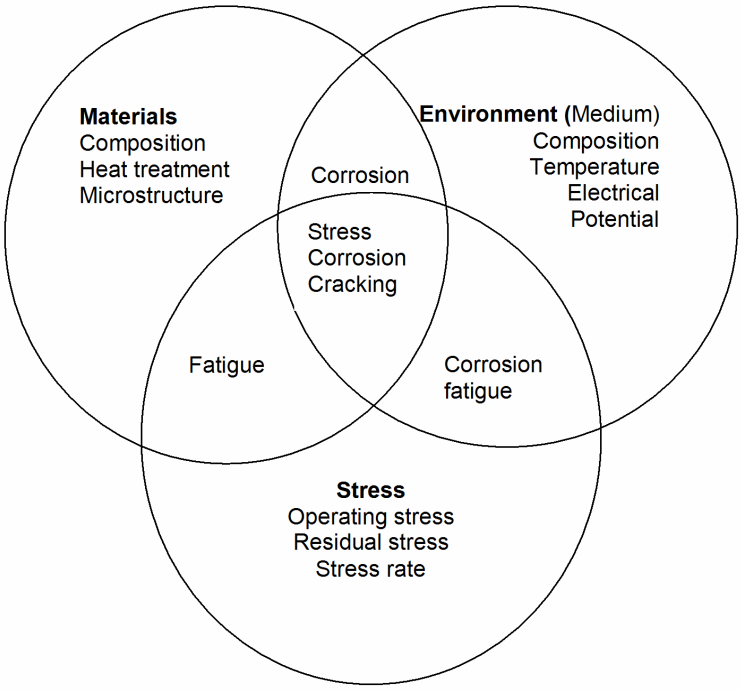

Figure 2.1 Three conditions are to be present for SCC to occur, namely environment, tensile stress and a material which is susceptible [9].

Environments that promote stress corrosion cracking of austenitic stainless steel are the following [9]:

- Chlorides, both inorganic and organic
- Caustic solutions
- Sulphurous and polythionic acids

2.1.1 Mechanism of chloride Stress corrosion cracking

Several mechanisms for stress corrosion cracking have been proposed; a useful review of these is given by Jones and Ricker [12]. In the case of chloride cracking of stainless steels, the mechanism must account for the cleavage-like nature of the failure; this has been taken to imply a role of mechanical failure in crack growth [13]. However, the nature of this mechanical role is not clear. In the mechanism of film-induced cleavage [14], corrosion produces a surface product layer which can inject cracks into the underlying metal. Such a surface film was found by transmission electron microscopy of chloride cracks in austenitic stainless steel [15]. In applying this idea, Nishimura [16] proposed that crack growth occurs when the stress at the crack tip reaches a critical value, which is independent of the corrosive environment; the proposed role of the

environment is to change the rate at which the local stress at the crack tip increases as a result of corrosion – but there appears not to be direct experimental evidence for the constancy of the fracture stress, and the effect of environment on the rate of stress increase. In contrast with the proposal that the stress corrosion crack grows by brittle failure, it has also been suggested that plasticity is enhanced at the crack tip [17].

The lack of a generally accepted mechanism for chloride cracking of austenitic stainless steels is a difficulty in the present work, because there is no single theoretical framework which can be used to explain the experimental observations.

2.1.2 The transgranular crack advancement in cleavage manner

As is already established that transgranular SCC occur by intermittent microcleavage event due to a thin film. The increments are about 0.5µm long Sieradzki, et. Al. and Pugh are in agreement [10, 18]. The mean cracking velocity is estimated to be 0.1µm.s^{-1} and it was consistence with spacing of crack front striations.

Transgranular SCC appears to propagating by discontinuous cleavage. Blunted crack is continues by cleavage crack the blunted due to lagging of step formation velocity behind the cleavage crack tip, which continues after crack arrest forming a ligament thus blunt crack tip. When stress transferred back to tip the environment reinitiate the cleavage crack after blunting [18].

The Cottrell – Lomer lock allows dislocations to pile up on each of the {111} planes and eventually crack will be formed on (110) plane [10]. The film is reformed because of environment, a brittle crack can initiate under thin film (oxide, de-alloyed layer and hydride) advance for short distance in cleavage manner in substrate where after step formation is completed then the environment reinitiate the cleavage crack [18].. Dislocations are allowed to pile up on lock until cracking again. When two slipping planes are equally stress, the stress required to nucleate a crack in the film may by roughly estimated that is

the crack driving force [10]. The film formation determines the time between crack growth events. The film mismatch and thickness influence discontinuous cleavage crack growth.

Early proposed cause of cleavage cracking was Hydrogen Embrittlement, Adsorption and Selective dissolution but from selective dissolution film–induced cleavage was deduce and it seemed more suitable [18].

2.2 The conditions required for SCC to occur; other factors that affect SCC

The main factors are summarised in Table 2.1

Table 2. 1 Material, environmental and mechanical factors that influence stress corrosion cracking [19].

Material Factors	Environmental Factors	Mechanical Factors
Composition Microstructure Contaminants or impurities Grain size Grain orientation	Temperature pH Electrochemical Potential Solute species Solute concentration Oxygen concentration	Stress Strain rate

2.2.1 Environmental effects

Short discussions on the major environmental effects are presented below.

Dissolved Oxygen

The time to failure in an oxygenated environment is shorter, as shown in Figure 2.2 which compares cracking in oxygenated and nitrogen purged chloride solutions. The greater severity of cracking in the oxygenated solution supports the role of anodic dissolution in crack growth.

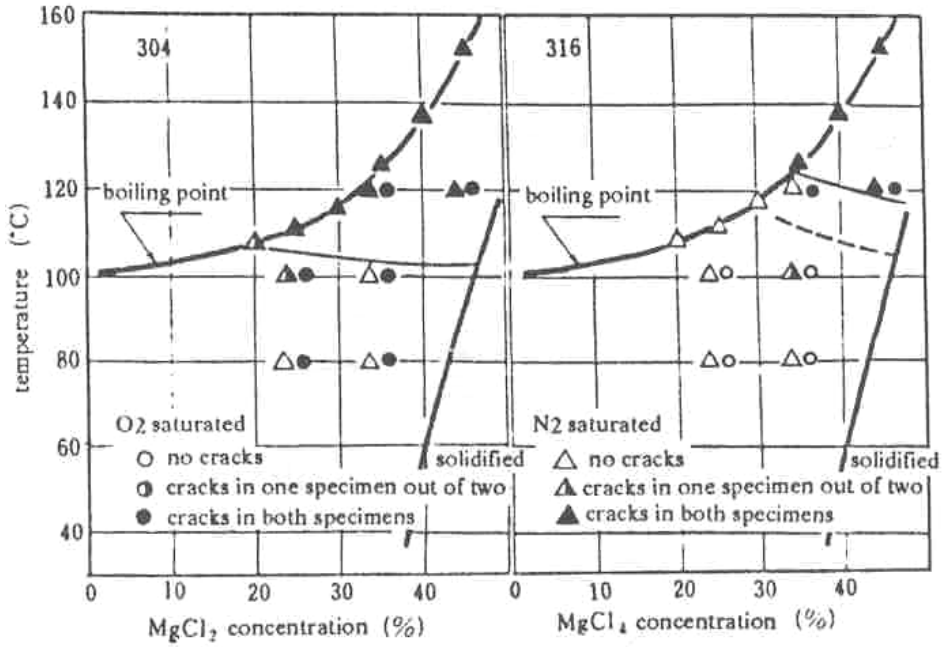

Figure 2.2 Susceptibility to SCC of Types 304 and 316 stainless steel in oxygen-saturated and nitrogen-saturated $MgCl_2$ solution (U-bend test) [2]

Acidity (pH)

If the *p*H is below 2, uniform corrosion can predominate, but recent work shows that chloride stress corrosion cracking does occur at low pH at room temperature [20]. In general, the time to failure is longer at higher *p*H. [2, 19]

Temperature effect

At higher temperature, the time to failure is shorter. The crack initiation time and crack propagation time are not that easy to distinguish experimentally. The total time to failure is mostly reported. Kowaka [2] showed the apparent activation energy to be between 54 and 96 kJ/mol (figure 2.3).

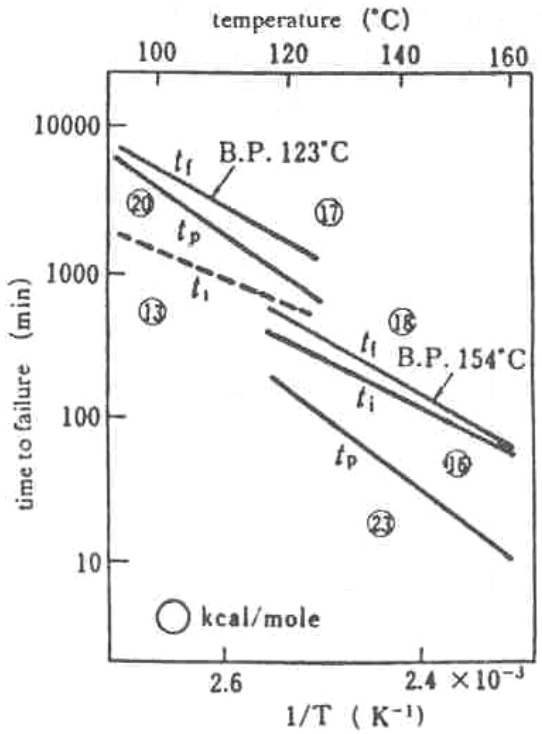

Figure 2.3 Effect of temperature on stress corrosion cracking of Type 304 stainless steel in $MgCl_2$ [2]

Chloride Solutions

$MgCl_2$ solution is more aggressive than sodium chloride (NaCl) solution with regards to stress corrosion cracking [2]. All other chloride salts are less severe compared with $MgCl_2$ and NaCl [2]. However, the chloride activity is more significant than cation influence. Chloride concentration affects the time to failure: high concentration reduces time to failure while low concentration prolongs time to failure.

Effect of Potential

Stainless steel behaves differently at different potentials, depending on the presence and stability of the passive layer, as illustrated by figure 2.4. In this figure, regions I, II and III are where the passive film is unstable, and where active-passive corrosion-resistant alloys can be expected to be susceptible to stress corrosion cracking. The passive film is assumed to be a prerequisite for stress corrosion cracking [9]. Stress corrosion cracking occurs in narrow potential ranges, with pitting corrosion predominating at more positive potentials.

Corrosion pits can serve as initiation points of stress corrosion cracks because of the stress concentrations at pits.

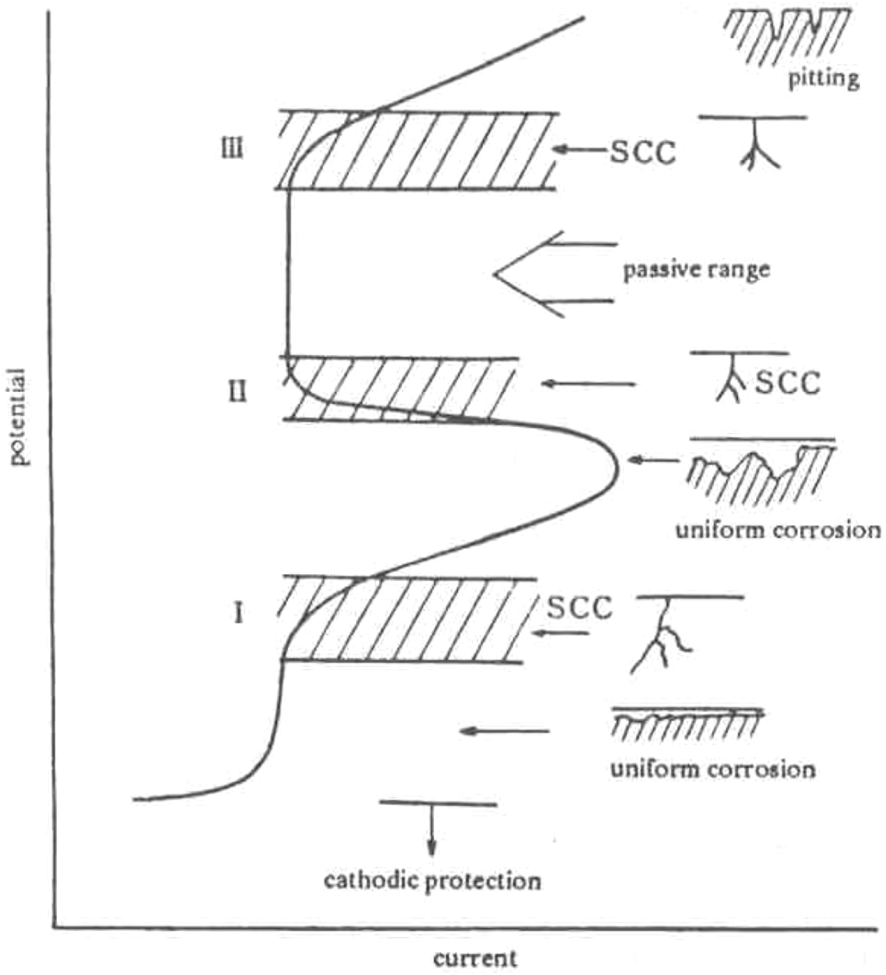

Figure 2.4 Schematic anodic polarisation curve showing zones of susceptibility to stress corrosion cracking [9]

2.2.2 Stress

The presence of tensile stress is essential for stress corrosion cracking. In most instances, metals are subjected to tensile stress in service, often in the presence of residual stresses caused by welding or/and forming. The residual stresses can be comparable with the proof stress and can cause cracking [2]. The magnitude of the stress affects time to failure (Figure 2.5).

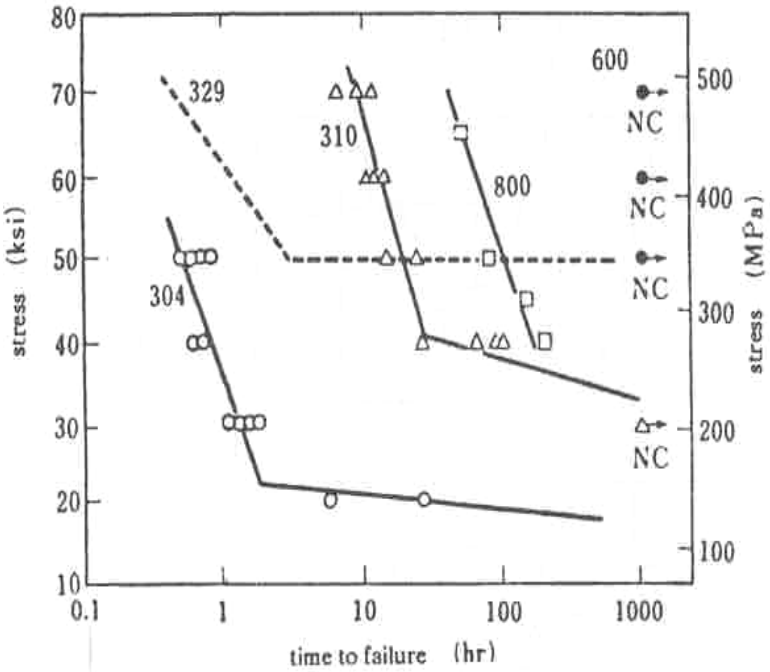

Figure 2.5 Effect of stress on SCC of several materials in boiling 45% $MgCl_2$ at 154°C (see figure 6.16 pp 361 of reference [2]).

2.2.3 Effect of Metallurgical factors [2]

Factors such as alloying elements, grain size, cold work, and surface condition of the material influence stress corrosion cracking. Alloying elements effects can be detrimental, variable or beneficial for stainless steel. For example Ni, C and Si have positive effects in reducing susceptibility to stress corrosion cracking while Cr, P and N increase susceptibility to stress corrosion cracking. The table below summarises the effects of alloying elements on the susceptibility of stainless steel to stress corrosion cracking. The temperature influences the effect of each alloying element on susceptibility to stress corrosion cracking. Some alloying elements are beneficial, some are detrimental, and others do not have any effect. Susceptibility of stainless steel is shown in by figures 2.6 and 2.7 as a function of nickel content. At low nickel levels (ferritic stainless steel) and high nickel levels (nickel alloys) resistance to stress corrosion is improved. Certain levels of silicon can increase the resistance of stainless steel to stress corrosion cracking (see figure 2.8). The combination of phosphorus and nitrogen should be well controlled not to compromise the stress corrosion properties of austenitic stainless steel (figure 2.9). Molybdenum addition increases the threshold stress

intensity of stainless steel, improving the stress corrosion cracking resistance of Fe-Ni-Cr alloys [21].

Table 2.2 The effect of alloying elements on cracking of stainless steel in various environments [2,21]

Element	Boiling 45% $MgCl_2$	Boiling 35% $MgCl_2$
C	O	O•
Si	O	O
Cr	X	□
Mo	X	O
Cu	X	O
P	X	X
N	X	X
Ni	O	

Remark O: beneficial X: detrimental □: no appreciable effect
•: effective in inhibiting transgranular cracking

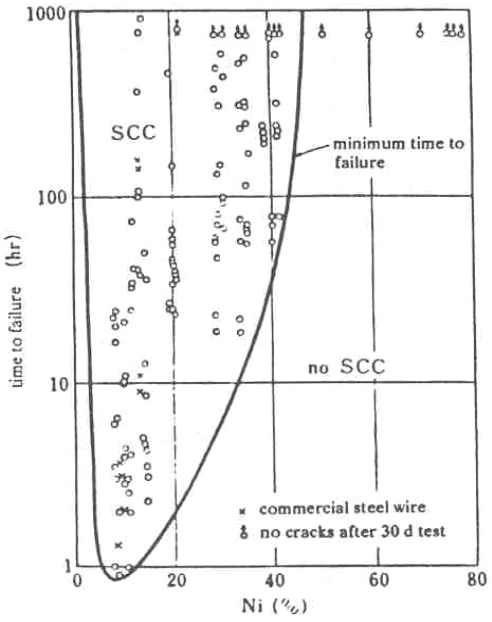

Figure 2.6 Effects of Ni content on SCC of stainless steel in boiling 42% MgCl2 [2]

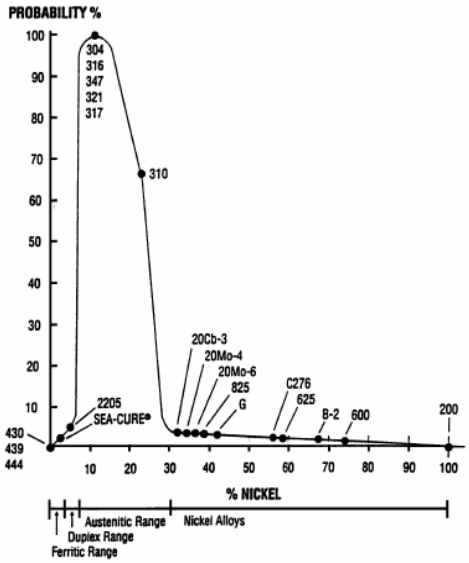

Figure 2.7 Probability of stress corrosion cracking as function of the alloy's nickel content [1]

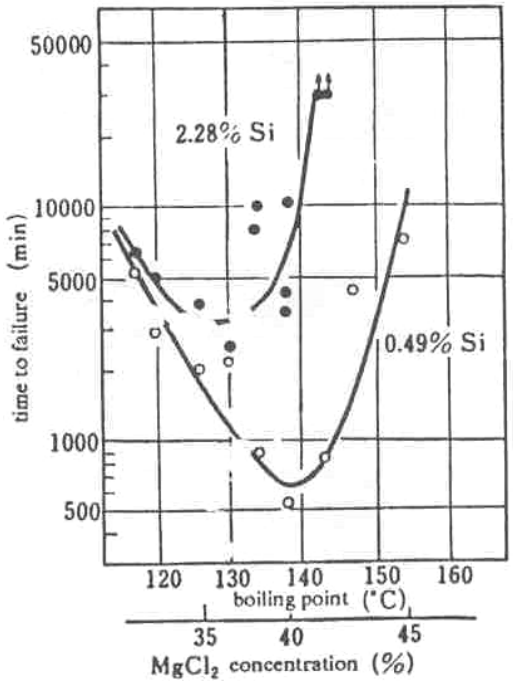

Figure 2.8 Effects of Si on SCC of 17Cr-13Ni stainless steel in various boiling $MgCl_2$ solutions at a constant load of 245MPa [2]

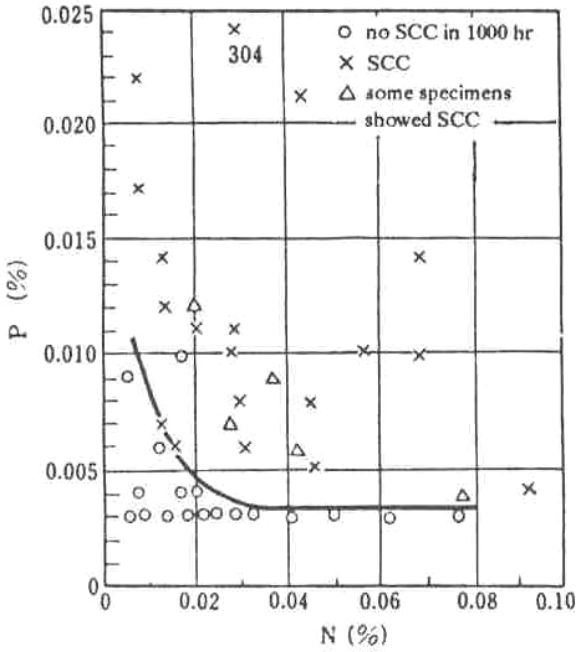

Figure 2.9 Effects of P and N on SCC of 17Cr-13Ni stainless steel in various boiling $MgCl_2$ solutions at a constant load of 245MPa [2]

Grain size has a minor effect on transgranular stress corrosion cracking. Larger grain size plays a role in intergranular stress corrosion cracking (of sensitised steels) in the formation of a galvanic cell, where the grain boundary is the anode while the rest of the grain is the cathode.

Surface finish affects susceptibility to stress corrosion cracking. Surface defects or notches can act as pre-existing defects to initiate cracks.

2.2.4 Corrosion fatigue and Stress Corrosion Cracking

The importance of possible cyclical stressing effects in this project is that the temperature control method which was applied inherently caused the stress to be non-static. Mechanical fatigue occurs in non-corrosive environments under cyclic stress; in corrosive environments the fatigue strength is generally reduced [21], and the corrosion-assisted fatigue life is lower than fatigue life in air (see figure 2.10). The factors which influence corrosion fatigue and stress corrosion cracking are tabulated in table 2.4 and some of the factors are discussed in this section.

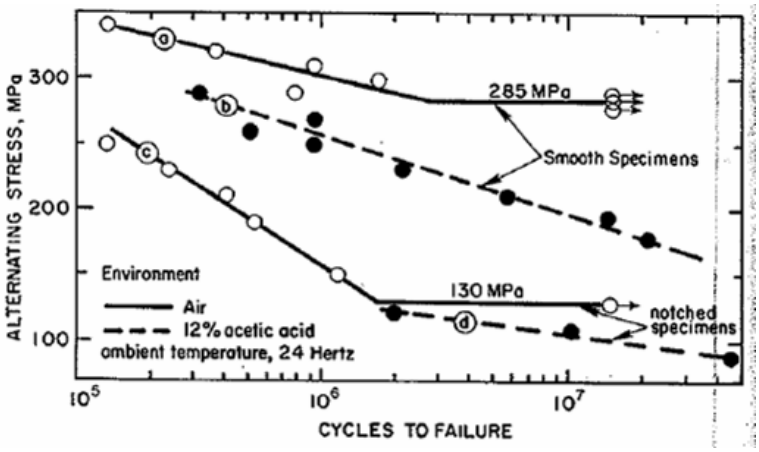

(i)

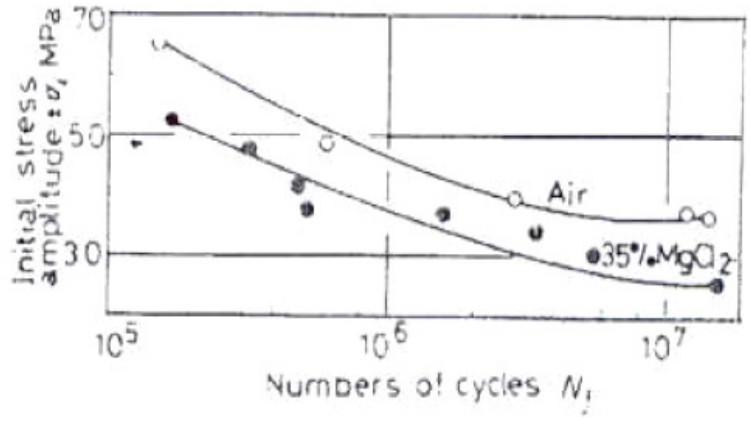

(ii)

Figure 2.10 Effect of corrosion to lower the fatigue limit of (i) 316 in air and acetic acid and (ii) 321 in air and $MgCl_2$ solution [21,22]

Table 2.3. Factors Affecting Corrosion Fatigue [23, 19]

Metallurgical	Environmental	Mechanical	Geometrical
• Alloy composition • Microstructure and crystal structure • Heat treatment • Grain boundary structure • Grain shape and size • Surface texture • Distribution of alloy elements and impurities • Deformation mode (slip character, twinning, cleavage) • Mechanical properties (strength, toughness, etc.)	• Type of environments (gaseous or liquid) • Partial pressure of damaging species in aqueous or other liquid environments • Concentration of damaging species in aqueous or other liquid environments • Temperature • pH • Electrochemical potential • Viscosity of the environment	• Fatigue load frequency • Fatigue load ratio • Fatigue load waveform • Maximum stress-intensity factor and stress-intensity factor range • Load interactions in variable amplitude loading (over/ under/spectrum load) • Residual stress	• Crack size • Crack geometry • Specimen thickness (plane strain versus plane stress)

2.2.4.1 Comparing Stress corrosion cracking with Corrosion fatigue [24]

Stress corrosion occurs in specific environments for a specific material while corrosion fatigue happens in any corrosive environment. Tensile loading is required for both situations, but the stress ratio (the ratio between the minimum and maximum stresses) distinguishes the two mechanisms. Temperature increases crack growth rates of both stress corrosion and corrosion fatigue cracking. In stress corrosion cracking both failure modes are present (intergranular and transgranular) and in corrosion fatigue generally only transgranular. The corrosion fatigue crack generally contains corrosion product but stress corrosion cracks generally do not show any corrosion product. The corrosion fatigue fracture surface can show beach marks and striations, and the

fracture surface of stress corrosion is cleavage-like. Cathodic protection suppresses both cracking mechanisms (see table 2.5).

The morphology of cracking of chloride SCC (of non-sensitised material) and corrosion fatigue are both transgranular, but stress corrosion cracks are more branched [24]; see Figures 2.11, 2.12, 2.13, 2.14 and 2.15 for examples.

Corrosion fatigue is similar to stress corrosion cracking in that the presence of a corrosive solution induces apparently brittle fracture in alloys that are normally ductile. The crack propagates perpendicularly to the principal tensile load for both. However, corrosion fatigue requires neither a specific corrodent nor a very low corrosion rate, and acts on pure metals and alloys. Corrosion fatigue propagates at a low rate so corrosion product is likely to be present in the crack [9].

Strong mixing occurs between the crack tip solution and solution from other parts of the corrosion fatigue cracks [25] due cyclic loading (and the resulting pumping action), in contrast with the static situation for stress corrosion cracking.

Table 2.4. Characteristics of Environmentally-Assisted Cracking [26, 9, 2]

	Stress Corrosion Cracking	**Corrosion Fatigue**
Stress	Static tensile	Cyclic and tensile
Aqueous corrosive agent	Specific to the alloy	Any
Temperature	Increases	Increases
Pure metal	Resistant	Susceptible
Crack morphology	Transgranular, Intergranular, Branched	Transgranular, Unbranched, Blunt tip
Corrosion products in cracks	Absent	Present
Crack surface appearance	Cleavage-like	Beach marks and/or striations
Cathodic protection	Suppresses	Suppresses

2.2.4.2 Effect of Stress

Placing a specific material such as type 304L stainless steel under cyclic or alternating stress in a corrosive environment, particularly chloride or sulphide solutions, can result in corrosion fatigue (while stress corrosion cracking occurs under static stress in same corrosive environment) [21,24,27].

Cyclic loading under cracking conditions need not accelerate crack growth: movement of the flanks of the crack can serve to expel (pump) the solution within the crack, and decrease concentration differences between the crack interior and bulk solution. [24, 25]

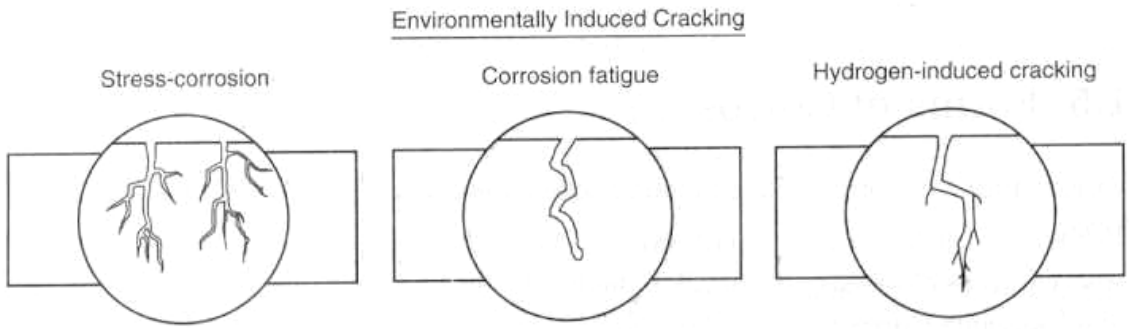

Figure 2.11 Cracking morphology of SCC and CF [9]

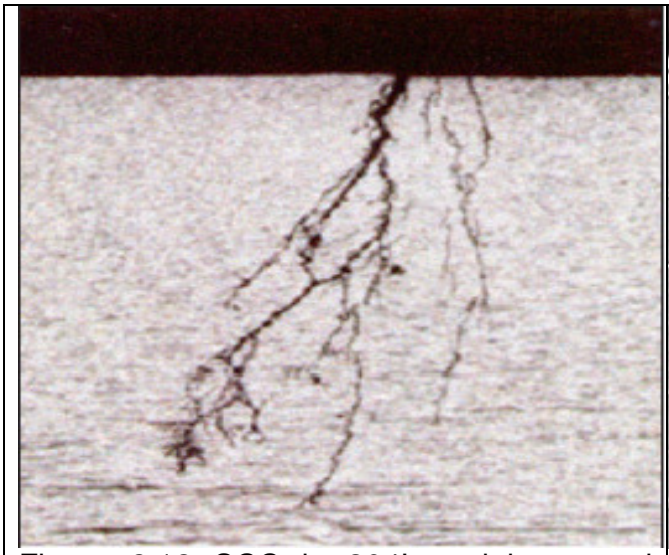

Figure 2.12 SCC in 304L stainless steel pipeline [27]

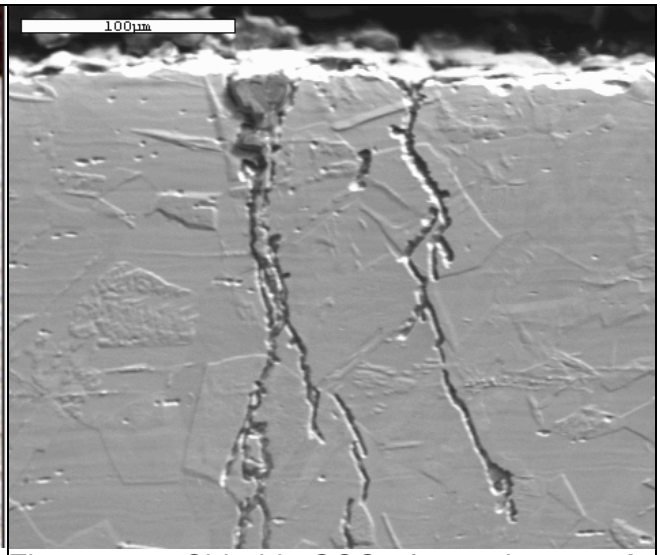

Figure 2.13 Chloride SCC of sample test 3A top (this work)

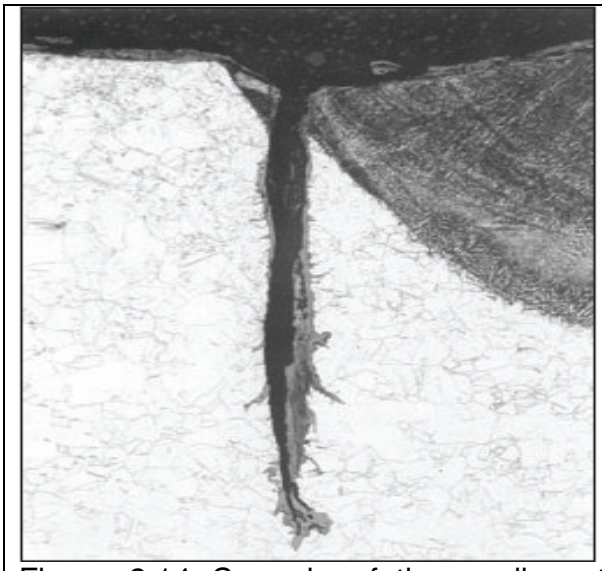

Figure 2.14 Corrosion fatigue adjacent to weld in 316 stainless steel pipeline [27]

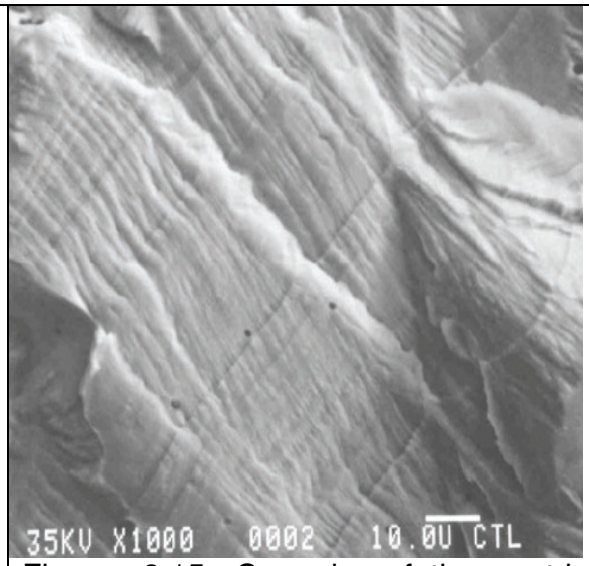

Figure 2.15 Corrosion fatigue striation (scanning electron micrograph) [27]

2.3 Preventing and controlling Stress corrosion cracking

SCC can be managed or controlled by repairing the material, changing the environment or reducing tensile stress, or can be prevented by changing the material (using resistant material).

2.3.1 Changing Environmental conditions

Possible environmental changes included the following:

- Raising the pH of the solution will reduce the probability of stress corrosion cracking.
- Designing to minimise crevices and localised deposits
- Reducing the chloride concentration.
- Cathodic protection (making the potential less positive than the presumed stress corrosion cracking threshold)

2.3.2 Reducing Stress

Several methods had been practised to reduce the stress. These include proper welding methods, reduction of the residual stresses by stress relieving the formed or welded material, and shot peening the component (resulting in compressive stresses on the surface).

2.3.3 Material choice

High-nickel alloys and duplex stainless steels (such as 2205) can be used, but are more expensive. For some applications, ferritic stainless could be used and offers lower cost. In low chloride environments type 316 stainless steel would more suitable because it has better pitting corrosion resistance than 304 stainless steel.

2.3.4 Repairing defects

Weld repair of defects is recommended if changing the environmental conditions is difficult, residual stress are lower due to geometry, manufacturing and construction and replacement of the material is not possible [1]. Methods such as laser and tungsten inert gas welding have been trialled on pipes and tanks [1, 4]. However, welding may itself introduce new defects. A summary of welding defects and corrosion phenomena resulting from these defects is shown in figure 2.16. Such defects can compromise the integrity and the quality of weld repairs.

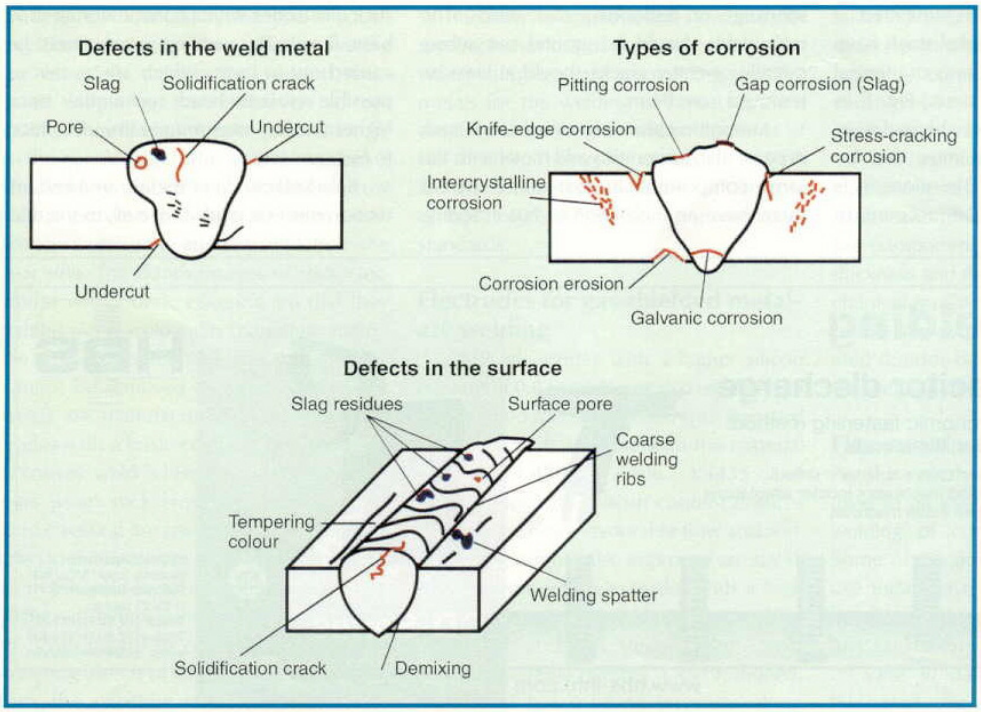

Figure 2.16 welding defects and corrosion phenomena resulting from these defects [28].

2.3.5 Laser welding

As mentioned, this research is part of larger project which aims to repair the stress corrosion cracks in-service. For this reason, the repair process is mentioned briefly.

Laser welding is well established in the fields of repair and surface protection [29]. Laser welding is a fusion welding process where any weldable material is joined using a laser beam as a high energy-density power source. Laser cladding involves the deposition of the material from powder or rod filler onto a substrate using laser heating. The process can be used as a repair procedure to rebuild wall thickness. Wear prevention by hard-surfacing the components and improved corrosion resistance can be obtained [30, 31].

With laser welding or cladding it is possible to control the depth of penetration to a greater extent, compared with Tungsten Inert Gas and Metal Inert Gas welding processes. Welding at high speed and at low heat input rates are possible, depending on the power of the equipment used. Advantages of laser welding are listed in Table 2.3. A typical nozzle typical arrangement is shown in figures 2.17. and 2.18 As schematic picture of the nozzle during the cladding process is shown by figure 2.18.

Table 2.5 Comparison of laser welding with conventional welding processes [32]

	Laser	**Electron Beam**	**Resistance Spot**	**Gas Tungsten Arc**	**Friction**	**Capacitive Discharge**
Weld Quality	Excellent	Excellent	Fair	Good	Good	Excellent
Weld Speed	High	High	Moderate	Moderate	Moderate	Very High
Heat Input Into Welded Part	Low	Low	Moderate	Very High	Moderate	Low
Weld Joint Fit-Up Requirements	High	High	Low	Low	Moderate	High
Weld Penetration	High	High	Low	Moderate	High	Low
Range of Dissimilar Materials	Wide	Wide	Narrow	Narrow	Wide	Wide
Range of Part Geometries/Sizes	Wide	Moderate	Wide	Wide	Narrow	Narrow

	Laser	Electron Beam	Resistance Spot	Gas Tungsten Arc	Friction	Capacitive Discharge
Controllability	Very Good	Good	Fair	Fair	Moderate	Moderate
Ease of Automation	Excellent	Moderate	Excellent	Fair	Good	Good
Initial Costs	High	High	Low	Low	Moderate	High
Operating / Maintenance Costs	Moderate	High	Moderate	Low	Low	Moderate
Tooling Costs	High	Very High	Moderate	Moderate	Low	Very High

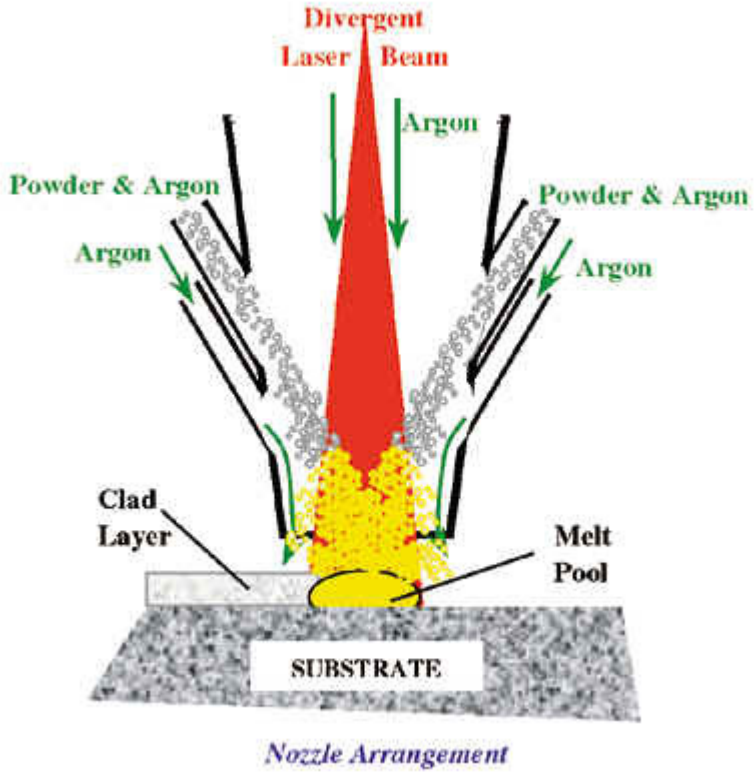

Figure 2.17 Nozzle arrangement for laser cladding [33]

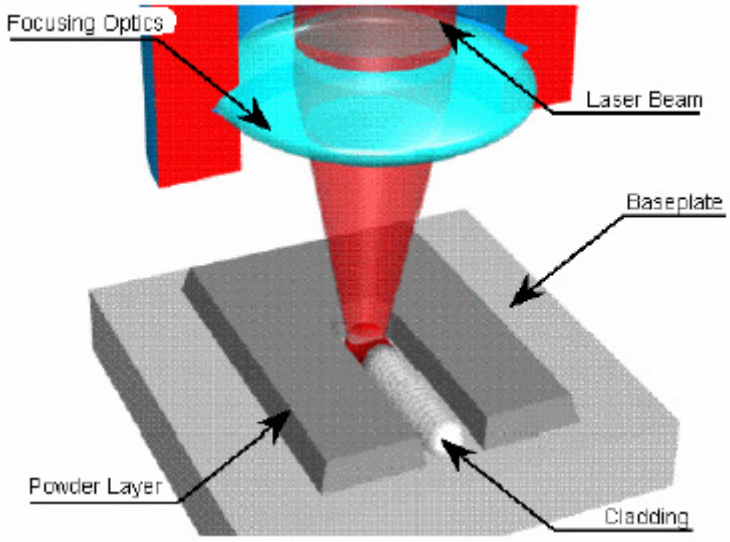

Figure 2.18 Single cladding process [34]

Chapter Three

3.1 Hypothesis

This work tested the hypothesis that (1) small amplitude loads when superimposed on sustained or constant load result in stress corrosion cracking at lower loads and (2) that thermally induced stress, together with residual stress from manufacturing and fabrication will reach the threshold stress required to crack the sample in a small laboratory rig.

3.2 Scope of research

The experimental work investigated stress corrosion cracking of non-standard samples, with cyclical loading superimposed on a baseline stress. The effects of cyclical strain, thermal stress and temperature on the time to failure were assessed, and the fracture surface and crack morphology were examined.

Chapter Four

4 Experimental design and methodology

4.1 Introduction

The designed rig (see figure 4.1) was constructed from tubes of type 304L stainless steel (samples to be cracked) and type 310 stainless steel plates and hollow bar (stressing elements). A heating element was inserted in the hole in the central type 310 bar. The resulting temperature difference between the bar and tube caused thermal stress (tensile in the 304L tube, and compressive in the type 310 bar). The inner surface of the 304L tube was exposed to magnesium chloride solution and the outside exposed to atmosphere. In the presence of tensile stress and magnesium chloride solution, at temperatures above 60℃, Type 304L stainless steel is expected to crack. Type 310 stainless steel has superior stress corrosion cracking resistance. Filler metal ER309L Si is suitable for dissimilar welding and was used here to fabricate the rig.

Chemical analysis and mechanical testing of Type 304L stainless steel were performed. Strain gauges mounted on the tube were used to measure the strain and thermocouples were used to measure temperature (both types of measurement were recorded with a data logger). Following testing, crack depths and crack density were measured, and cross-sectional samples were examined metallographically. Fracture surface analysis was performed on some selected fracture surfaces. The success of the study to produce cracked samples will be followed by a Laser cladding or welding repaired.

4.2 Sample design (rig design) and testing conditions

Rig Design

The test rig was designed to simulate a vessel, pipe or tank that has undergone stress corrosion cracking and needs repair. The temperature difference between the hollow bar and 304L stainless steel tube induced thermal stress in the 304L

tube, superimposed on residual stresses from manufacturing and fabrication. The cracks were expected to initiate from the inside of the 304L tube.

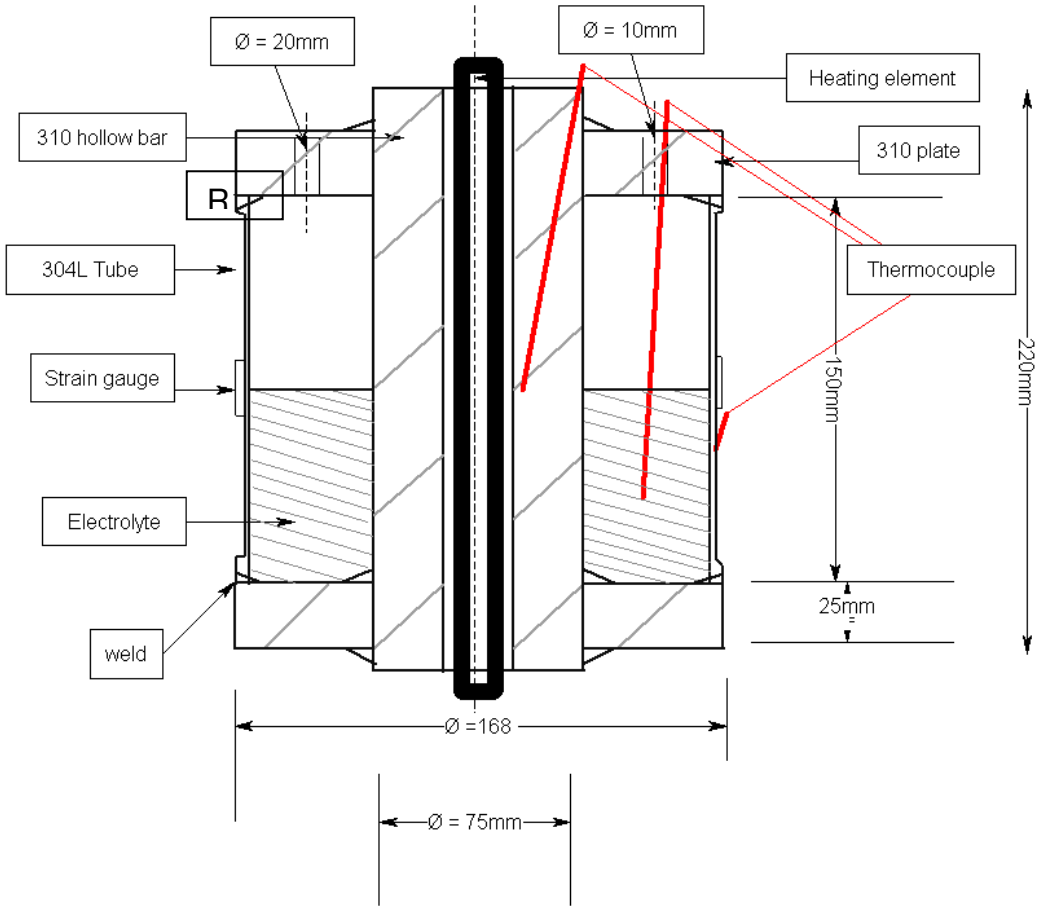

Figure 4.1 Schematic illustration of test rig. "R" shows the top weld.

A successful outcome with the designed rig was defined as failure of only the 304L tube, with the hollow bar carrying the (compressive) load without failing. The dimension and sizes selected have to be according to load carry capacity. To test whether the dimensions selected are suitable, design calculations (see appendix A) for load carrying capabilities/limits were performed, to show that the center bar and outer tube will be able to carry the load according to experimental requirements and that the sizes are suitable in terms of diameters and wall thickness.

Electrical circuit: Heating element

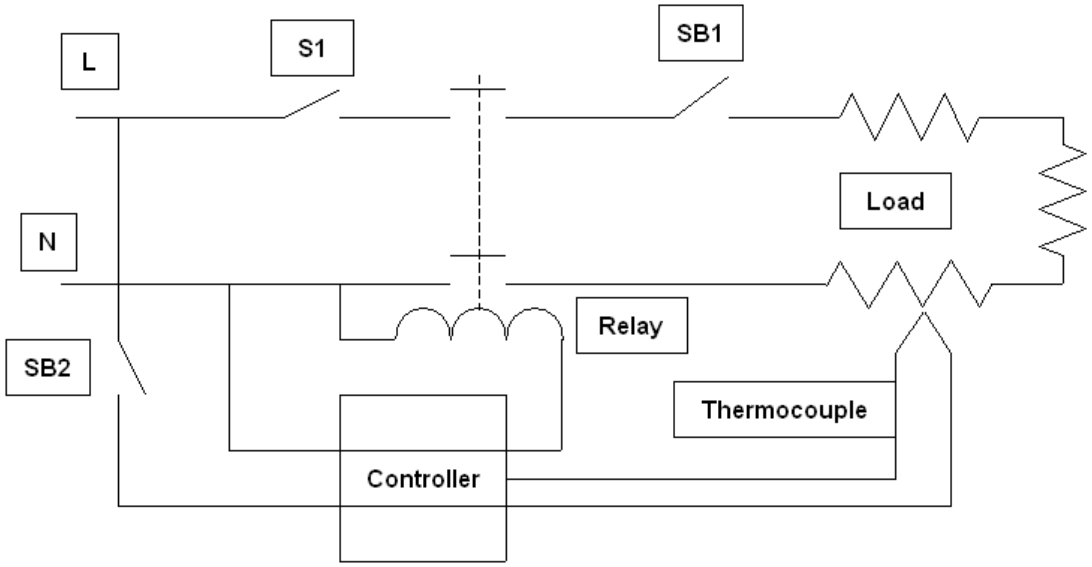

Figure 4.2 Schematic electric circuit of the heating element with single temperature controller

The electrical circuit with heating element and controller is shown in figure 4.2. One of two controllers could be selected, where one had a large (0 to 800ºC) temperature range and the other had a smaller (0 to 200ºC) temperature range. Circuit breaker no.1 (SB1) was for the heating elements and circuit breaker no.2 (SB2) was for the controller.

Test Conditions

Type J thermocouples were used to measure temperature. The environment was magnesium chloride solution. $MgCl_2$ solutions are more aggressive (with respect to chloride cracking of stainless steels) than other aqueous chloride solutions due to the slight acidity of the solutions (*p*H = 6). The stress sources were residual stress and thermally induced stress. Type 304L stainless steel material was selected, with temperature and solution concentration selected to crack 304L. Figures 4.3 and 4.4 show the temperature and solution concentration ranges relative to regions of susceptibility to stress corrosion cracking.

Chloride concentrations were $1.6X10^5$ ppm chloride (21% $MgCl_2$ solution) and $2.6X10^5$ ppm chloride (35% $MgCl_2$ solution), with average temperatures of 80℃

and 92 ℃ and pH of between 1.1 to 6. Distilled water and hydrochloric acid were used to adjust or maintain the pH during the tests. The solutions were prepared by dissolving $MgCl_2.6H_2O$ (analytical grade) in demineralized water. The solution was left open to atmosphere (in the test rig) to allow the presence of dissolved oxygen. Initially the replenishment was performed using $MgCl_2$ solution (tests 1 and 2) and demineralised water was used subsequently.

The solution *pH* was measured during the tests. To measure *pH*, a solution sample was removed from test rig, cooled down, and then measured at room temperature.

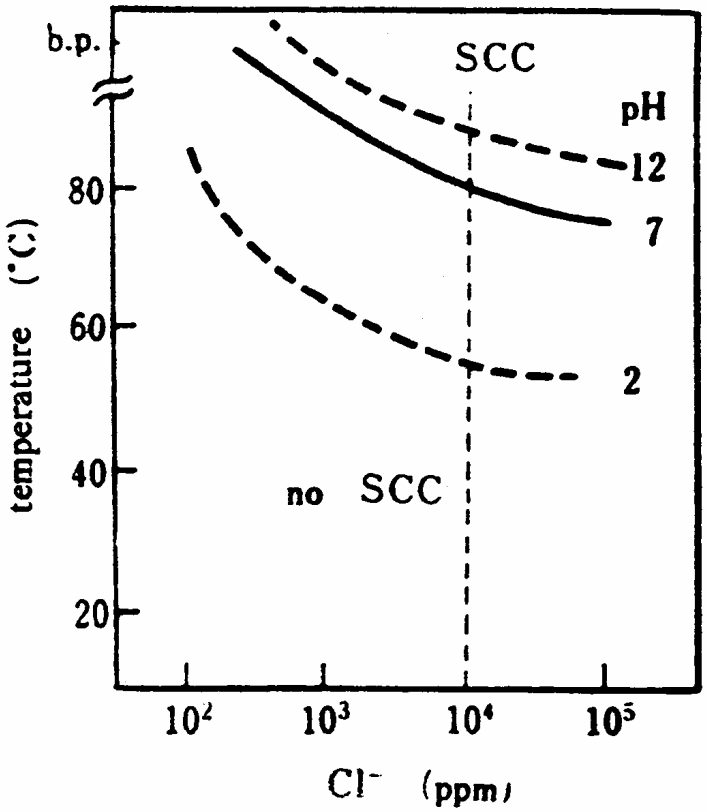

Figure 4.3 The relationship between temperatures and chloride concentrations which lead to stress corrosion cracking of 304 [2]

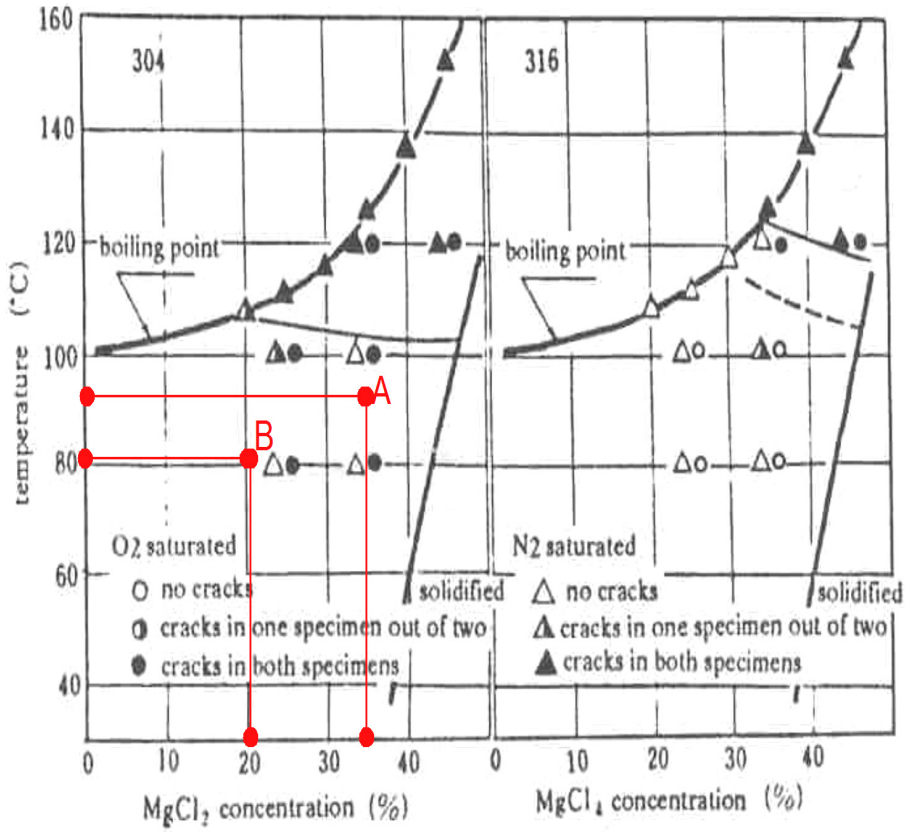

Figure 4.4 The relationship between temperature, chloride concentration and cracking, showing boiling point and solidification of $MgCl_2$ solution [2]

Some samples were grooved by a sharp-tipped machining tool. The sharp tip was used to shave material at localized point to produce a 0.5mm wide and 0.5mm deep triangular groove all around the internal circumference, at the mid point of the sample. The groove served to increase the local stress. The grooved samples are indicated in the test conditions summary as given in Table 4.1.

Table 4.1 Test conditions summary

	Test 1	**Test 2-5**
$MgCl_2$ concentration in solution	21wt%	35wt%
Mass of Cl^- in 100g solution	15.64g	26.06g
Temperature of hollow bar	80°C	90°C, 101°C, 114°C, 127°C
Temperature of the solution	79.96°C	80°C, 83°C, 86°C, 91°C
Tests with bar diameter of 75mm	None	T3A, T3B, T3C, T4A, T4B, T4C, T4D, T5A
Tests with bar diameter of 50mm	T1A, T2A, T2B	T5B, T5C
Grooved samples	None	T4C, T4D, T5B, T5C

The stress intensity at the notch is estimated to be about 4 MPa.m$^{0.5}$, assuming an average stress of 100MPa and a crack of 0.5mm.

4.3 Measurement of strain

Strain gauges were used to measure the elastic strain of the tube test sample. HBM type strain gauges with temperature compensation for steel (α= 10.8X10^{-6}/ºC) suitable for steel of accuracy of about 0.3µm/m were used, with resistance of 120Ω and gauge factor of 2. Full and half Wheatstone bridges were used (full bridge for samples T3A, T3B, T4A, T4B, T4C, T5A, T5B and T5C and half bridge for T3C), see figures 4.5 and 4.6.

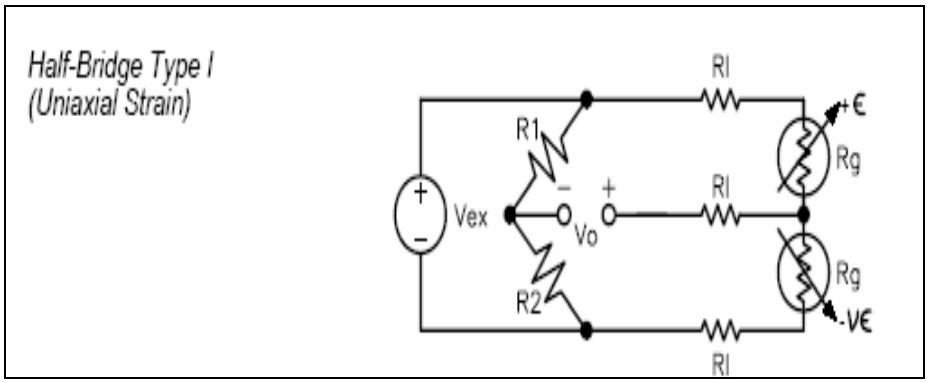

Figure 4.5 Schematic: half Wheatstone bridge [35].

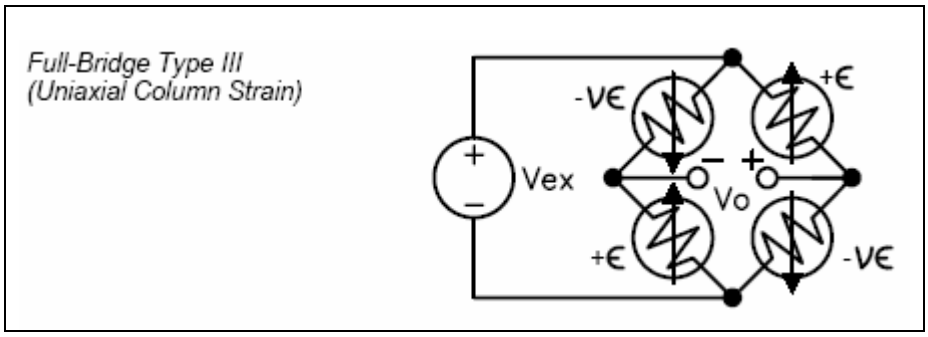

Figure 4.6 Schematic: full Wheatstone bridge [35]

Typical test results of temperature and strain are plotted below in Figures 4.7 and 4.8 respectively. The temperatures measured at the center bar, in the solution and on the outside surface of the sample (as shown in figure 4.1) are plotted in figure 4.7, showing that the temperature differed between these areas and varied over time during testing. The measured strain follows the pattern of temperature variations (see figure 4.8). The oscillations in temperature and strain resulted

from the on-off nature of the controller. Figure 4.9 shows the temperature difference (temperature of the bar minus temperature of tube sample) with time. The significance of this difference is that it is the origin of the thermal stress which was imposed on the tube sample by the bar.

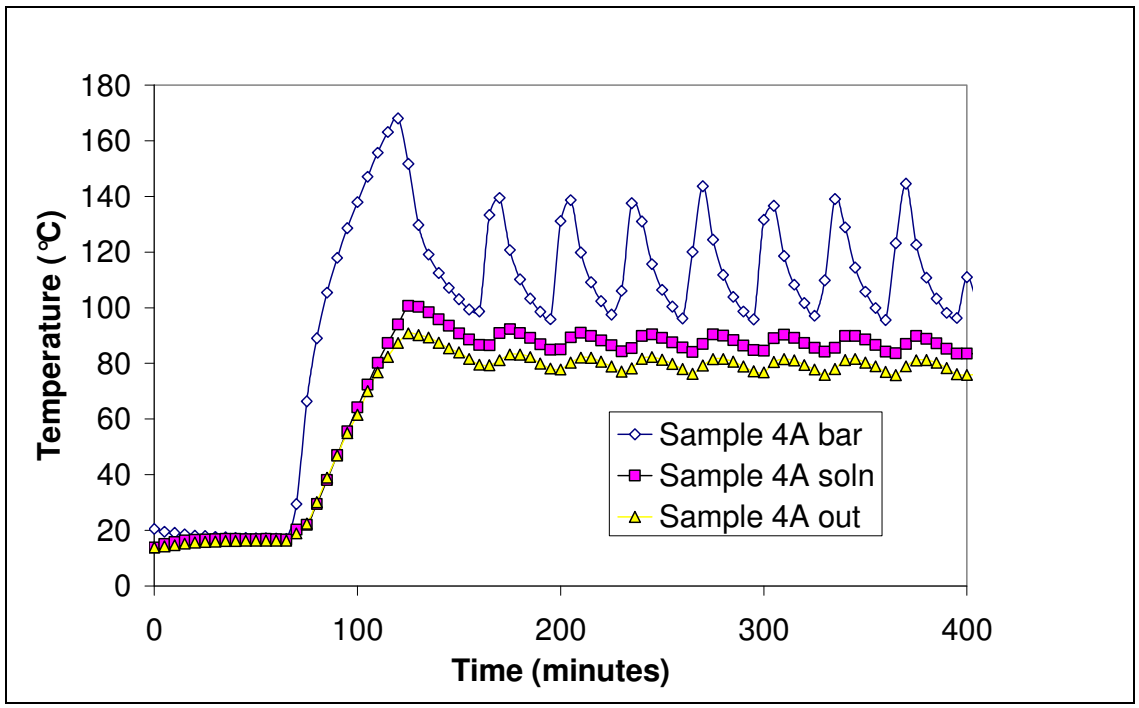

Figure 4.7 Typical temperature results from the experiment (sample 4A shown)

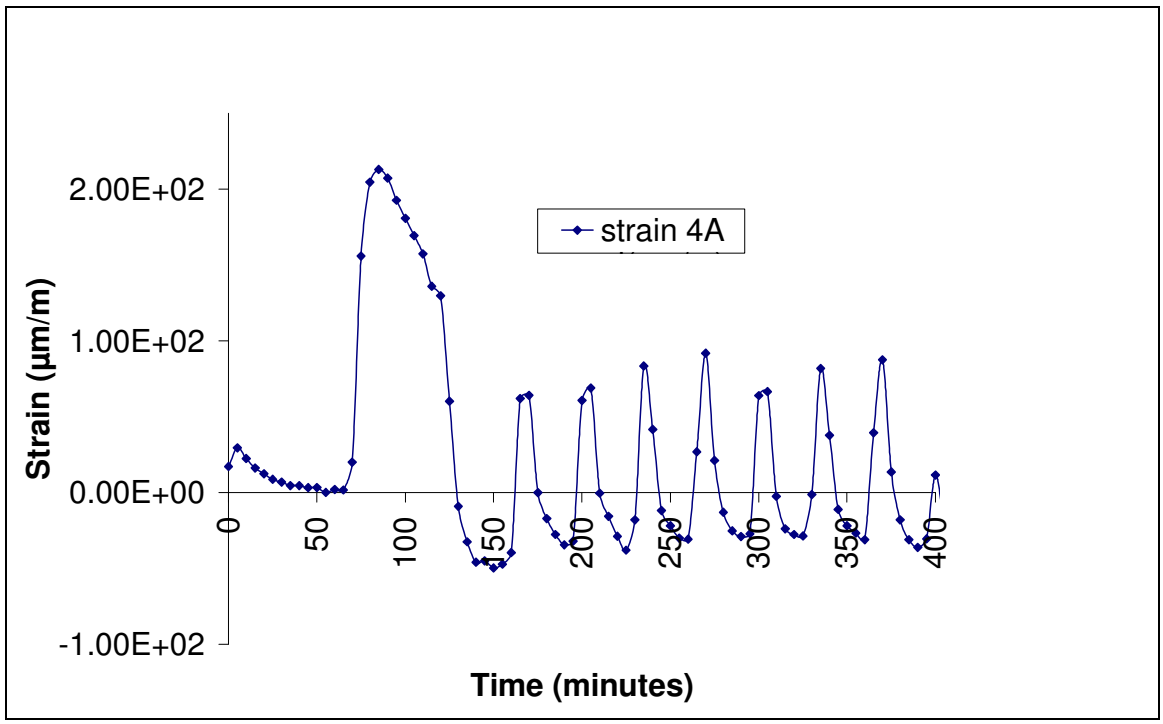

Figure 4.8 Typical strain results from the experiment (sample 4A shown)

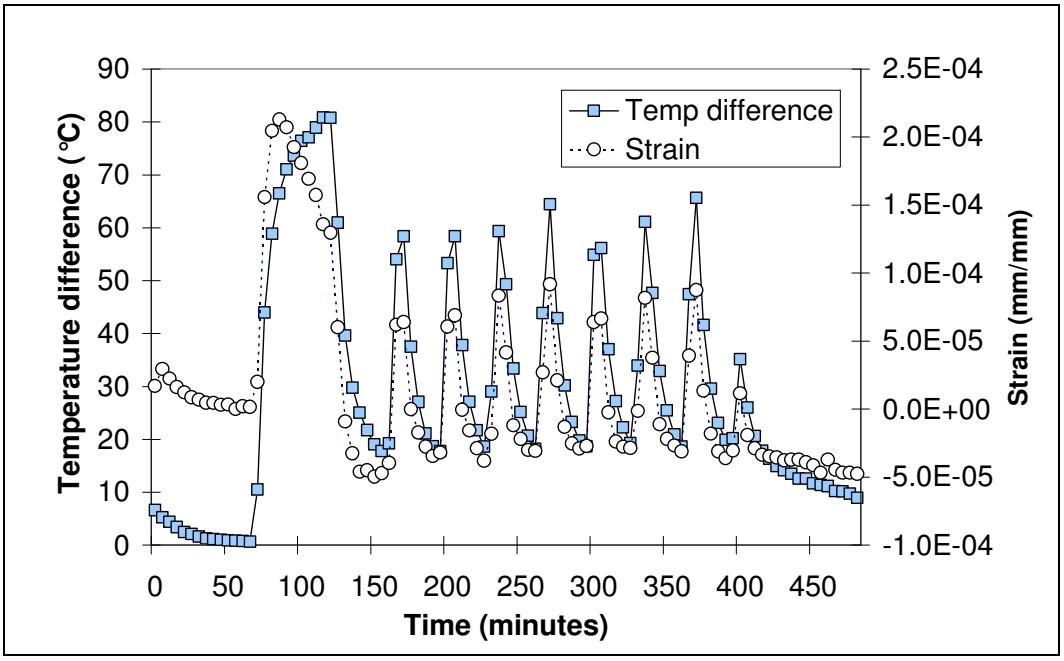

Figure 4.9 Typical temperature difference (bar-sample) and strain variation with time in sample 4A

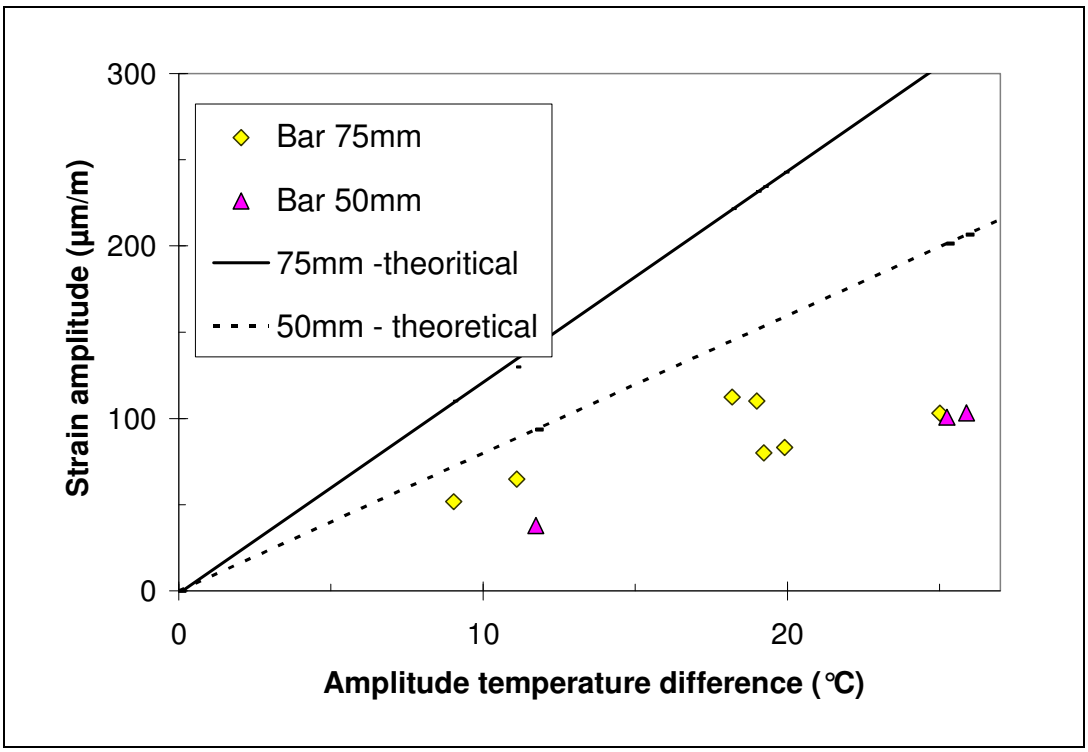

Figure 4.10 Theoretical and actual strain amplitude plotted against amplitude of the bar-sample temperature difference amplitude. Notes on legend: "Bar 50mm theoretical" and "Bar 75mm theoretical" – strain amplitude **predicted** from temperature difference, for samples with Ø50mm and Ø 75mm center bars respectively; "Bar 50mm ave strain" and "Bar 75mm ave strain" – **measured** strain amplitude for Ø 50mm and Ø 75mm center bars respectively.

The strain in the tube (sample) is caused by the temperature difference between the bar and the tube. A simple analytical method can be used to obtain a first estimate of the elastic stress in the tube (sample), as shown below. Comparison of the actual cyclical elastic strain with the predicted values (Figure 4.10) shows the actual values to be approximately half the predicted values. The main reason for this is likely to be flexing of the type 310 flange which connected the bar to the sample; flexing of this flange hence took up some of the thermal strain, resulting in less stressing of the sample. If the flange were rigid, the expected relationship between the bar-sample temperature difference and the stress in the sample is as follows:

$$\sigma/E = \alpha\,\Delta T/(1 + A_2/A_1) \qquad (1)$$

In equation 1, σ is the stress in the tube sample, E is the elastic modulus α is the thermal expansion coefficient, ΔT is the temperature difference between the bar and tube, A_2 is the cross-sectional area of the tube, and A_1 is the cross-sectional area of the bar

This relationship is derived from simple balance of forces, as follows:

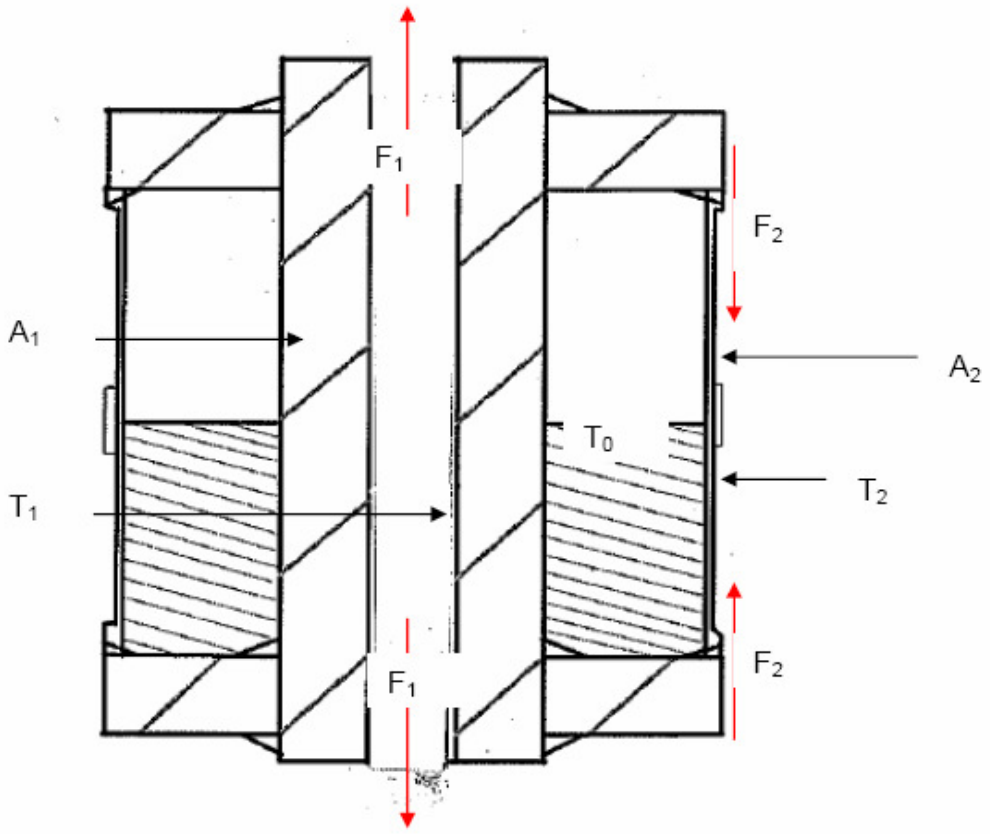

Figure 4.11 Forces acting in the test rig

Let σ_1 be the (compressive) stress in the bar, and σ_2 the (tensile) stress in the tube. Then $\sigma_1 A_1 = -\sigma_2 A_2$, or $\sigma_1 = -\sigma_2 A_2/A_1$

If the end flanges are rigid, then the total strain (elastic and thermal) of the tube and bar must be equal. If T_x is the initial temperature at which the stresses in the tube and bar are zero, the strains can be written as:

$\varepsilon_1 = \sigma_1/E + \alpha(T_1-T_x) = \varepsilon_2 = \sigma_2/E + \alpha(T_2-T_x)$
Substitution of the expression $\sigma_1 = -\sigma_2 A_2/A_1$ then yields
$\sigma_2/E = \alpha(T_1-T_2)/(1+A_2/A_1)$

4.3.1 Predicted Strain and Temperature: finite-element analysis

Finite-element analysis was performed on the test rig to obtain more accurate predictions of the steady-state temperatures and stresses. The analysis was performed by a specialist in structural integrity at Eskom, Mr Ronnie Scheepers.

The following material properties for 304L stainless steel were used for the temperature distribution and thermal stress calculations:

Table 4.2 Physical properties

Thermal conductivity of stainless steel	15 W/mK
Modulus of elasticity	193 GPa
Poisson's ratio	0.24
Thermal expansion coefficient	16.9×10^{-6} °C^{-1}

It was assumed that the central surface temperature (on the inner surface of cylindrical cavity in the bar, next to the heating element) is at 110ºC. Natural convection between the outer surface and surrounding air (at 20°C) was assumed (see figures 4.12 and 4.13). The assumed convection heat transfer coefficient was 5W/m^2°C (table 4.3). Within the sample rig, the thermal conductivity of steam (at 100°C) was used in the freeboard, and that of water (at 93°C) for the solution (table 4.3). Results are presented in figures 4.11 to 4.14.

Table 4.3 Heat transfer constants used

Conductivity of steam top (100℃)	0.0243W/m℃
Conductivity of liquid water (93℃)	0.678W/m℃
Heat flow (interior of bar surface)	0.01 W/mm^2
Convection heat transfer coefficient- top	5W/m^2 ℃
Convection heat transfer coefficient- centre	5W/m^2 ℃
Convection heat transfer coefficient- bottom	5W/m^2 ℃

The calculated thermal stress at the internal surface of the tube was approximately 26 MPa for the 75 mm centre bar, and 22MPa for the 50 mm centre bar (see figures 4.14 and 4.15). The predicted temperatures are comparable with the measured temperatures (as presented later).

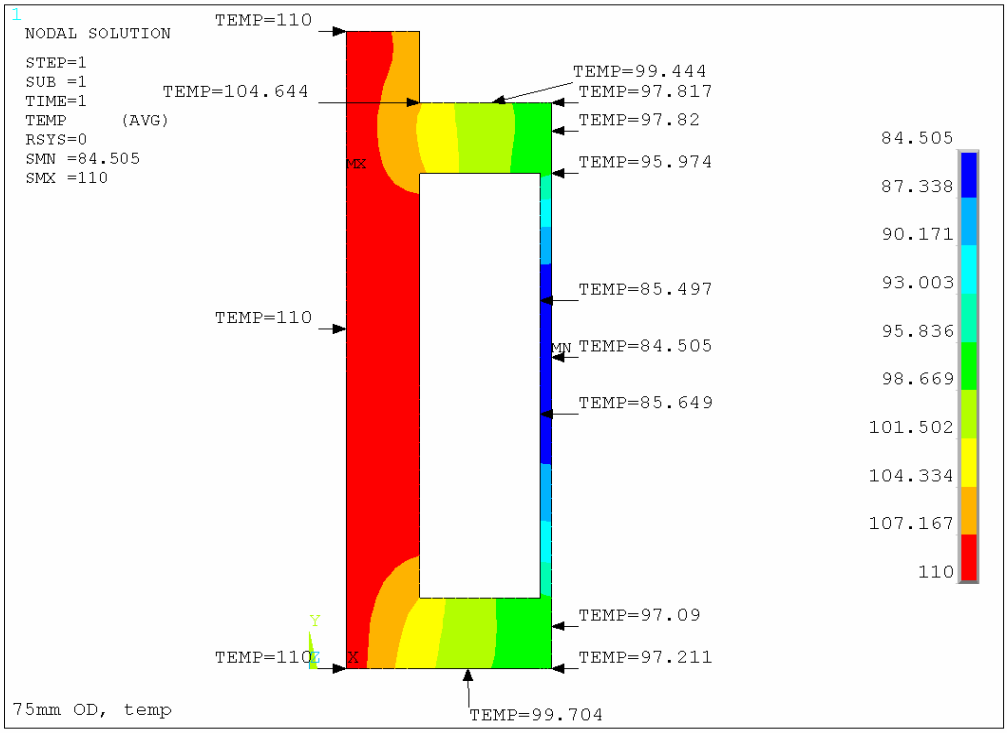

Figure 4.12. Steady state temperature distribution for rig with a Ø75mm centre bar.

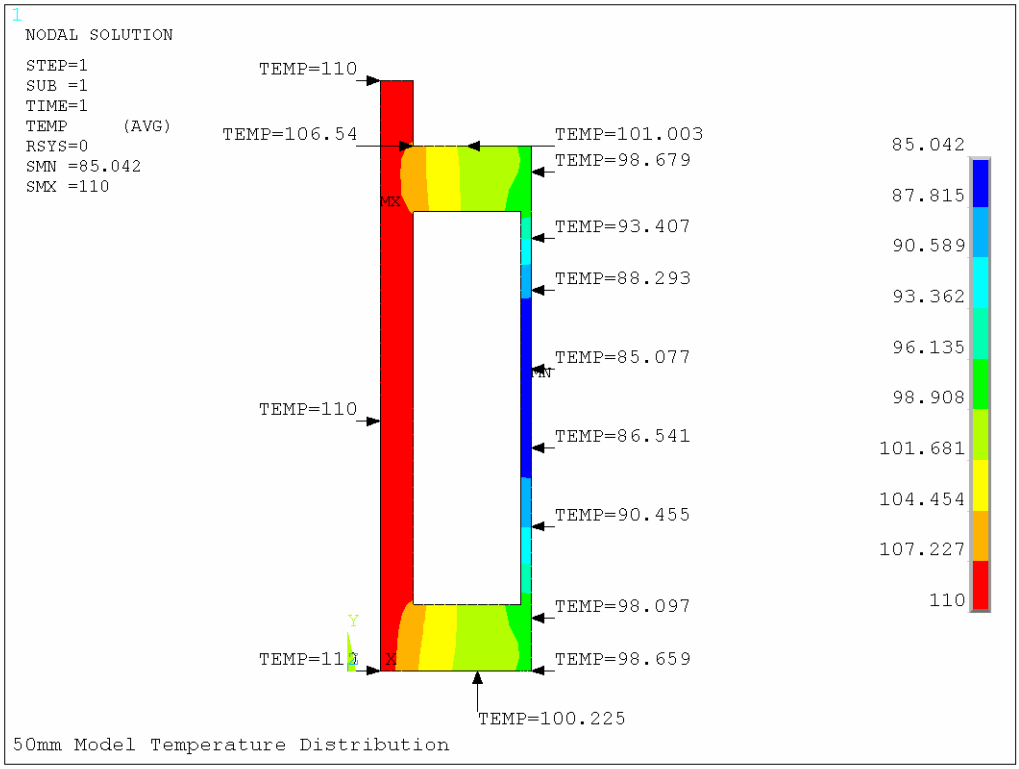

Figure 4.13. Steady state temperature distribution for rig with a Ø50mm centre bar.

Figure 4.14. Steady state stress distribution for a rig with a 75mm diameter centre bar.

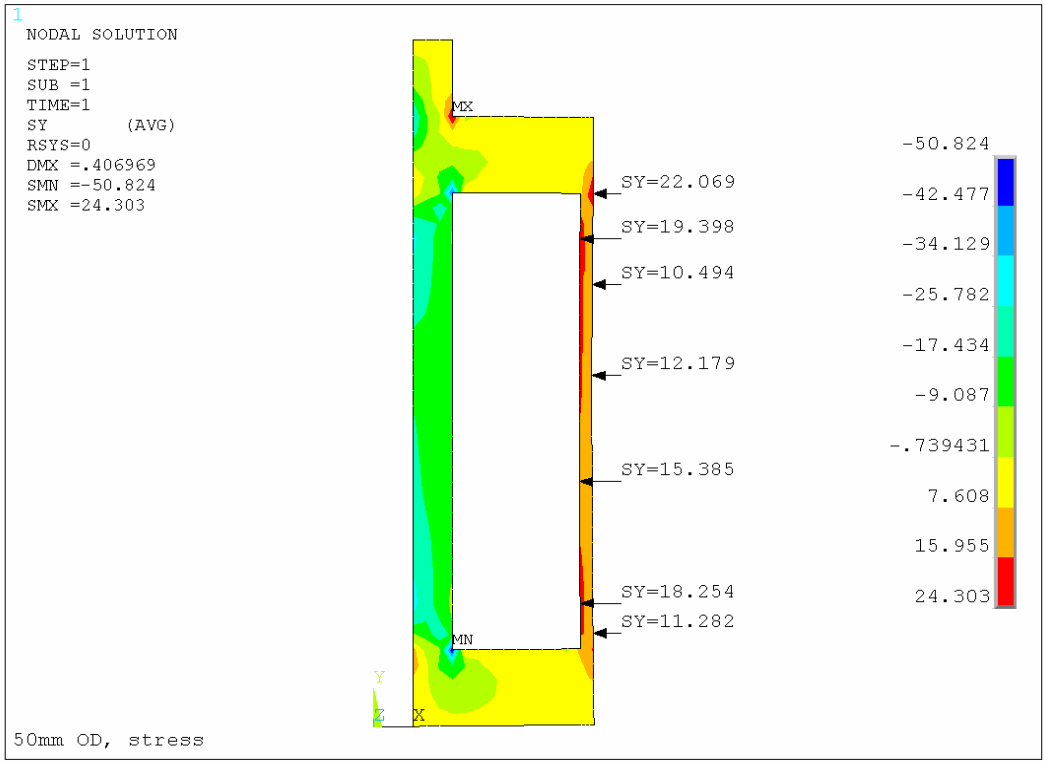

Figure 4.15. Steady state stress distribution for a rig with a 50mm diameter centre bar.

4.4 Mechanical Testing

The tensile properties and hardness of the tube were measured. Mechanical testing was performed according to ASTM standard 307 for flat samples. Vickers hardness tests were performed. The mechanical test results are within specification (DIN X2CrNi 18-9 or EN 10088 no 1.4307) for as-received stainless steel. The average hardness is 85HRB. The ultimate tensile strength was 668MPa and the 0.2% proof strength was 340MPa. The as-received grain size was 40 micron.

4.5 Visual examination and metallography

After testing, samples were examined by scanning electron microscope, stereo and optical microscope to identify the mode of failure, microstructure, and crack density.

The samples were examined visually to detect gross defects (e.g. leakage of solution during the test, indicating a through-wall crack). The evidence was

recorded and photographed. Stereo microscopy supported visual examination. Visual examinations and stereo microscope analysis of cracked or failed samples were performed on external and internal surfaces, and observations recorded. The bar and flange were also examined for cracks and noted. The cracks were classified as being through-wall or non-through-wall and surface cracks were counted. Cross-sectional evaluations of cracks were performed at selected positions, measuring crack depths (see figures 4.16 and 4.17).

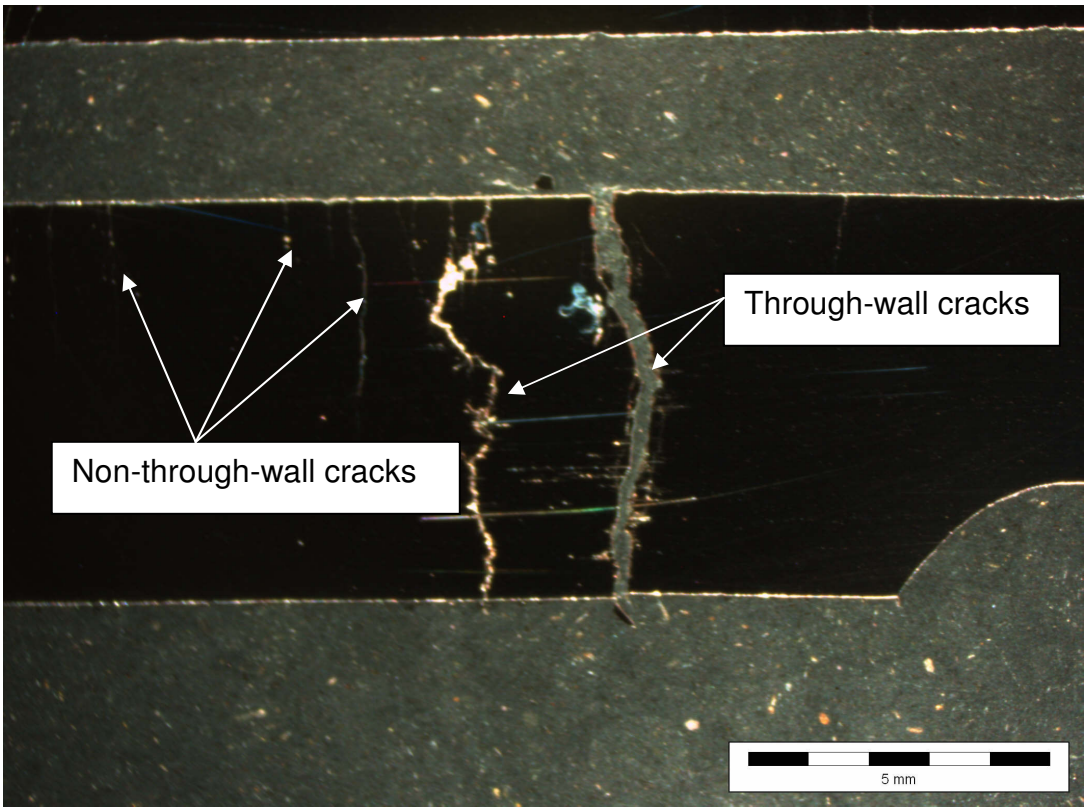

Figure 4.16 Typical stereo microscope image of type 304L stainless steel sample (cross-section) after testing

Metallographical evaluation was performed on polished cross-sections of the polished samples; cracks were counted and documented. The crack morphology was evaluated.

Scanning electron microscopy (SEM) was used for fracture analysis at higher magnification.

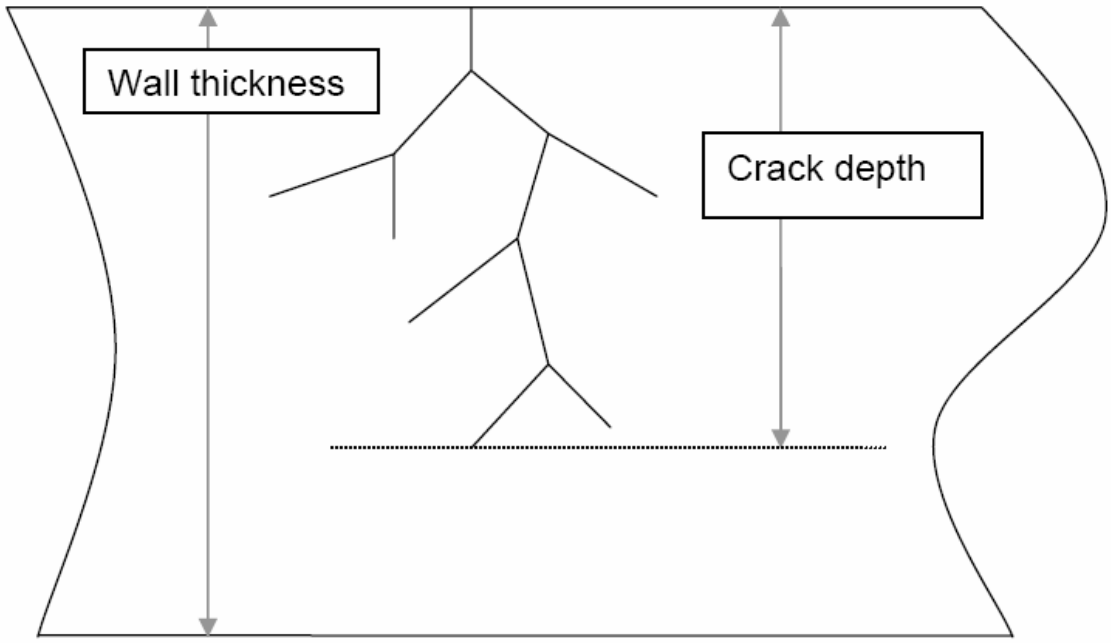

Figure 4.17 Measuring crack depth

Chapter Five
Analysis of conditions during tests

5.1 Introduction

The three main factors which were expected to influence crack formation and growth were sample temperature, stress, and variations in stress (amplitude and frequency). Because the sample was heated by convection and conduction from the central bar, and was also stressed by the temperature difference between the sample and the central bar, these factors could not be varied independently in the experiments. This chapter presents results on the conditions during the tests, to illustrate the range of experimental conditions. Analysis of the contribution of corrosion fatigue to cracking is also presented. Detailed analysis of crack appearance and crack density is presented in the next chapter.

5.2 Relationship between bar-sample temperature difference and stress in sample

The predicted relationship between the temperature difference between the heated central bar and the sample, and the thermal stress in the sample, was presented in section 4.3. This section gives results of measured temperatures and more detail of measured elastic strains.

5.2.1 Average temperatures

The temperatures within the test rig had two main features which could affect cracking of the sample: a difference between the average temperature of the (heated) central bar and the sample, and fluctuation in the bar-sample temperature difference. The temperature difference between the bar and the sample was responsible for the tensile thermal stress in the sample. The temperature difference arose because the bar was heated centrally with a resistance heater and the sample lost heat to the surroundings, mainly by convection. The fluctuations in temperature resulted from the on-off nature of the temperature controller which was used.

The finite-element calculations predicted a typical temperature difference between the bar and sample of 25°C. Measured temperatures are given in Figure 5.1, showing temperature differences of at least this much, and often greater.

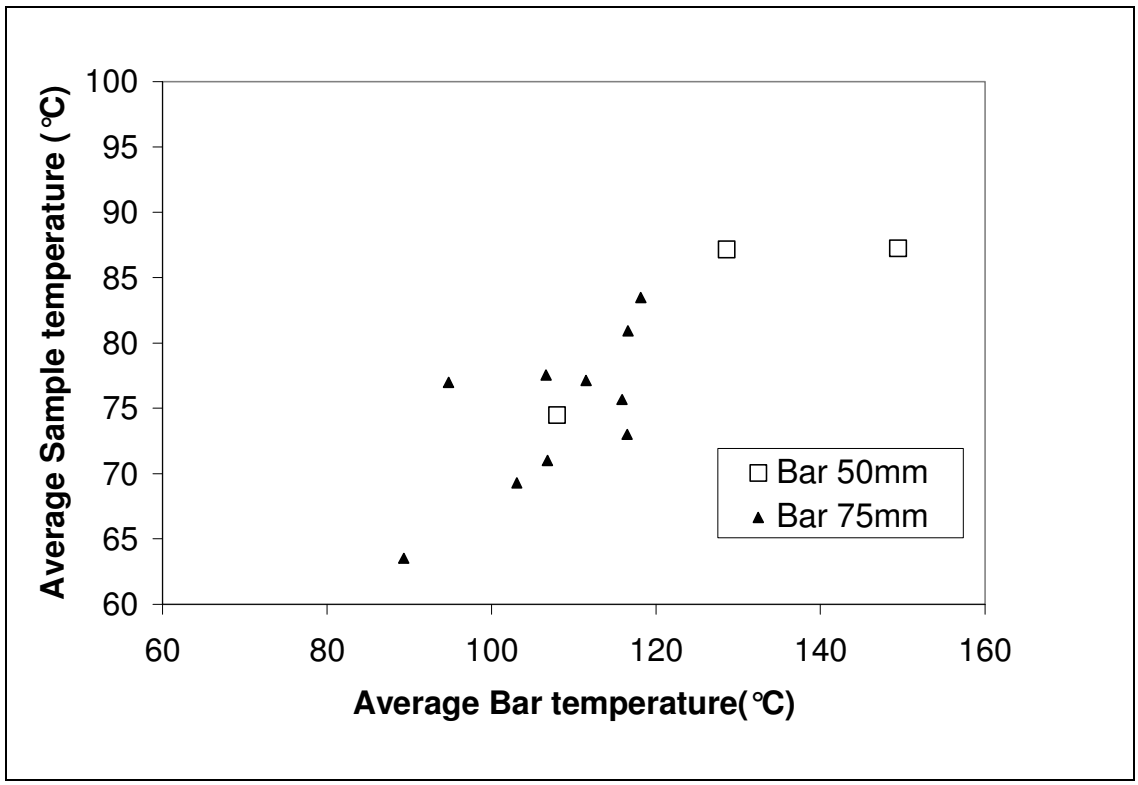

Figure 5.1 Measured average bar and sample temperatures for individual samples in tests 3, 4 and 5.

Thermal mapping confirmed that the sample temperature was fairly uniform, as predicted by the finite element calculations. Figure 5.2 shows the measured thermal maps. The thermal maps illustrate that the weld, heat affected zone, end flanges and the heating elements had temperatures above100ºC; in the other areas the temperature was between 50ºC and 90ºC. The difference in the appearance of the strain gauges in the thermal map is not because of a higher temperature, but rather a difference in emissivity.

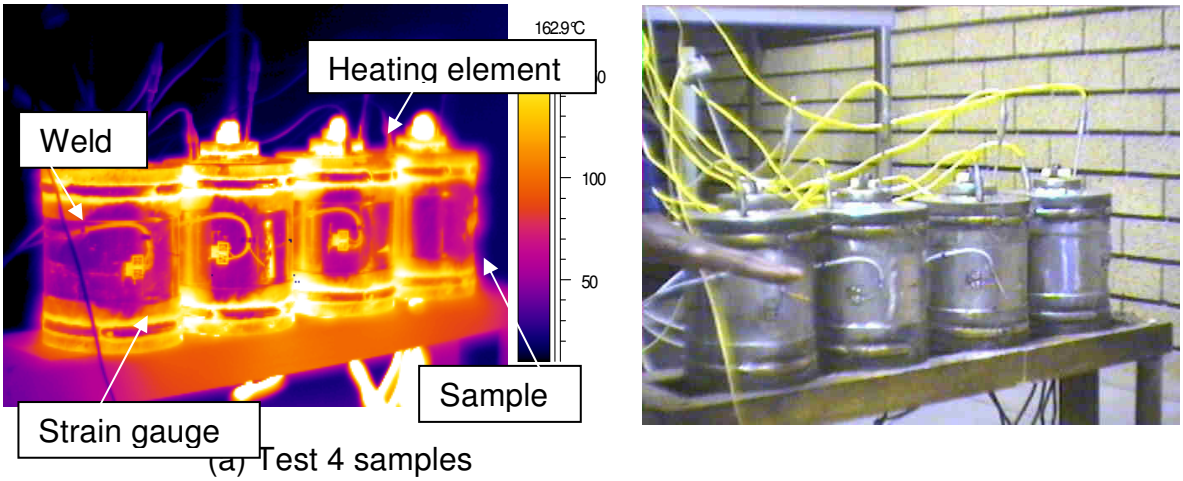

(a) Test 4 samples

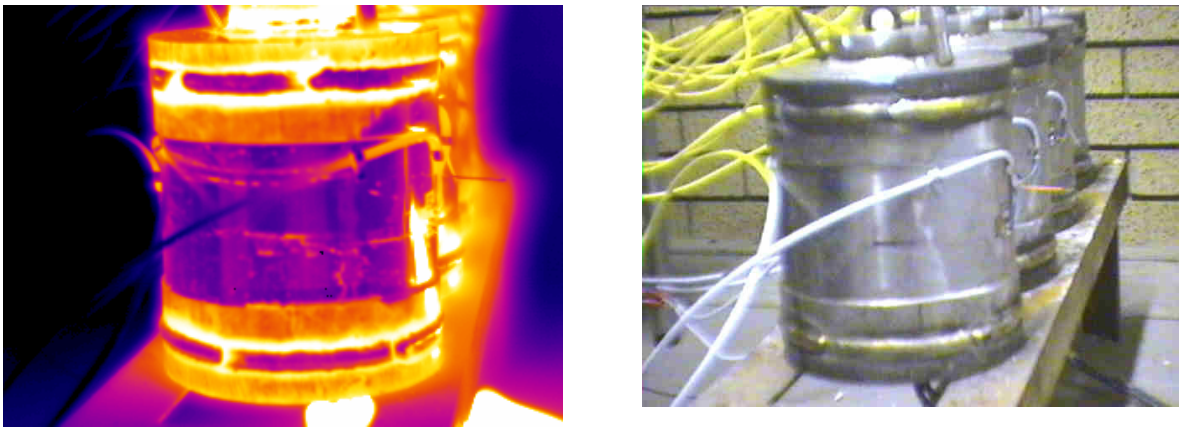

(b) Test 4 sample D

Figure 5.2 Thermal maps (left) and visible-light images (right) of samples during a test.

5.2.2 Average conditions during tests

The average sample temperatures during testing also contribute to the thermal stress. Figure 5.3 show the effect of average temperature on stress corrosion cracking. The average sample temperature was above 60°C in all cases. The $MgCl_2$ solution temperature was more than the sample temperature, by 8°C on average. In test 3 the samples were between 63°C and 70°C, in test 4 between 73°C and 80°C, and in test 5 between within 83°C and 87°C. Tests 6, 7 and 8 were shorter runs which were used to confirm/recheck data recorded (temperatures and strains; samples were not tested to failure in tests 6-8). Average sample temperatures are given below in Table 5.1.

Table 5.1 Summary of average sample temperatures during tests

Sample number	Bar outside diameter (mm)	Average sample temperature (ºC)
3A	75	63.5
3B	75	71.0
3C	75	69.3
4A	75	73.0
4B	75	80.9
4C	75	75.7
4D	75	77.1
5A	75	83.5
5B	50	87.2
5C	50	87.1
6A	75	77.6
7A	75	77.0
8A	50	74.5

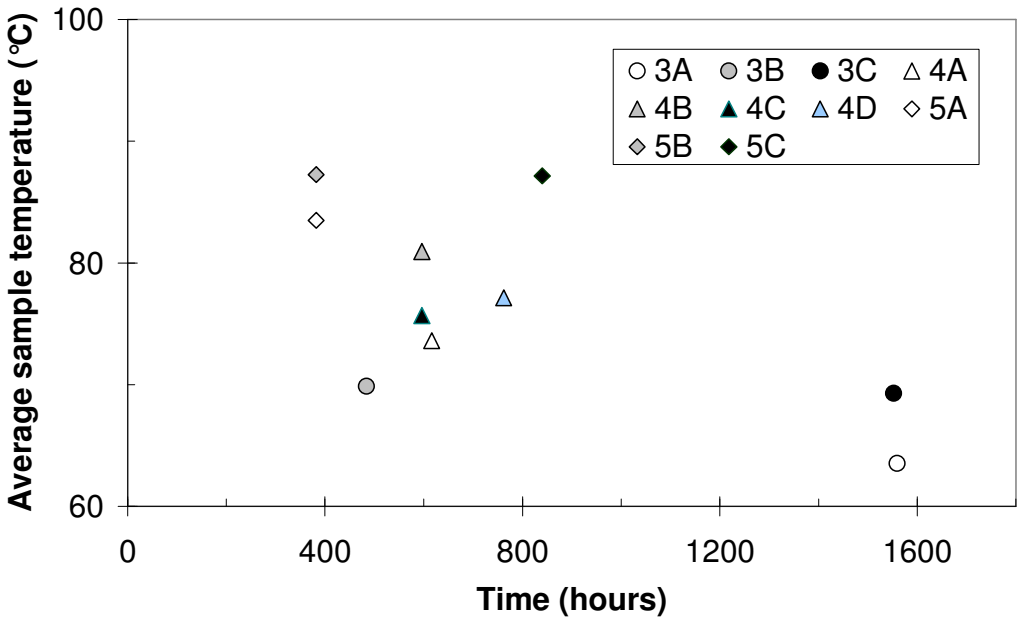

Figure 5.3 Influence of average temperature on time to failure

5.2.3 Temperature fluctuations

The temperature difference between the bar and sample followed an inverse sawtooth pattern, of rapid increases followed by slower decreases. The rapid increase in temperature difference occurred when the heating element was

turned on by the controller, with the slower decreases when the heating element was off. Examples are shown in Figure 5.4.

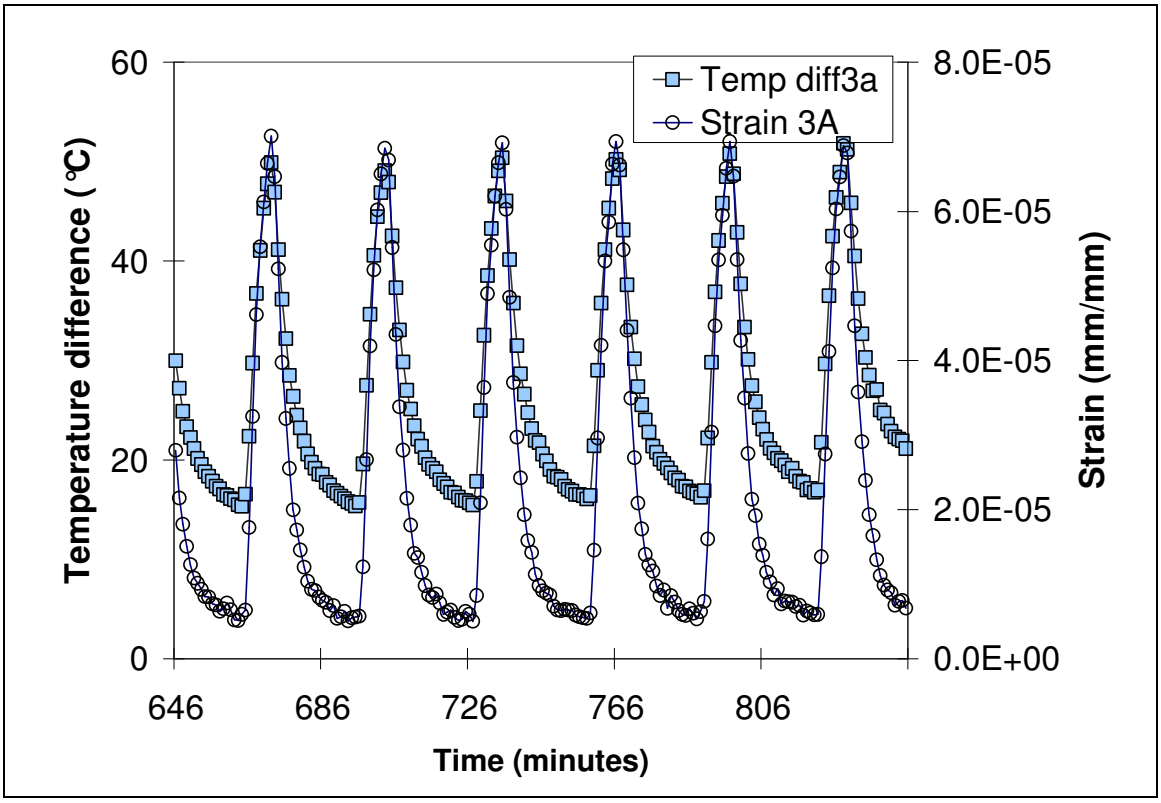

Fig. 5.4 (a) Test 3A

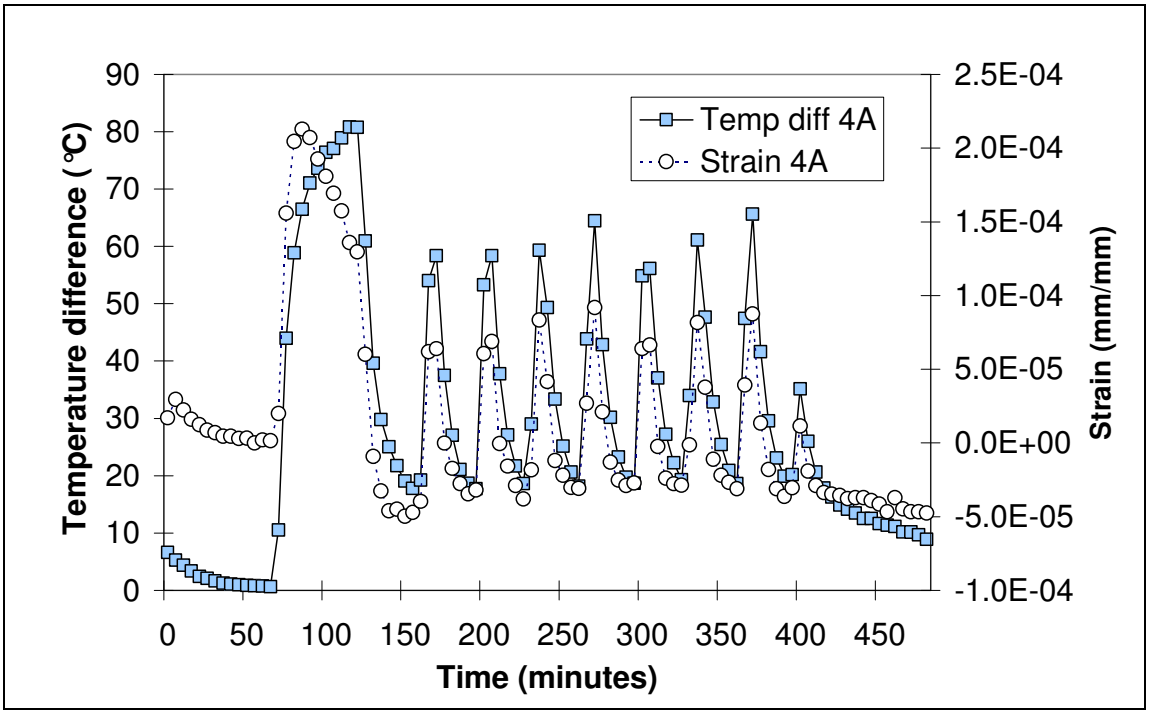

Fig. 5.4 (b) Test 4A

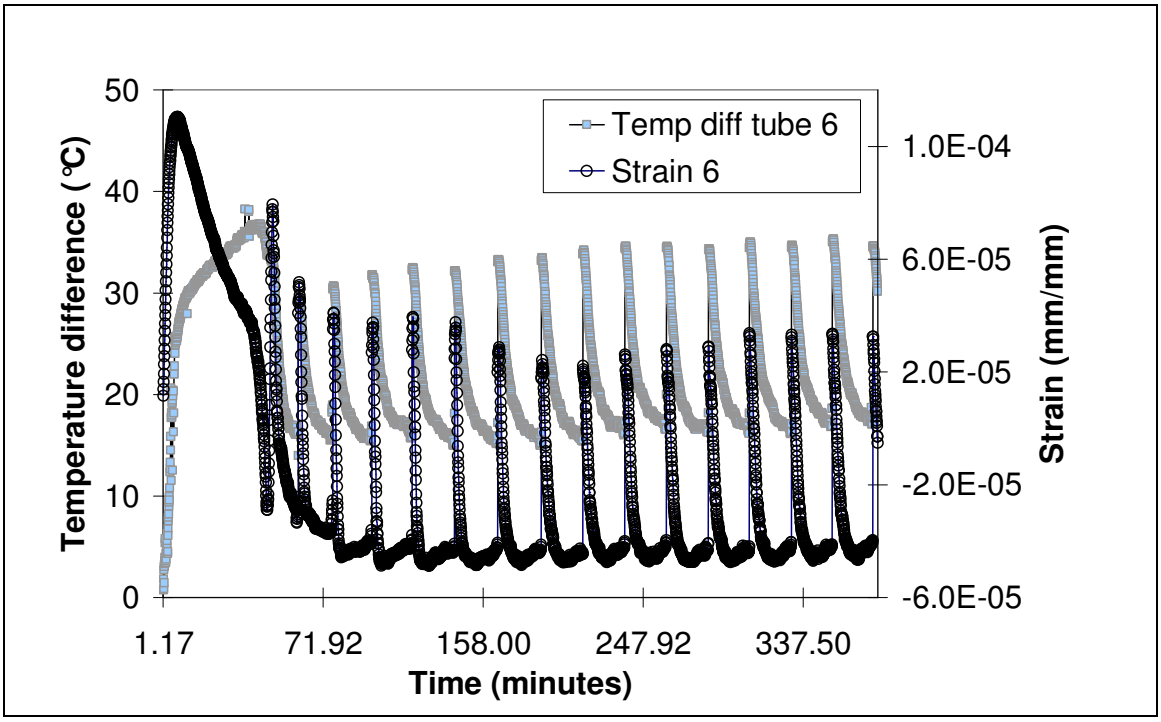

Fig. 5.4 (c) Test 6A

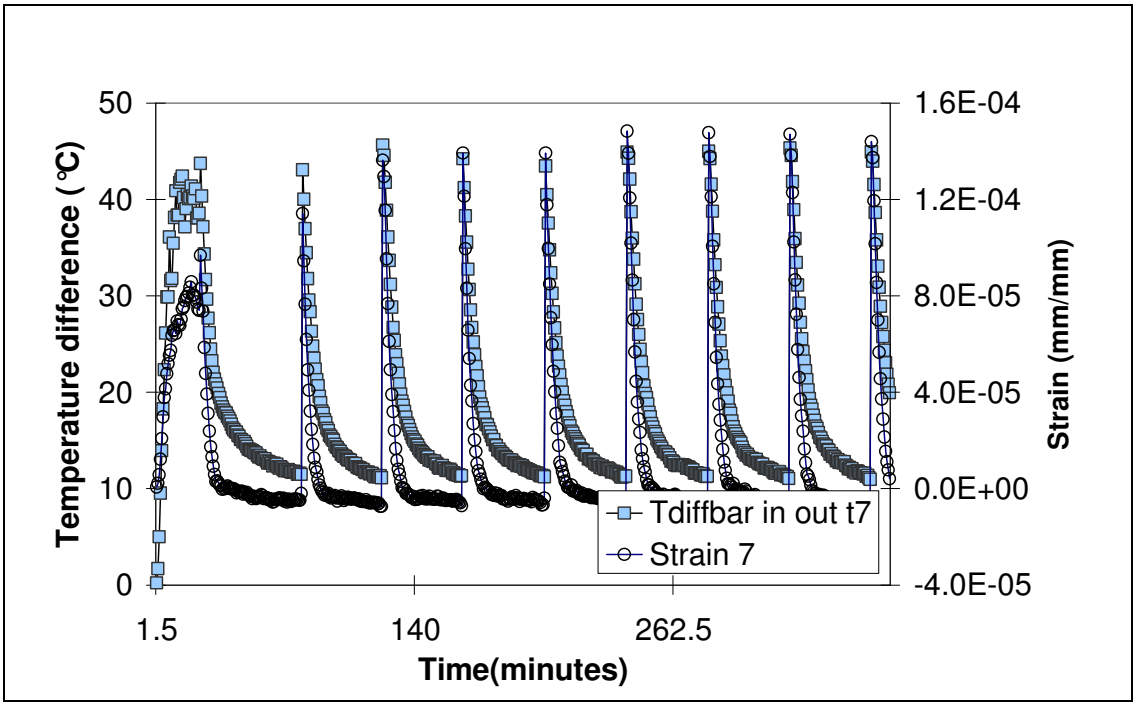

Fig. 5.4 (d) Test 7A

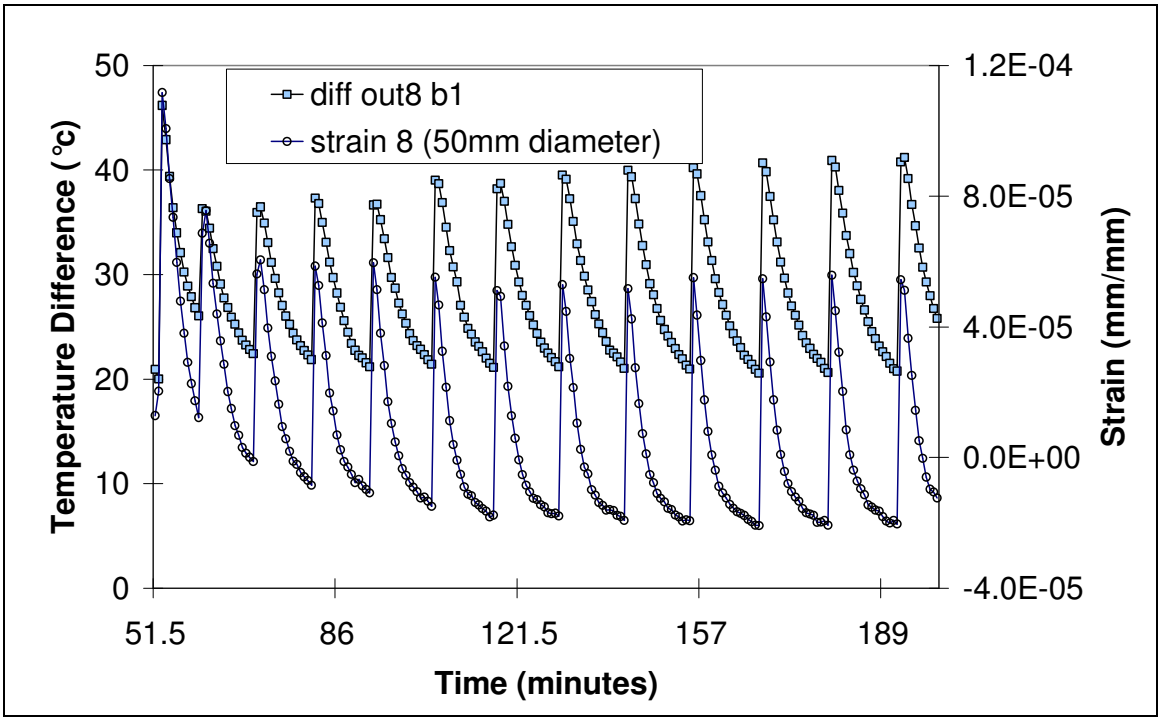

Fig. 5.4 (e) Test 8A

Figure 5.4 Measured fluctuations in the temperature difference between the bar and the sample, and the strain (excluding thermal expansion) in the sample.

Based on the simple thermal-stress model (section 4.3), the tensile stress in the sample is expected to be proportional to the temperature difference between the bar and the sample. This expected relationship is tested in Figure 5.5. Each of the data points represents a temperature cycle. Evidently the actual strain amplitude is smaller than the expected amplitude. This is because coupling between the bar and the sample was not completely rigid (as assumed in the simple analytical model): flexure of the flange which coupled the bar to the sample allowed some relief of the thermal stress. From the predictions presented in the previous chapter (section 4.3, Figure 4.1), the sample strain for the 50mm bar is expected to be less than for 75mm bar, which is confirmed by the measurements.

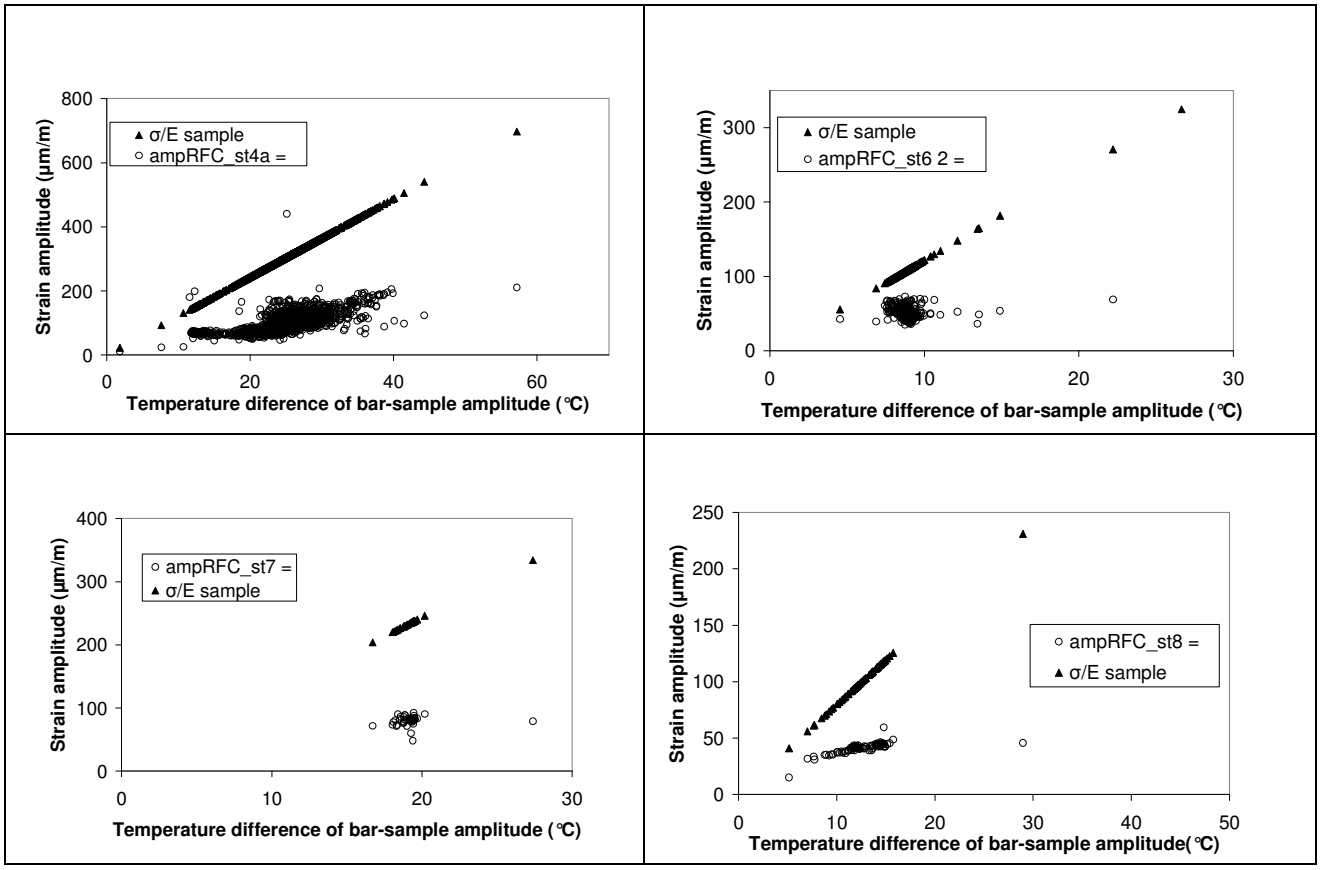

Figure 5.5 A strain and temperature difference plot. "ampRFC" is measured strain amplitude, σ is stress and E is modulus of elasticity

As Figure 5.5 illustrates, there was variability in the measured amplitudes of the temperature and strain variations; this variability is quantified in Figure 5.6. Some of this variability was caused by aliasing, because the sampling rate was not much higher than the frequency of the temperature and strain fluctuations (see the results for Test 4 in Figure 5.4), and the table below which gives the sampling rate and frequency of stress fluctuations.

Table 5.2 Comparing Sampling rate and frequency of stress fluctuation

Test	Sampling rate (Hz)	Frequency of stress fluctuations (Hz)
Test 3	$16.6X10^{-3}$	$4.2X10^{-4}$
Test 4	$3.33X10^{-3}$	$4.2X10^{-4}$
Test 5	$16.6X10^{-3}$	$7.5X10^{-4}$

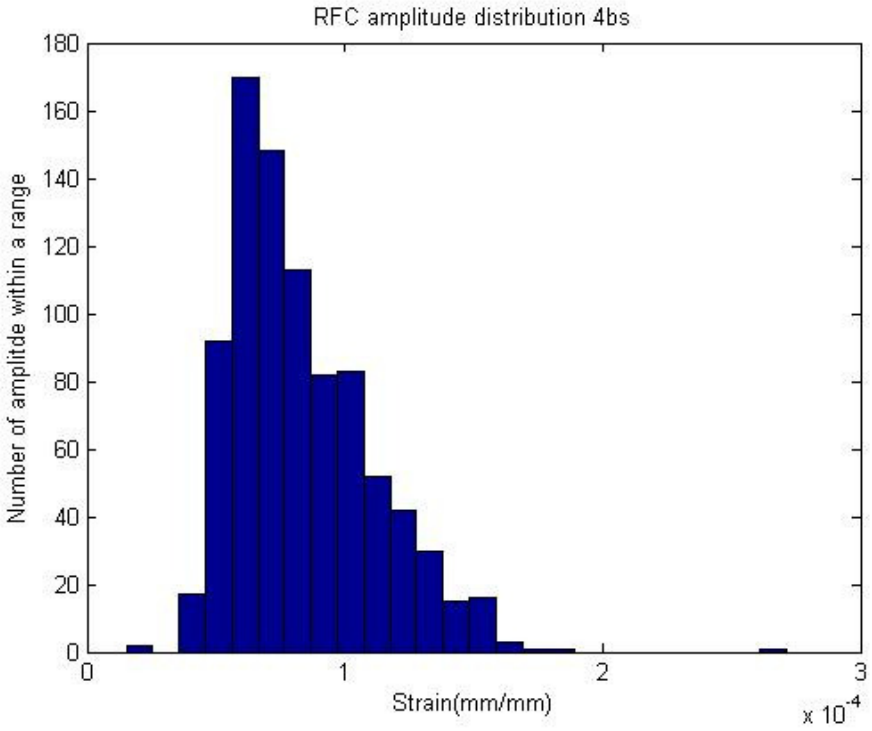

(a) Strain amplitude distribution

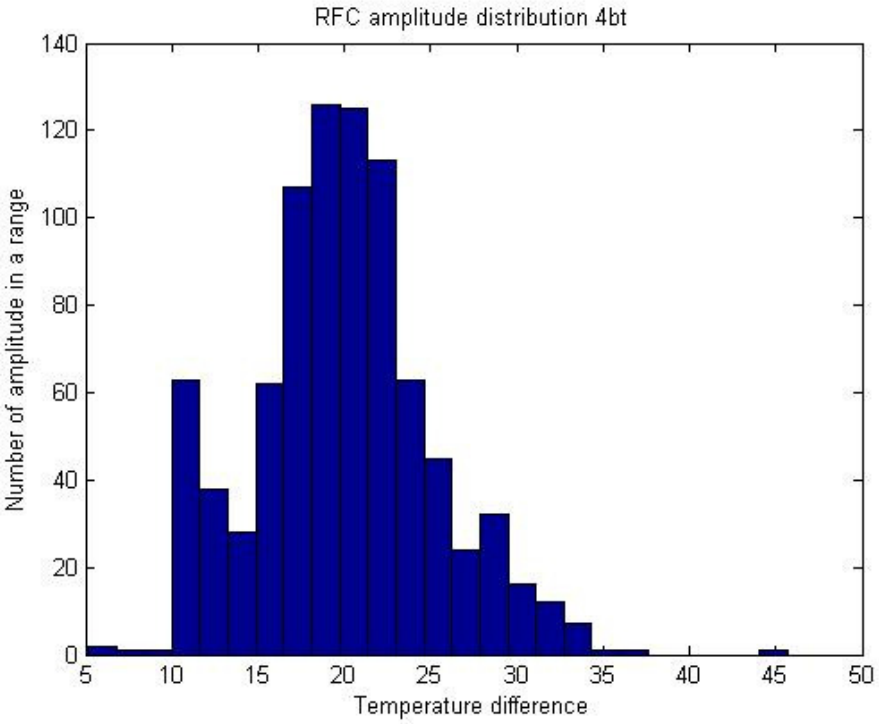

(b) Temperature amplitude distribution

Figure 5.6 Distribution plots of variations in sample (a) strain amplitude and (b) amplitude of the temperature difference between the bar and the sample

5.3 Residual stress

The residual hoop stress was estimated by using the elastic equations of ASTM standard G38 (for C-ring specimens), and also measured using strain gauges placed around holes which were carefully drilled to relieve the stresses (Figure 5.7); the diameters of the holes are tabulated in table 5.3 and 5.4. The strain gauges were on a circular base (diameter 10mm) with the hole drilled at the centre. In the former method the diameters of rings cut from the tube samples were measured before and after cutting through the rings to allow elastic relaxation. The averages of diameters before and after cutting were used in the following equation.

$$\sigma = 4(\Delta D)Etz/(\pi D^2)$$

Where σ is the hoop stress, ΔD is the change in diameter upon unloading, E is the elastic modulus, t the wall thickness, and D the average diameter. Values of the correction factor z (for values of D/t smaller than 20) are listed in ASTM standard G38; z has values close to 1.

This method yielded values of the hoop stress (before welding of the tube into the experimental rig) of 63 MPa (tensile stress); a similar value was found with the method using strain gauges.

The results from the measurements with the strain gauges are summarised in Table 5.3 (tube only) and Table 5.4 (tube welded into rig), with Figure 5.8 showing the direction of the major stress for the two cases (note in Figure 5.8 that Gauge A was oriented in the circumferential [hoop] direction in all cases). Before the tube is welded into the rig, the major residual stress is tensile, and is in the hoop direction. After the tube is welded into the rig, the residual stress is compressive, with the direction of the major stress between the circumferential and longitudinal directions. Examination of the cracks after sample failure showed that this residual stress direction did not affect the crack direction – the cracks were circumferential, showing that the stress causing cracking was oriented longitudinally; the single exception to this was sample 4A which cracked along the longitudinal seam weld in the sample.

Table 5.3 Residual stress measured on tube

Location	Gauge	Hole diameter [mm]	Strain A ¥ [µm/m]	Strain B [µm/m]	Strain C [µm/m]	Stress 1 [MPa]	Stress 2 [MPa]	Theta [θ]*.
Gauge 1	1	1.590	-35	17	18	25.7	-4.2	158.1
Gauge 2	2	1.605	-65	2	8	57.4	13.4	160.1
Gauge 3	3	1.605	-82	-6	21	65.2	10.5	167.3

*Theta indicates the direction of Stress 1 relative to the "a" gauge of the rosette.
¥ The "A" gauge was oriented in the circumferential direction.

Table 5.4 Residual stresses measured on tube after welding into the test rig

Location	Gauge	Hole diameter [mm]	Strain A ¥ [µm/m]	Strain B [µm/m]	Strain C [µm/m]	Stress 1 [MPa]	Stress 2 [MPa]	Theta [θ]*.
Gauge 1	1	1.598	135	19	6	-32.6	-129.0	65.1
Gauge 2	2	1.633	174	19	44	-69.3	-192.2	58.5
Gauge 3	3	1.633	179	15	3	-50.3	-160.8	70.6
Gauge 4	3	1.610	168	12	17	-39.3	-147.1	72.8

* and ¥ describe in Table 5.3 note.

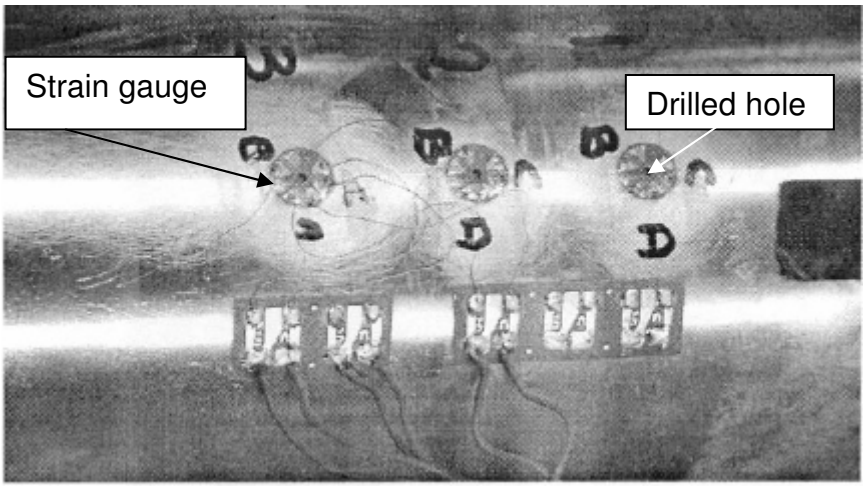

Figure 5.7 Strain gauges mounted on the tube for residual stress measurement

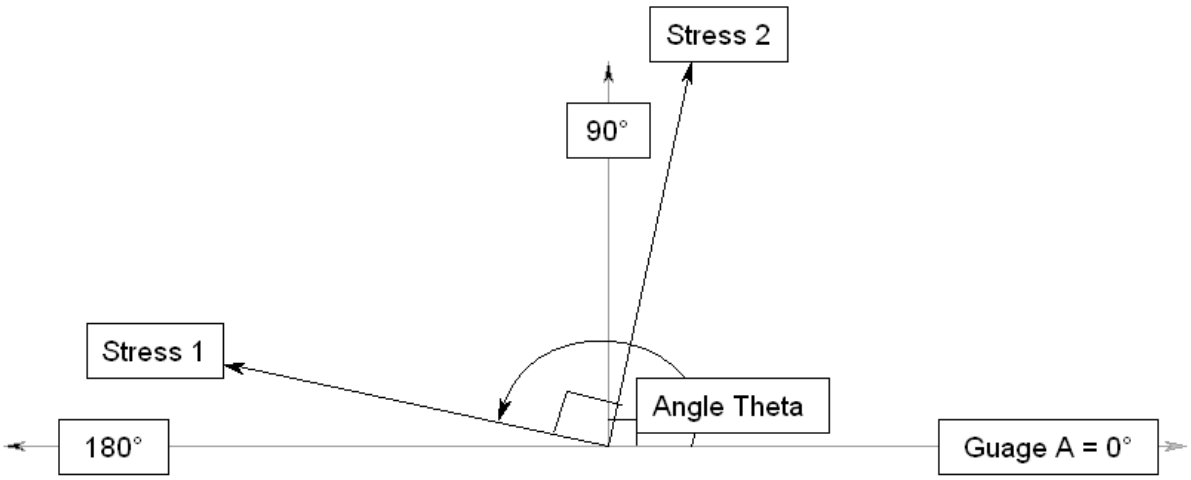

(a)

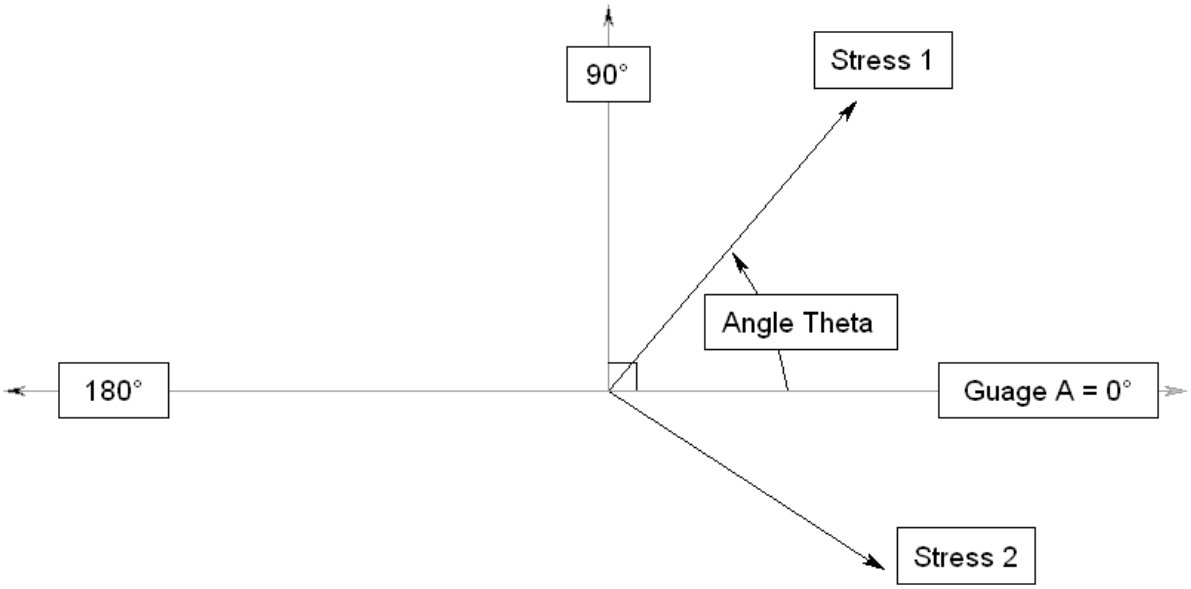

(b)

Figure 5.8 Sketches showing the direction of residual stress in (a) as-received tube and (b) tube welded into the test rig

5.4 Effect of varying stress on failure

The results could be used to test whether cyclic loading contributes significantly to crack growth. It was possible to perform this check because the amplitude of the strain cycles varied somewhat tests, and with different average sample temperatures (Figure 5.9). If cyclic loading played an important role, one would expect a significant effect of the cyclic strain (hence the cyclic thermal stress) on the rate of crack growth (and hence on the time to failure) [36]. However, the results summarised in Figure 5.10 shows that, while there was some variation in the cyclic strains in different tests, there is no correlation between the cyclic

strain and the time to failure. Rather, the time to failure correlates with the sample temperature and (less strongly) with the applied (average) stress (Figure 5.10) – both as expected for chloride cracking, rather than corrosion fatigue. It is hence concluded that cyclic loading played little role in these experiments. Also, the results presented in the next chapter illustrate that the cracks had the classic branched morphology of chloride cracking (and hence were not typical corrosion fatigue cracks).

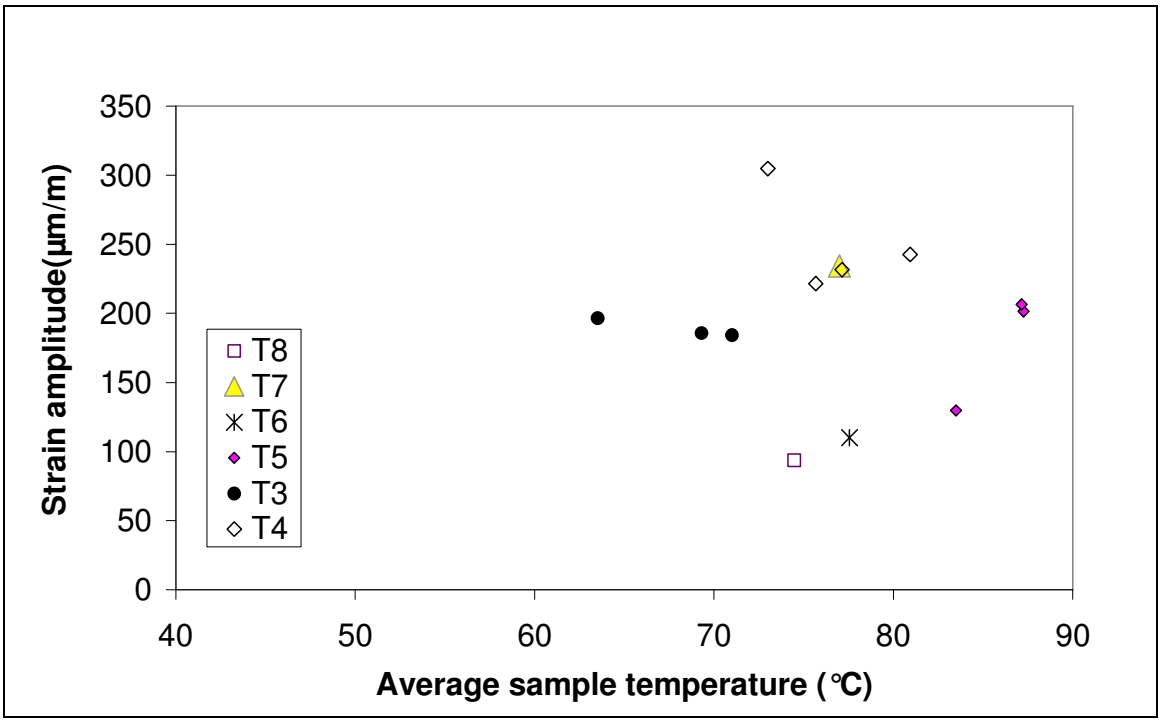

Figure 5.9 Strain amplitude and average sample temperature for the different tests

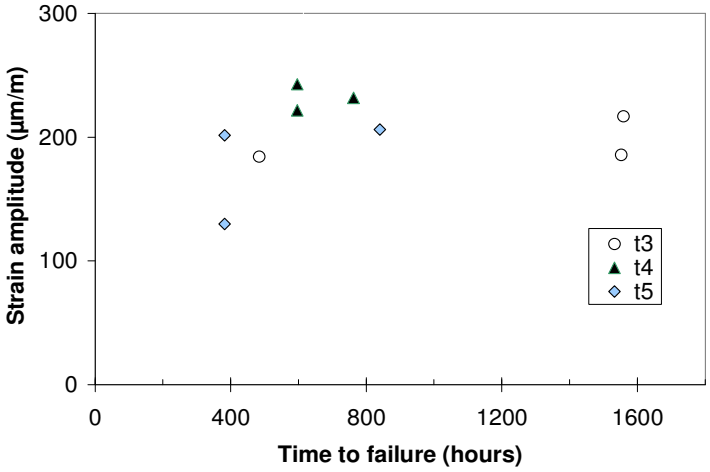

(a)

b)

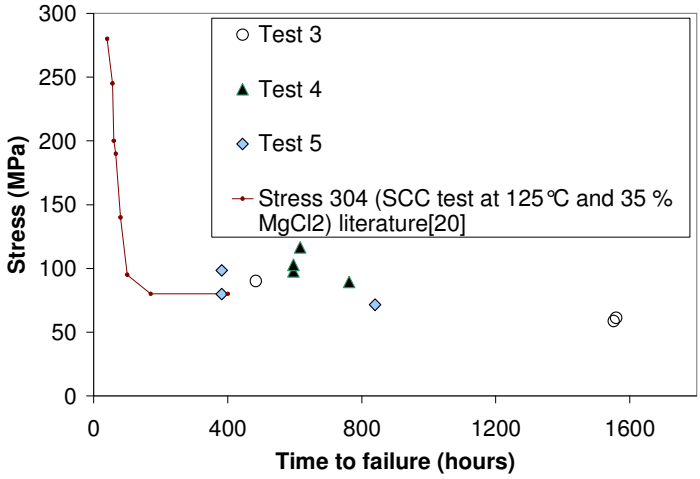

(b)

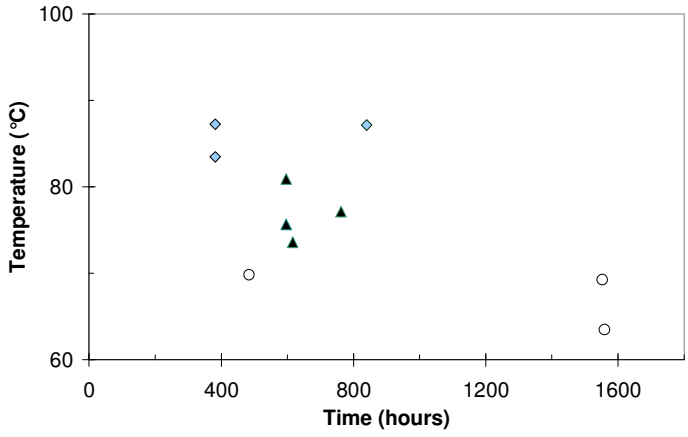

(c)

Figure 5.10 Relationship between time to failure (first through-thickness crack) and a) strain amplitude, (b) average stress (literature data included), and (c) sample temperature.

The absence of an effect of stress cycling does agree with the arguments advanced by Pugh [18], who suggested that stress corrosion cracks advance discontinuously, with each advance a brittle failure. Experimental evidence for such discontinuous advance has been summarised by Newman and Sieradzki [10] If one assumes that the distance by which the crack advances per event is 0.5 µm, as for 310 stainless steel in boiling magnesium chloride solution [18], and taking the typical crack growth rate in this work to be 6 µm/hour (see Figure 6.7 in the next section), then the time between crack growth events is estimated to be 300 seconds. This is significantly shorter than the period of the temperature and stress fluctuations, of which the period was around 2500 s (Table 5.2). In this view, in this work the stress fluctuations simply occurred at too low a frequency to influence crack growth significantly. The low crack velocity, corresponding to stress intensities just above $K_{I\,SCC}$, with crack velocities much lower than the plateau values, supports a direct role of mechanical deformation in crack growth [11]. This is also in line with the crude estimate of the stress intensity in these tests: for the typical average stress of 100 MPa (Figure 5.10), and taking a crack length of 5 mm, the stress intensity (calculated as $\sigma[\pi a]^{0.5}$) is estimated as 12.5 MPa.m$^{0.5}$, similar to the reported threshold stress intensity for Type 316 in hot magnesium chloride solutions [11].

Chapter Six

6 Visual examination and metallographic analysis

As shown in the previous chapter, the samples cracked in a manner consistent with chloride cracking, with the time to appearance of the first through-wall crack depending on the average stress and sample temperature. In addition to these differences between samples, within any one test sample local variations in temperature and stress were present: the ends of the sample close to the end flange were hotter, and increased residual stress was expected close to welded joints. It was hence important to study the distribution of cracks on the internal surfaces of the samples, and also the crack paths.

To this end, visual examination and stereo microscopy of the internal and external surfaces were performed. For examination of the internal surfaces, the samples were first sectioned into three sections. Then the sections' internal surfaces were cleaned with inhibited HCl. The fracture surfaces (of opened-up cracks) were examined by scanning electron microscopy, and polished cross-sections were studied to determine the crack path and crack depth distribution.

6.1 Appearance of external and internal surfaces

6.1.1 External surface examination of test rig samples

Through-thickness cracks were recognised by solution leaking through the crack, causing white magnesium chloride to crystallise on the outside of the sample. The first visible crack was the definition of failure, at which time the test was stopped for that sample. The majority of examined cracks were along the circumference of the tube (sample). As mentioned in Chapter 5 there was one exception (sample 4A), where the crack was along seam weld heat affected zone (the seam weld was longitudinal).

6.1.2 Internal surface examination of the test rig samples

The internal surfaces were discoloured after the tests, because of the presence of corrosion products. In the case of samples T3A and T3C the internal surface was greenish (likely due to the release of chromium by pitting corrosion, see Figure 6.1 (b)) while the internal surfaces of other samples were reddish-black (Figure 6.1(a)). Many cracks were visible on the internal surfaces of all samples, above and below the water line. The majority of cracks did not pass through the wall thickness (a result of the experimental approach to stop the test as soon as the sample displayed a through-thickness crack). Some cracks were also observed on the central bar and the end flanges. This was especially the case in test 3, samples A and C, where the bar was heavily cracked (see figure 6.2). The longitudinal direction of the cracks in the bar indicate that these formed because of the thermal gradient within the bar, with the interior expanding more than the outer regions of the bar during heating (causing tensile stress on the outer surface of the bar). Cracks in the end flanges were close to the top weld.

On some of samples pits were associated with cracks (Figures 6.3 and 6.4). However, because of the possibility of corrosion after crack growth started, it is not possible to state that the cracks initiated from corrosion pits. A few instances were observed where the crack apparently initiated from notches at the welded joint (Figure 6.5).

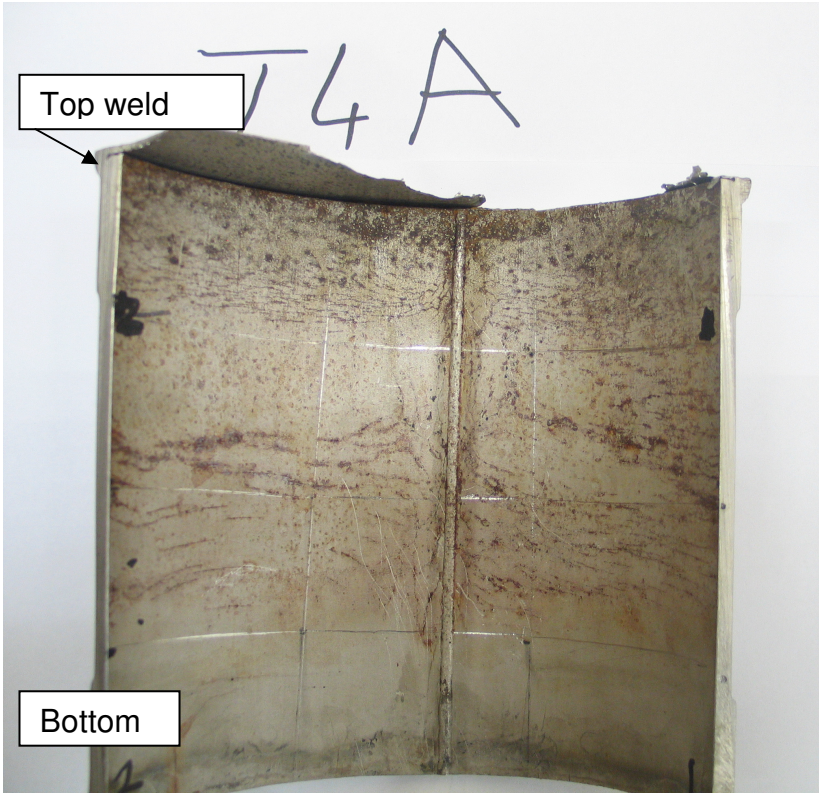

(a) Sample T4A

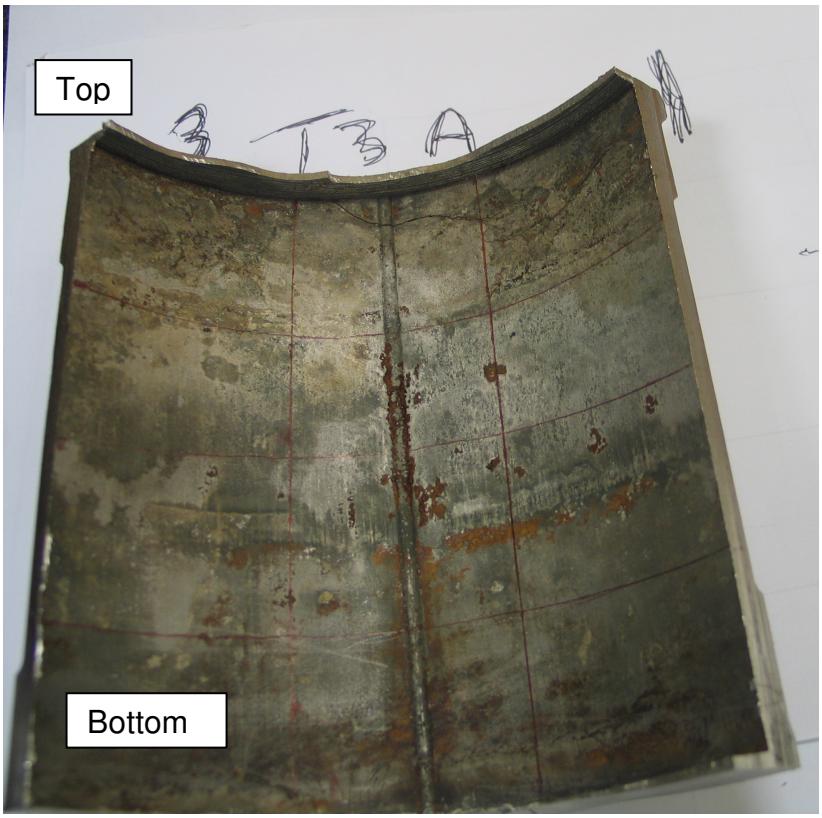

(b) Sample T3A

Figure 6.1 Cleaned internal surfaces of samples after testing, showing reddish-brown and greenish surfaces

(a) Sample 3C

(b)Sample 3A

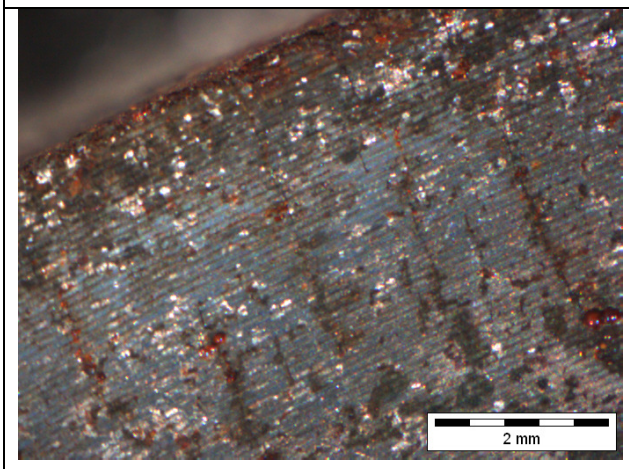

(c) end flange

Figure 6.2 Cracking of test rig other than in the tubular sample: (a) bar of test 3C, (b) bar of test 3A, and (c) end flange of sample 5C close to weld with sample (see also Figure 6.5)

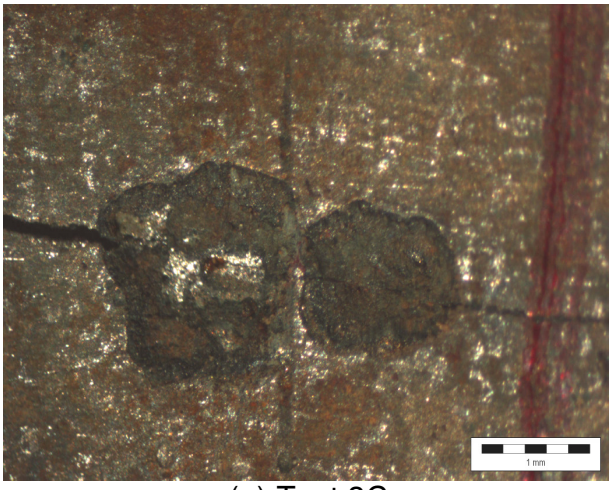

(a) Test 3C

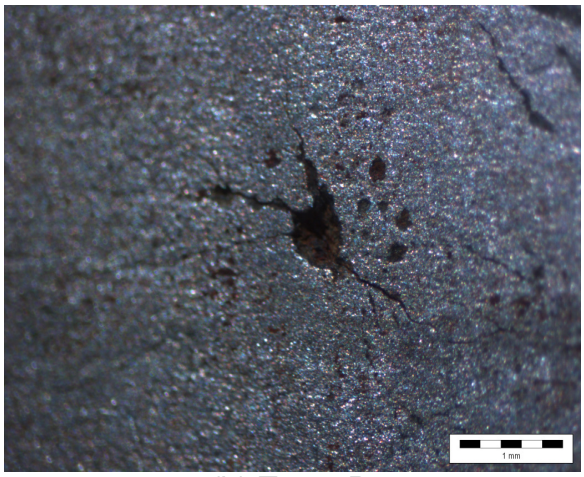

(b) Test 5B

Figure 6.3 Association between pits and cracks on internal surface after testing.

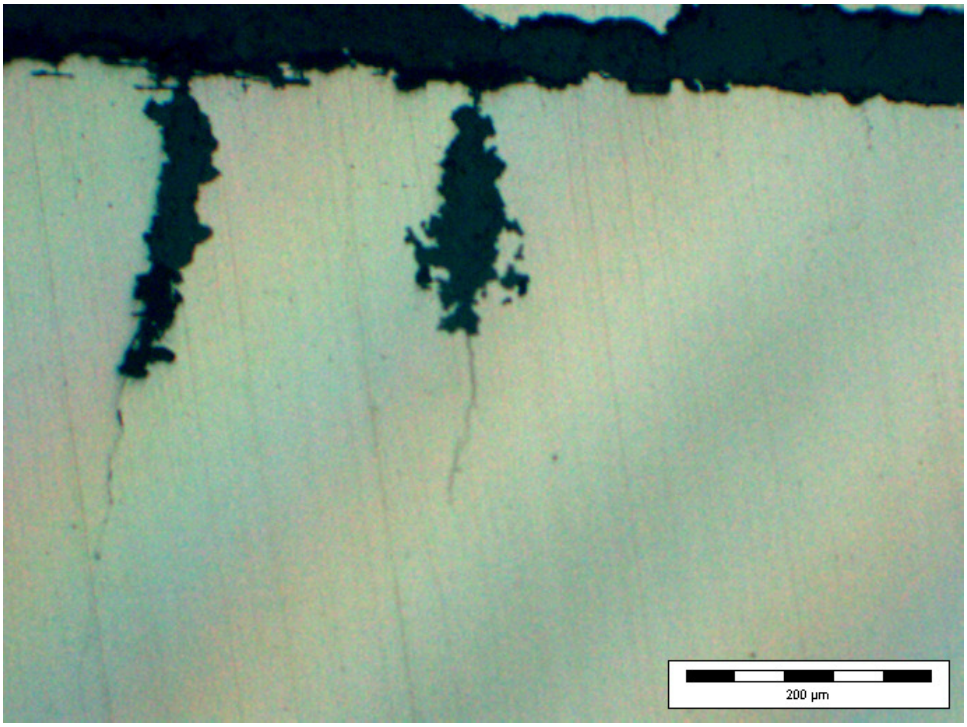

Figure 6.4 Cross-section of sample from test 5C: cracks associated with corrosion pit

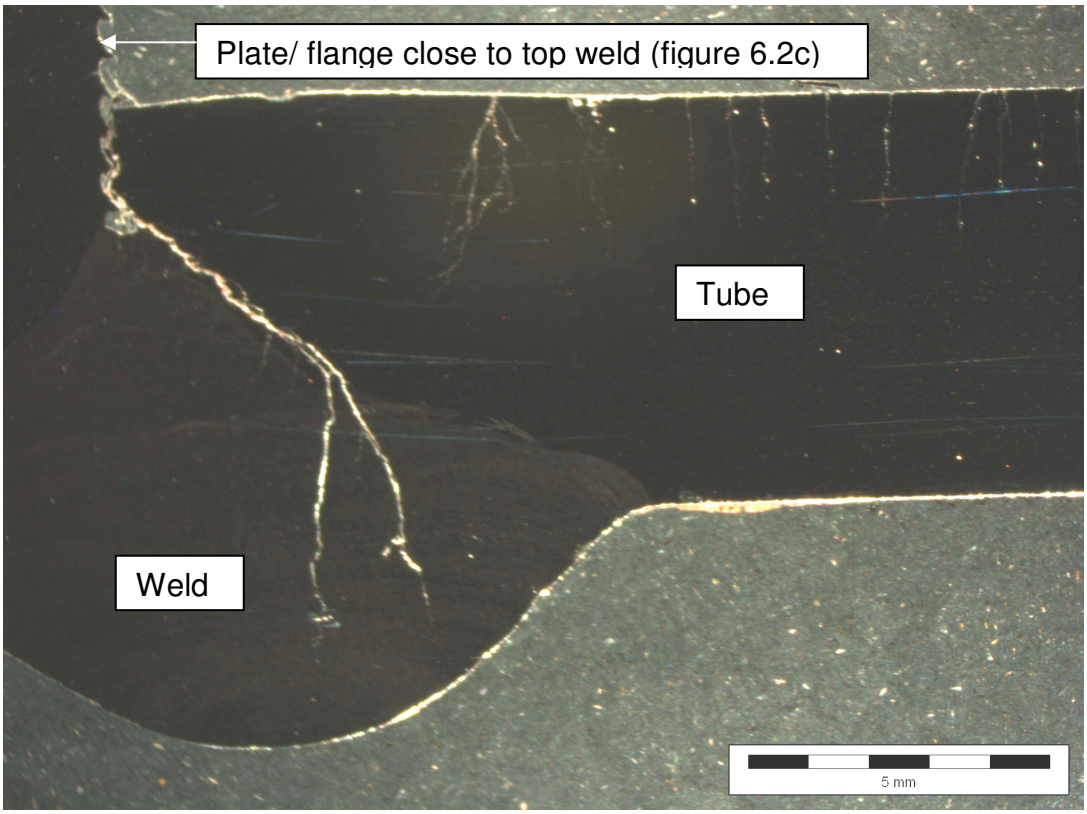

Figure 6.5 Cross-section of sample T3A top: crack initiated from the top weld root (between the end flange and the tubular sample).

6.1.3 Crack densities and crack lengths

The surface cracks were counted and mapped for every sample. An estimate of the average crack formation rate was obtained by dividing the crack density by the exposure time. Cracks which intersected were counted as separate cracks. The minimum length of cracks which were counted was 0.82mm (for stereo microscopy of internal surface cracks), and for optical microscopy of polished cross-sections the minimum counted crack depth (at 500X magnification) was 20µm. Samples that took longer to fail generally had lower average crack formation rates (Figure 6.6). The distribution of crack depths was measured on cross-sections through the samples, by optical microscopy. It is recognised that this can underestimate crack depth, if the crack tip does not fall within the polishing plane, but this method does give a way of comparing different samples. An average crack growth rate was calculated, assuming that the deepest cracks grew for the entire exposure period. Results are given in Figures 6.7 and 6.8. Because the sample wall thickness was larger close to the sample top than at the midpoint, the growth rate is not simply inversely proportional to the time to failure - in some cases the longest crack (close to the sample top) was not the crack which led to leakage. In Figure 6.8 the relation of crack velocity and inverse temperature is shown [11].

A typical distribution of crack depths is shown in Figure 6.9; the flat nature of the distribution – with many shallow cracks as well as deep cracks – indicates that cracks nucleate throughout the test period.

The high crack density and wide distribution of crack depths illustrate that the approach used in this work cannot be used to produce samples with just a few, well-defined cracks. The aim of this project was to produce cracked samples which can serve as test pieces for the laser-welding repair method. Whether these samples are appropriate for testing the repair method depends on the actual in-plant components (to be repaired) having similarly high crack densities. Evaluation of the in-plant components did not form part of the scope of this project, though.

The distribution of crack densities on the sample surfaces followed essentially two types (Figure 6.9). In the cases where the electrolyte level was maintained at half the height of the sample (runs 4C and 4D) the crack density peaked around the water line – presumably because of locally increased salt concentration just above the water line, through splashing and evaporation, or "creeping" of the salt [37]. For samples which were kept filled during the runs, the crack density peaked at the upper and lower ends of the samples, which is where the temperature was highest. This confirms the very strong effect of temperature on chloride cracking: on the basis of the finite element model, the difference in temperature along the sample height was only some 10°C. While the effect on crack density is not apparent in Figure 6.9, the notch machined into some samples did enhance crack nucleation (Figure 6.10), but without a detectable effect on time to failure.

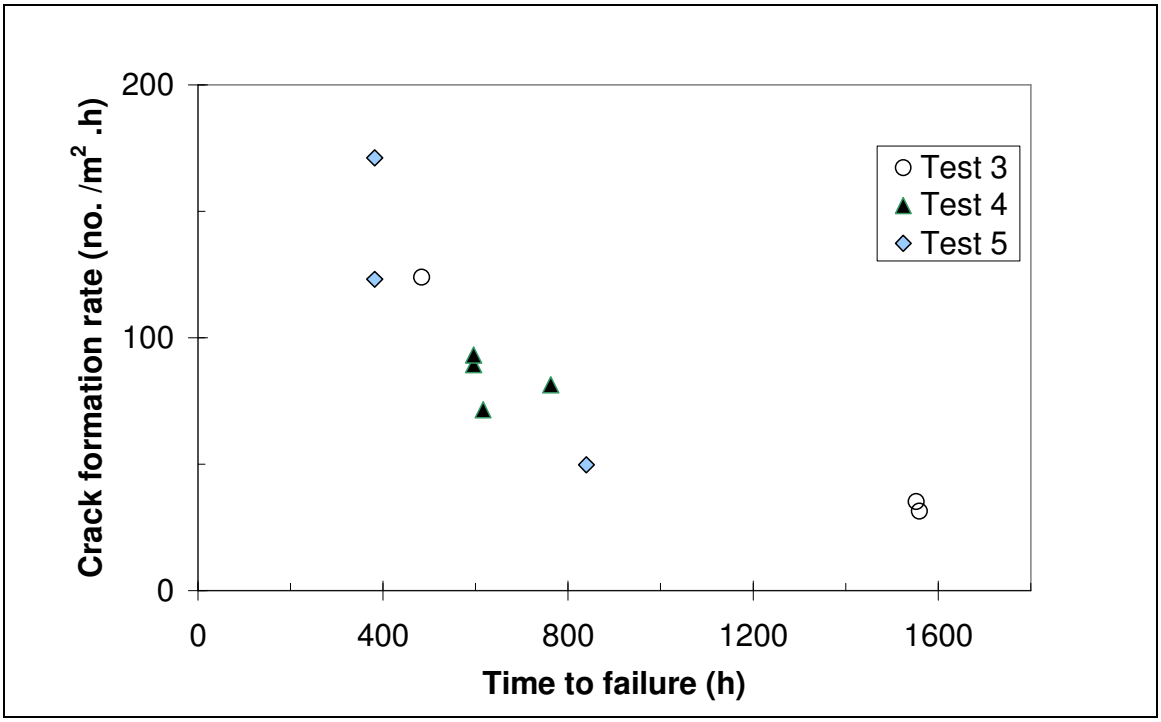

Figure 6.6 Internal surface crack density and time to failure

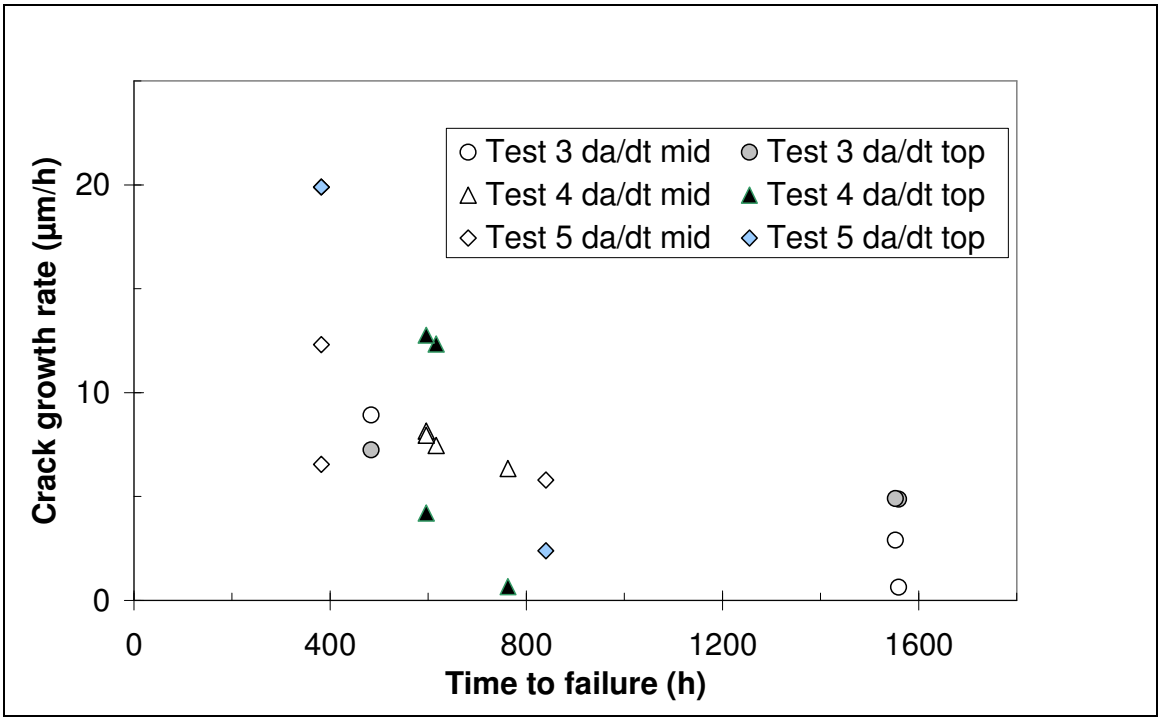

Figure 6.7 Average crack growth rates

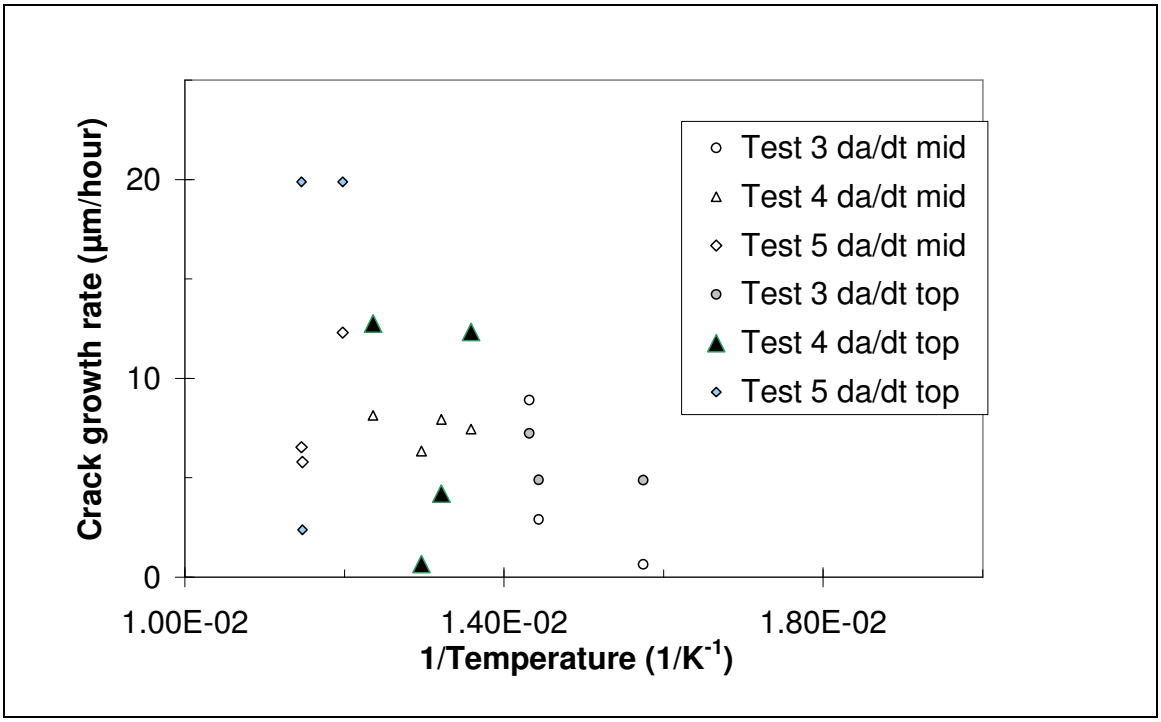

Figure 6.8 The relation of crack growth rate and temperature inverse

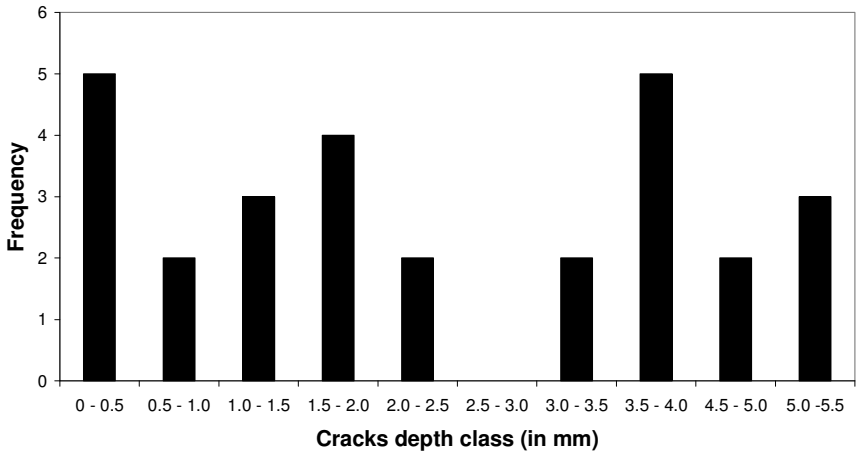

(a)

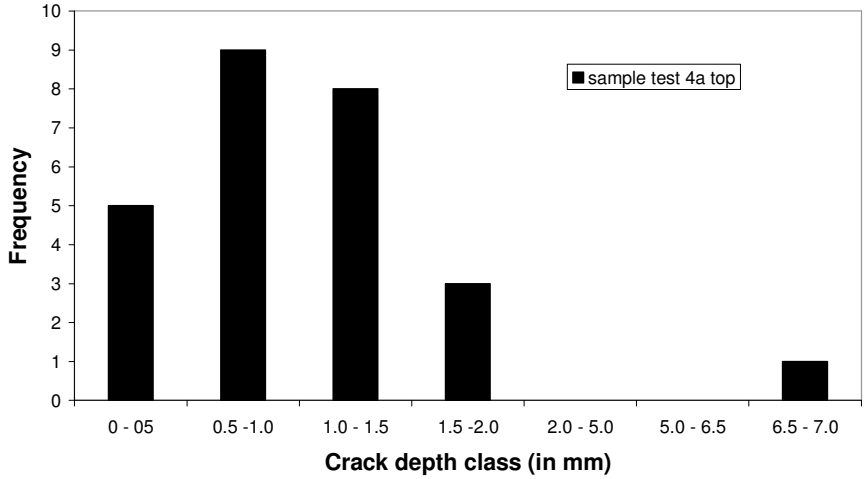

(b)

Figure 6.9 Distribution of crack depths, as measured on polished cross-section at (a) mid point of sample 4D,and (b) top part of sample 4A

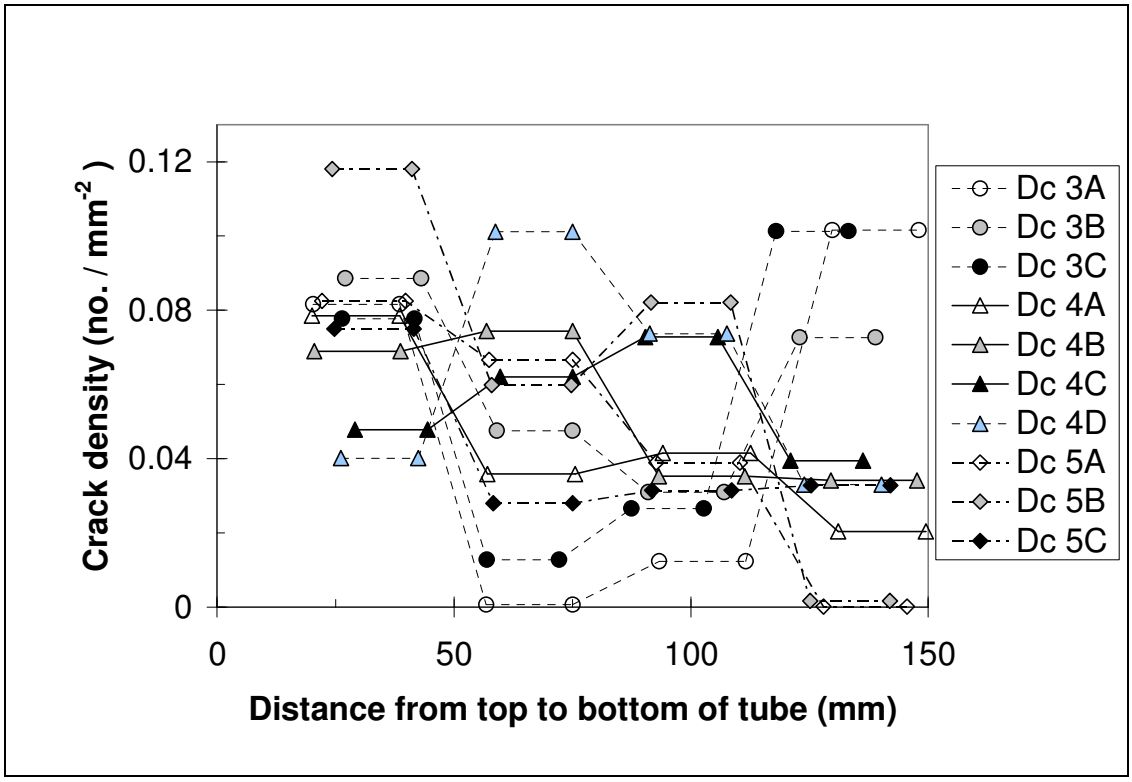

(a)

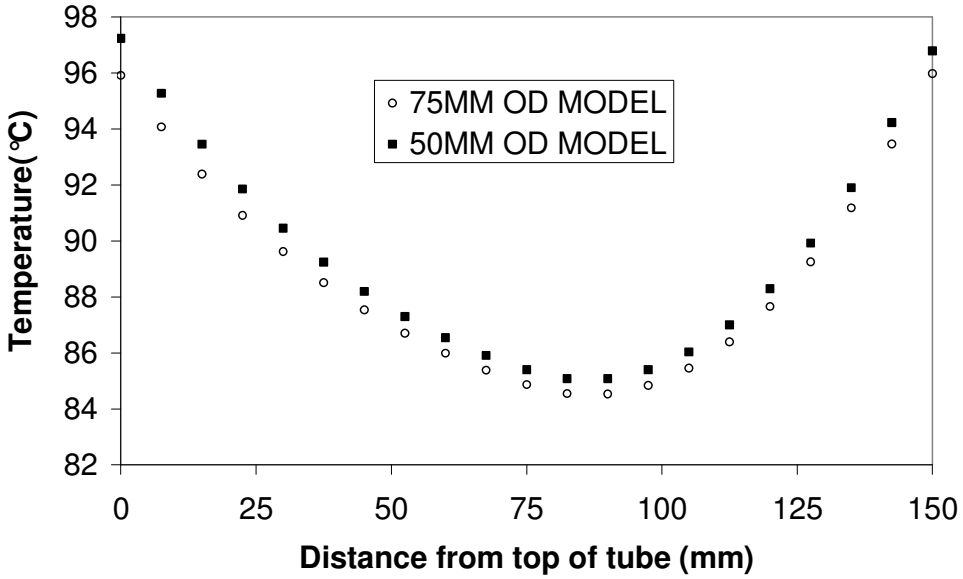

(b)

Figure 6.10. Variation of crack density (crack formation) with height along the interior surface of the sample (a), and variation in sample temperature with height as predicted by the finite element calculations (b).

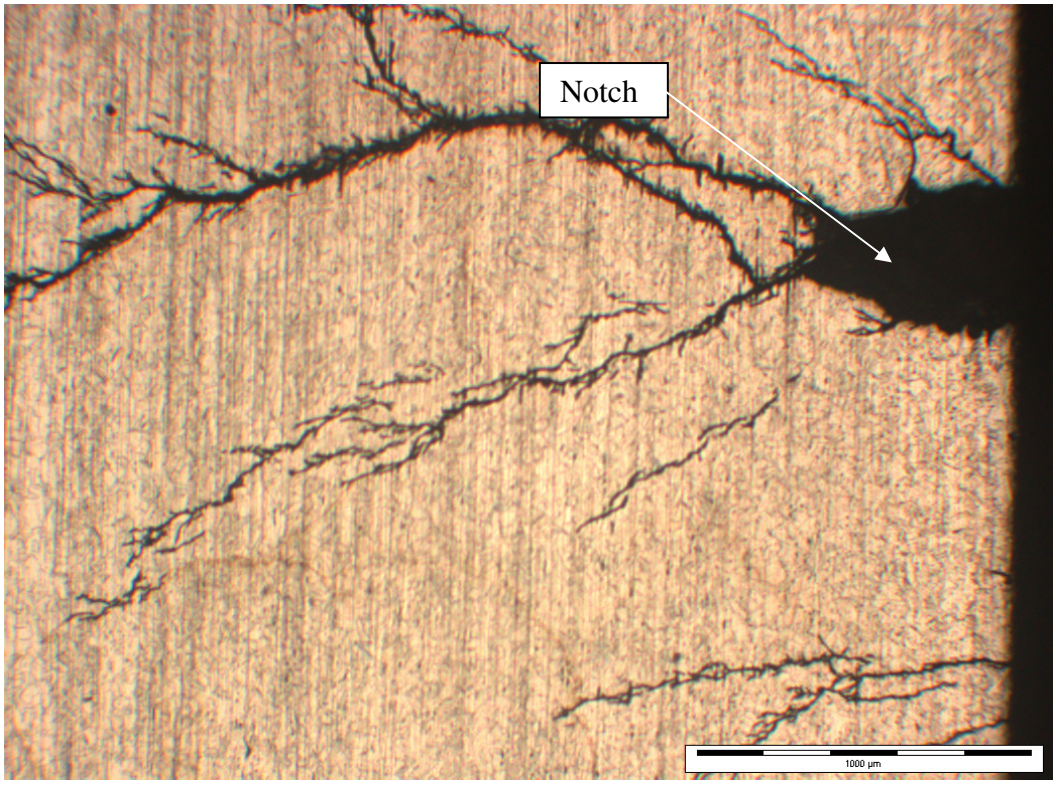

Figure 6.11 Crack that might have initiated from a notch, as seen on a sample cross-section (optical micrograph).

6.1.4 Crack paths

Examination of polished and etched cross-sections confirmed that the cracks were transgranular and branched (Figures 6.12 and 6.13), as expected for chloride cracking of unsensitised austenitic stainless steel. In some cases, anodic dissolution appeared to have initiated from the crack flank (Figure 6.13, right-hand image); dissolution took place in the direction of the delta ferrite stringers (phases analysed with X-ray diffraction see appendix B), that is in the rolling direction, in what appears to be a type of "end-grain corrosion".[38]

It was difficult to study the fracture surface, because the fracture surface had been corroded, and because of the presence of nonconductive material (electrolyte residues or corrosion products). However, areas which could be examined confirmed the expected quasi-cleavage appearance of chloride cracking (Figure 6.14). The grain size of as-received and tested material was 40 micron, as shown by figure 6.15.

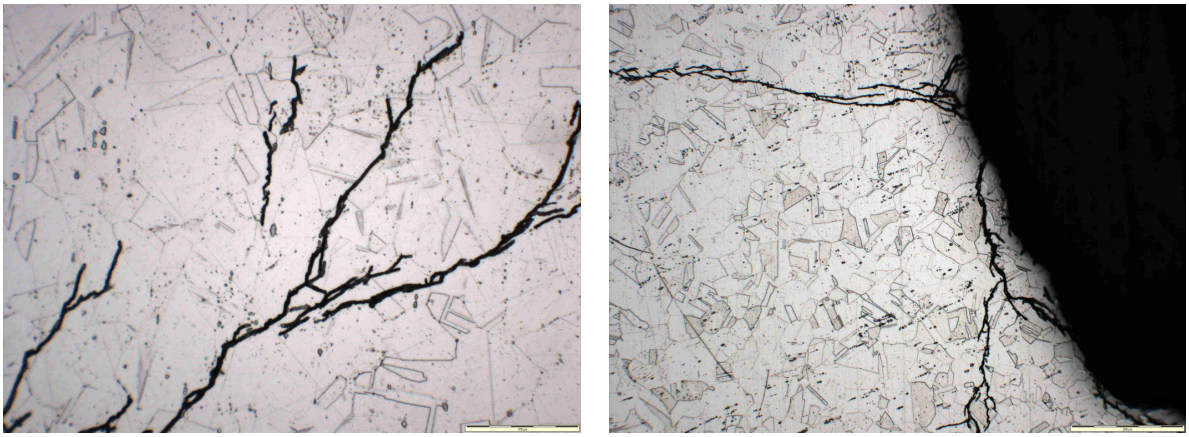

Test 1A Test 2A

Figure 6.12 Branched, transgranular appearance of cracks on polished cross-sections

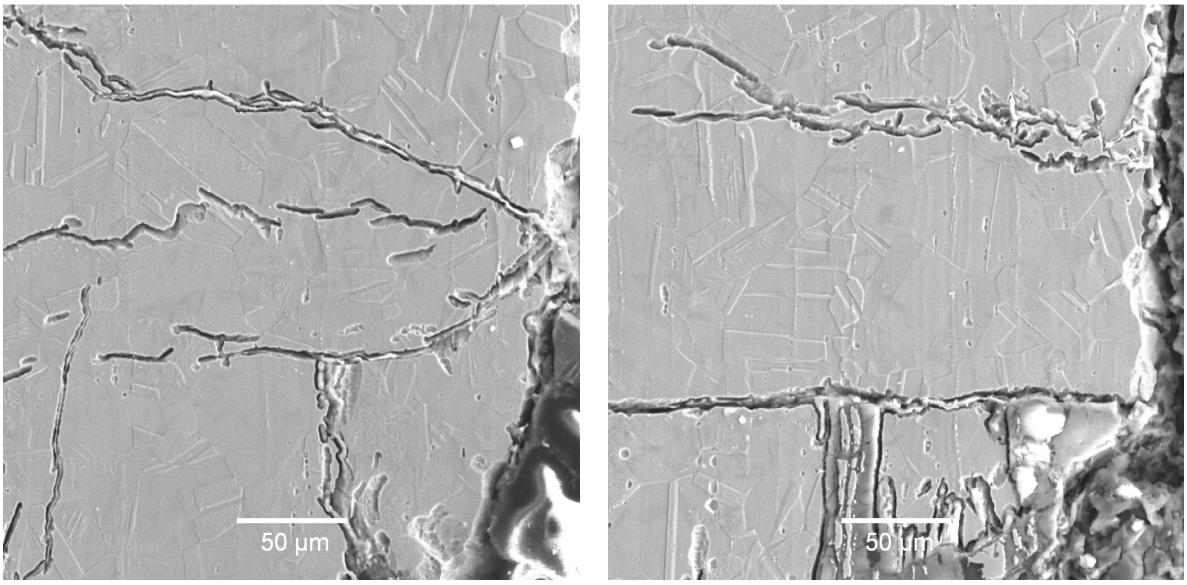

Figure 6.13 Scanning electron micrographs (secondary electron images) of cross-sections through sample after test (sample from test 4D etched electrolytically with 10% oxalic acid solution). Note dissolution in the rolling direction, starting from a crack flank, in the right-hand image.

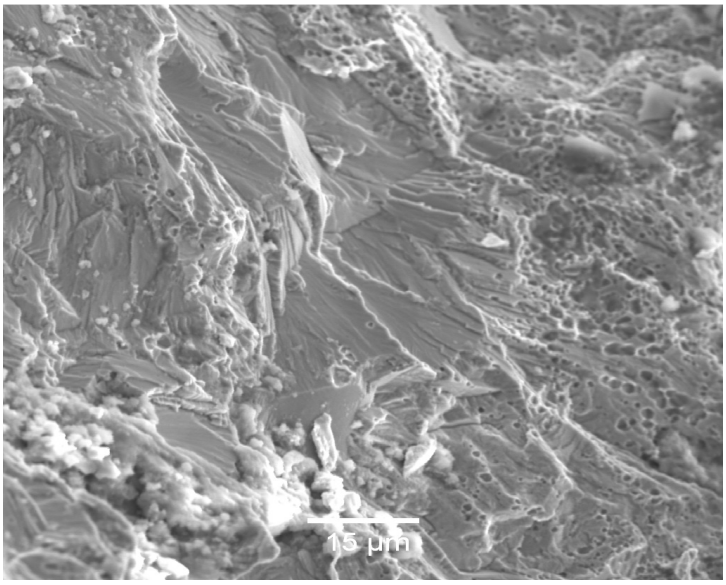

Figure 6.14 Scanning electron micrograph of fracture surface (sample from test 4A), illustrating the quasi-cleavage nature of crack growth.

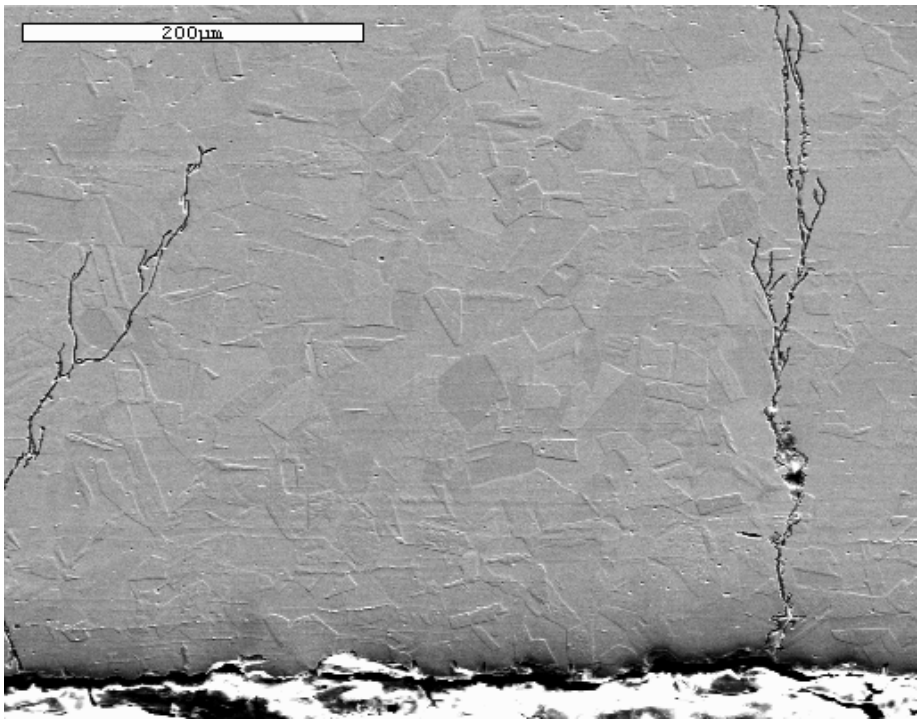

Figure 6.15 The grain size and crack path of material tested

Chapter 7

7 Conclusion and recommendation

The thermal stress, caused by the difference in temperature between the bar and tube (sample), together with the residual stress, was high enough to result in transgranular cracking of the sample. Cyclic loading (negative sawtooth, frequency less than $2X10^{-4}$ Hz) did not appear to affect cracking significantly; transgranular, branched cracks (showing quasi-cleavage) showed the failure mechanism to have been chloride stress corrosion cracking.

The method resulted in the formation of multiple branched cracks in the samples. When these are used to test the envisaged repair process, due consideration should be given to the fact that the samples contain many cracks which do not penetrated the wall thickness. It would be essential to re-test the integrity and crack resistances of samples after weld repair. Crack repair had been tried on test rig but the Laser welding or cladding needs to be researched further for this application, especially for in-situ repair.

Further work

- Measure pH change of solution within refills
- Stress relieve the test rig before testing
- Measuring residual stress of every sample before testing
- Paint the bottom part of sample or paint other part, exposes the selected area to restrict cracking and investigate crack formation.

References

1 Tverberg, J C. "Stainless in the Brewery." *Technical Quarterly of the Master Brewers Association of the Americas*, vol. 38, number 2, pp 67-82 (2001). Sourced from www.mbaa.com
2 Kowaka, M. *Metal corrosion damage and protection technology*, (Chapter 6: Stress corrosion cracking of stainless steels), pp 347- 467. Allerton Press (1990).
3 Craig, B.D. & Lane, R.A. "Material failure part 1: A Brief Tutorial on Fracture, Ductile Failure, Elastic Deformation, Creep, and Fatigue/Environmental assisted cracking." *Amptiac*, vol. 9, issue 1, pp 9-25 (1988).
4 Laser welding, CSIR, www.csir.co.za accessed on 30 January 2006.
5 Nickel Development Institute: *Stainless steel in swimming pool buildings.* 1995. Available from www.nickelinstitute.org, accessed on 28 October 2008.
6 Baddoo, N. & Cutler, P. *Stainless steel in indoor swimming pool building*, Technical note: swimming pools, http://www.bssa.org.uk/publications/files/Baddoo%20Swimming%20Pools%20(3p).pdf, accessed on 30 September 2006.
7 Nakahara, M. *Preventing stress corrosion cracking of austenitic stainless steels in chemical plants*. NiDI (Nickel Development Institute) Technical Series no.10066 (1992).
8 Oldfield, J.W. & Todd, B.. *Ambient temperature stress corrosion cracking of austenitic stainless steels in swimming pools*. NiDI (Nickel Development Institute) reprint Technical series no.14015 (reprinted from *Materials Performance*, December 1990).
9 Jones, D.A. *Corrosion principles and prevention*, 1996. Prentice-Hall.
10 Sieradzki, K. and Newman, R.C.: “Brittle behaviour of ductile metals during stress-corrosion cracking.” *Philosophical Magazine A*, vol. 51, pp. 95-132 (1985).
11 Russell, A.J. and Tromans, D.: “A fracture mechanics study of stress corrosion cracking of Type-316 stainless steel.” *Metallurgical Transactions A*, vol. 10A, pp. 1229-1238 (1979).
12 Jones, R.H. & Ricker, R.E.: "Mechanisms of stress-corrosion cracking." *Stress-corrosion cracking*, R.H. Jones (ed.). ASM (1992).
13 Pugh, E.N.: "Progress toward understanding the stress corrosion problem." *Corrosion*, vol. 41, pp. 517-526 (1985).
14 Sieradzki K. & Newman, R.C.: "Brittle behaviour of ductile metals during stress-corrosion cracking." *Philosophical Magazine A*, vol. 51, pp. 95-132 (1985).
15 Nisbet, W.J., Lorimer, G.W. & Newman, R.C.: "A transmission electron microscopy study of stress corrosion cracking in stainless steels." *Corrosion Science*, vol. 35, pp. 457-469 (1993).
16 Nishimura, R. "Characterization and perspective of stress corrosion cracking of austenitic stainless steels (type 304 and type 316) in acid solutions using constant load method." *Corrosion Science*, vol. 49, pp. 81-91 (2007).

17 Magnin, T., Chambreuil, A. & Chateau, J.P.: "Stress corrosion mechanisms in ductile FCC materials." *International Journal of Fracture,* vol. 79, pp. 147-163 (1996).
18 Pugh, E.N.: "Progress towards understanding the stress corrosion problem." *Corrosion*, vol. 41, pp. 517-526 (1985).
19 Craig, B.D. & Lane, R.A.: "Material failure part 1: Environmental assisted cracking." *Amptiac*, vol. 9, no. 1, pp 9 -16 & pp17 - 25 (1988).
20 Fang, Z., Wu, Y., Zhu, R., Cao, B. & Xiao, F.: "Stress Corrosion Cracking of Austenitic Type 304 Stainless Steel in Solutions of Hydrochloric Acid + Sodium Chloride at Ambient Temperature", *Corrosion,* vol. 50, No. 11, pages 873 – 878 (1994).
21 Sedriks, A.J.: *Corrosion of stainless steels*, 2nd edition. John Wiley & Sons (1996).
22 Chen L., Gao, X.J., Feng, T. & Liu, M.Z.: "SCF feature of austenitic stainless steel in boiling $MgCl_2$ solution." *Acta Metallurgica Sinica (English edition)* series B, vol. 6, pp 451 – 456 (December 1992).
23 Renner, M., Heubner, U., Rockel, M.B. & Wallis, E.: "Temperature as a pitting and crevice corrosion criterion in the $FeCl_3$ test.", *Werkstoffe und Korrosion* vol. 37, pp 183-190 (1986).
24 Cooker, T.W. & Hauser, J.A. (II): "A literature review on the influence of small-amplitude cyclic load on stress corrosion cracking in alloys." *Office of Naval Research(Minerals management services-mms)*, www.mms.gov/tarproject , accessed on 7 June 2006.
25 Van der Wekken, C.J. & Janssen, M.: "Solute transport in corrosion fatigue cracks." *Journal of the Electrochemical Society*, vol. 138, no 10 pp 2891 – 2896 (October 1991).
26 Warrington, R.O. (Jr) & Powe, R.E., "The transfer of heat by natural convection between bodies and their enclosures." *International Journal of Heat and Mass Transfer*, vol. 28, pp 319-330 (1985).
27 B.D. Craig, "Material failure modes desk reference", *Amptiac Desk reference*, http://amptiac.alionscience.com/pdf/deskref.pdf accessed on 3 July 2007.
28 Heuser, H.: "Arc welding of stainless steels- execution of filler metals and processing instructions." *Welding and Cutting*, no. 3. pp 124-126 (2003).
29 Himmer, T., Stiles, E., Techel, A., Nowotny, S. & Beyer, E.: "Using high power laser cladding for rapid tooling and tool repair." *Moldmaking Technology,* http://www.moldmakingtechnology.com/articles/040506.html, accessed on 18 March 2006.
30 Laser cladding, www.csir.co.za/nlc accessed 30 January 2006.
31 Walker, R.: "Lasers: The Cutting Edge in Industry." *The Industrial Physicist,* June 1998, pp 29–33.
32 *Comparisons of Laser Welding to Conventional Welding Processes.* http://www.processeq.com/Pro_Wel_Las.htm, accessed on 2 September 2006.
33 Boyle, N., Kennedy, A. & Connolly, J.: "Laser cladding development for the gas turbine industry." *SIFCO Ireland*, www.sifco-ie.com , accessed on 30 January 2006.
34 Yevko, V. Park, C.B., Zak, G., Coyle, T.W. & Benhabib, B.: "Cladding formation in laser-beam fusion of metal powder." *Rapid Prototyping Journal*, vol. 4, no. 4, pp 168-184 (1998).

35 Hoffmann, K.: *An introduction to measurements using strain gages*. HBM, 1989.
36 Hertzberg. R.W.: *Deformation and fracture mechanics of engineering materials*, second edition. Wiley, pp. 570-581 (1983).
37 Washburn, E.R.: "The creeping of solutions." *Journal of physical chemistry*, vol. 31, pp. 1246-1248 (1927).
38 Chandra, K, Kain, V. and Ganesh, P.: "Controlling end-grain corrosion of austenitic stainless steels." *Journal of Materials Engineering and Performance*, vol. 17, pp. 115-122 (2008).

Appendices

Appendix A: Design of test rig – Load-bearing capacity of bar

The design of the rig is based on the central hollow bar stressing the 304 tube sample. To test that the bar is sufficiently massive to stress the tube, a simple test was applied, namely that the stress in the bar should be less than the proof stress (tensile or compressive) of the bar, when the stress in the tube is at the tube proof stress (compressive or tensile). The values used and results are as give below; the load-bearing area of the bar can be seen to be larger than that of the tube, so the stress in the bar is lower than in the tube

TUBE (304L)

OD (mm)	168
ID (mm)	154
0.2% proof stress (MPa)	189
Area (mm^2)	3541
Load at proof stress (kN)	669

BAR (310)

OD (mm)	75
ID (mm)	25
0.2% proof stress (MPa)	210
Area (mm^2)	3927
Stress at load (MPa)	170

Appendix B: XRD results: 304 tube samples.

X-ray diffraction confirmed that the samples consist of austenite, with a small amount of delta ferrite. The sample was analysed using a PANalytical X'Pert Pro powder diffractometer with X'Celerator detector and variable divergence- and receiving slits with Fe filtered Co-Kα radiation. Phase quantification by means of the Rietveld method (Autoquan Program) gave the delta ferrite content as 1.7±0.6%. The X-ray diffraction data are shown below.

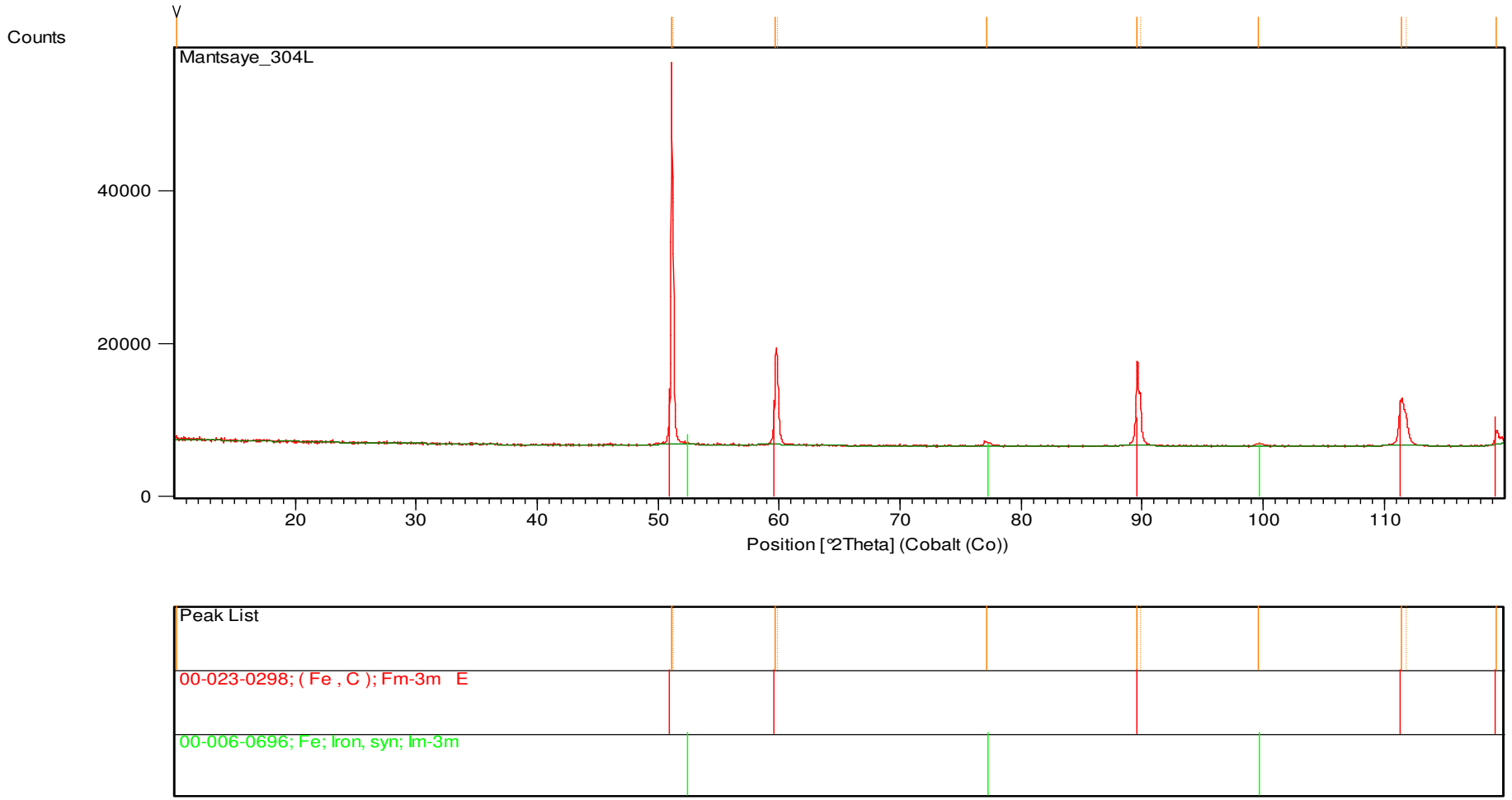

Phase identification with XRD (304 tube sample)